Agenzia Nazionale per le Nuove Tecnologie,
l'Energia e lo Sviluppo Economico Sostenibile

Ministero dello Sviluppo Economico

RICERCA DI SISTEMA ELETTRICO

Numerical Modelling of Pulverized Coal Oxy-Combustion

F. Donato, B. Favini, E. Giacomazzi, F.R. Picchia, N. Arcidiacono, D. Cecere, F. Creta

Report RdS/2010/30

NUMERICAL MODELLING OF PULVERIZED COAL OXY-COMBUSTION

F. Donato, B. Favini, F. Creta (Dipartimento Ingegneria Meccanica ed Aerospaziale – DIMA – Univ. La Sapienza di Roma)
E. Giacomazzi, F.R. Picchia, N. Arcidiacono, D. Cecere ENEA

Settembre 2010

Report Ricerca di Sistema Elettrico
Accordo di Programma Ministero dello Sviluppo Economico – ENEA
Area: Produzione e fonti energetiche
Tema: Sviluppo di un sistema innovativo di combustione oxicombustion – di tipo "flameless" – di carbone per impianti di produzione di elettricità con ridottissimi livelli di emissione, predisposti per la cattura della CO_2

Responsabile Tema: Paolo Deiana, ENEA

Contents

Nomenclature

Symbols

$\check{f}_p$	Dispersed phase probability density function conditioned by the flow realization
$\mathbf{c}_p$, $\mathbf{V}_p$	Single particle velocity
$\mathbf{f}_i$	Body force acting on species i
$\mathbf{J}_i$	Species i mass diffusion flux
$\mathbf{q}$	Thermal flux
$\mathbf{q}_D$	Thermal flux due to Dufour effect
$\mathbf{u}_f$	Gas phase velocity
$\mathbf{u}_p$	Dispersed phase velocity
$\mathbf{V}^c$	Correction velocity to impose mass conservation due to approximated diffusion fluxes for chemical species
$\mathbf{V}_i$	Species i mass diffusion velocity
$\mathcal{E}$	Gas mixture internal energy
$\mathcal{H}_f$	Gas mixture enthalpy
$\mathcal{H}_{f,i}$	Enthalpy of the i^{th} species in the gas mixture
$\mathcal{K}$	Gas mixture kinetic energy
$\mathcal{R}_u$	Universal gas constant
ϑ	Independent coordinate along the tangential direction

C_{p_i} Species *i* specific heat at constant pressure

C_p Gas mixture specific heat at constant pressure

C_{v_i} Species *i* specific heat at constant volume

C_v Gas mixture specific heat at constant volume

D_{ij} Binary diffusion coefficient of species *i* into species *j*

D_i Diffusion coefficient of species *i* into the gas mixture

d_p Particle diameter

E_k Turbulent kinetic energy associated to the lengthscale *k*

E_{pf} Work done by aerodynamic force on the continuous phase in a time unit

f_p Dispersed phase probability density function

f_{ij} j^{th} component of the body force acting on species *i*

$h^0_{f_i}$ Enthalpy of formation at reference state for the i^{th} species

H_p Dispersed phase enthalpy

h_{s_i} Sensible enthalpy for the i^{th} species

h_s Sensible enthalpy for the gas mixture

k^f Fourier coefficient for heat conduction

L_v Phase change heat

m_p Particle mass

n_p Particle number density

N_s Number of chemical species in the gas mixture

p Pressure

Q_{loss} Energy loss from the continuous phases (e.g. radiation)

Q_{pf} Energy dissipation due to the aerodynamic interaction between phases

r	Independent coordinate along the radial direction
R_g	Gas constant
Re	Reynolds number
Re_p	Particle Reynolds number
St	Stokes number
t	Time
T_f	Gas phase temperature
T_p	Dispersed phase temperature
V_{ij}	j^{th} component of species i mass diffusion velocity
W_i	Species i molecular weight
W_{mix}	Gas mixture molecular weight
W_{RUM}	Specific energy flux from the condensed to the gas phase due to the uncorrelated motion and to the aerodynamic interaction
X_i	Species i mole fraction
Y_ash	Ash mass fraction in the coal particle
Y_i	Species i mass fraction
Y_m	$m-th$ functional group mass fraction in the coal particle
z	Independent coordinate along axis direction
$\delta\mathbf{Q}_p$	Dispersed phase heat flux vector
$\delta\mathbf{V}_p$	Particle uncorrelated velocity
$\mathbb{H}_f$	Gas phase flow realization
α_i	Species i thermodiffusion coefficient
α_p	Dispersed phase volumetric fraction

$\delta\theta_p$ Dispersed phase uncorrelated energy

Δ Filter lengthscale

δ_p, β_p Single particle diameter

η Kolmogorov's dissipative lengthscale

Γ_p Specific mass flow rate from the condensed to the gas phase

$\Gamma_{p,i}$ Specific mass flow rate of species *i* from the condensed to the gas phase

Γ_{RUM} Specific energy flux from the condensed to the gas phase due to the evaporation and the uncorrelated motion

ν Cinematic viscosity

ω_i Species *i* mass production due to chemical reactions

Φ_f Dissipation function

Π_p Specific energy flux from the condensed to the gas phase due to the evaporation

Ψ Generic particle property

ρ_f Gas phase density

ρ_p Density of the particle material

τ_f^t Turbulence characteristic timescale

τ_p Particle relaxation time

ε_p, h_p Single particle enthalpy

ϑ_p, ζ_p Single particle temperature

Operators

$\dot{[]}$ Total derivative with respect time

$\overline{[]}$ Reynolds average

$\widetilde{[]}$ Fávre average

$\langle[]\rangle_p$ Mass average

$\{[]\}_p$ Ensemble average

Superscripts

$[]'$ Fluctuation with respect to Reynolds average

$[]''$ Fluctuation with respect to Fávre average

Subscripts

$[]_{f,j}$ j^{th} component of a vector in the continuous phase

$[]_f$ Continuous phase

$[]_{p,j}$ j^{th} component of a vector in the dispersed phase

$[]_\eta$ Dissipative lengthscale

Tensors

$\underline{\delta\mathbf{R}}$ Dispersed phase generalized stress tensor

$\underline{\mathbf{E}}$ Strain tensor

$\underline{\mathbf{S}}$ Stress tensor

$\underline{\tau}$ Viscous stress tensor

Introduction

Research scope

Much attention has been payed to multiphase flows modelling in the last decades. Two concurrent reasons can justify such an interest in the research community. The first motivation is that multiphase flows can be found in a variety of industrial processes and components (e.g. fluidized beds, gas turbine burners, etc.) as well as in many every day life devices (e.g. computer printers); the second reason can be addressed to the increasing computational capabilities, which is making Computational Fluid Dynamics (CFD) to be a more and more useful tool in the design and optimization process of such devices and components. In the CFD framework, Large Eddy Simulation (LES) approach is gaining in importance as a tool for simulating turbulent combustion processes. Such a technique is nowadays a standard as far as single phase phenomena are considered, while much work is being done to improve its performance in multiphase flow applications.

The present work is intended to be a contribution to the development of reliable models for the simulations of multiphase dispersed reacting flow within LES framework. The aim of this research project is to provide an improvement to the capability of existing particle transport models in predicting the dispersed phase evolution under dilute condition and for inertial particles. The main applications towards which this work is oriented are coal powder burners and spray combustors. The coupling of the LES accuracy in predicting gas phase turbulent combustion and an improved model for particle dispersion in the carrier gas could help in the design process of such components.

Physics of turbulent flows

Turbulent flows are one of the physical phenomena that are easiest to find in nature. They characterize the evolution of the oceans as well as of the atmosphere. They are often involved in the operation of man-made devices. In fact, turbulent flows represent the natural status of fluid motion while laminar flows are the exceptions, even though the sequence of their study in mechanical engineering has been inverted. Differently from the laminar case, in turbulent flows the fluid variables at a given point are functions not only of the position but also of time and the instantaneous velocities present components normal to their averaged values.

In Figure 1 a typical example of a two-phase turbulent flow is shown. By paying attention to the multitude of structures that can be seen in the plume of the pyroclastic eruption of St. Helene's mountain, it may be clearer what is meant when turbulence is said to be an example of deterministic chaos. A turbulent field is in fact characterized by the presence of organized structures (eddies), presenting a finite dimension in space (lengthscale) and time (timescale). The Navier-Stokes equations, used as a model for fluid dynamics, are able to describe any turbulent field evolution (hence the "deterministic" connotation) for common fluids, but no general solution is available. The strong nonlinearity of the Navier-Stokes equations makes it impossible to give an *a priori* estimate of the evolution of perturbations in a turbulent flow. Hence the chaotic nature of turbulence. Figure 1 also shows how the size of the involved structures may differ by many order of magnitude. Although the energy distribution over these scales

Figure 1: St. Helene's eruption

may appear at first sight completely unorganized, experimental data as well as Kol-

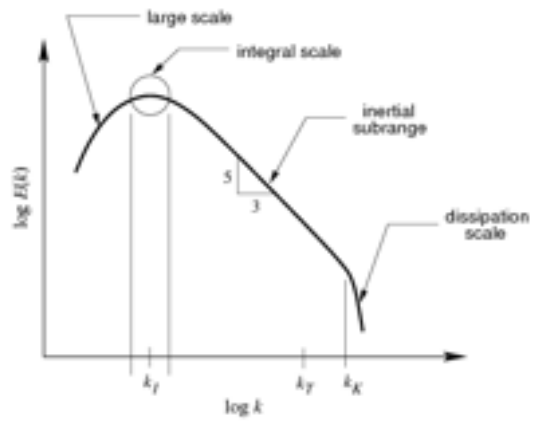

Figure 2: Turbulence Energy Spectrum

mogorov's theory [1] demonstrate that the turbulent kinetic energy distribution over the scales can be represented by the energy spectrum shown in Figure 2. Different characteristic lengthscale can be here identified through the corresponding wavenumbers. The integral lengthscale l_I (k_I) identifies the energy containing scales. It can be expressed by

$$l_I = \frac{1}{\|u'\|_{L2}^2} \int_{-\infty}^{\infty} u'(\mathbf{x},t)u'(\mathbf{x}+\mathbf{r},t)d\mathbf{r} \tag{1}$$

where u' is a fluctuation with respect to the averaged velocity and $\|\cdot\|$ is the L2-norm. From the integral lengthscale, energy is transfered to smaller scales down to Kolmogorov's scale η (k_K) that is given by

$$Re_\eta = \frac{u_\eta \eta}{\nu} = 1 \tag{2}$$

where *Re* is the Reynolds non dimensional number, ν is the kinematic viscosity and u_η is the characteristic velocity of Kolmogorov's scale. The *Re* number can be seen as the ratio of diffusion and convection characteristic times. The fact that $Re_\eta = 1$ says that η is the dissipative scale where kinetic energy is transformed into heat. As reported in Figure 2 the slope of the spectrum plot between k_I and k_K is $-5/3$ (when compressible flow effects are weak). This is a result of Kolmogorov's theory [1] that has been experimentally validated. This range of wavenumbers is called *inertial range*. The fact that this feature of turbulence is statistically reproduced by all the turbulent flows confirms their deterministic nature and provides a link for modelling strategies. Another important lengthscale reported in Figure 2 is the Taylor scale λ_T (k_T). This is an index of the position in the wave number space of the inertial range.

In order to study turbulent flows, due to the lack of a general analytical solution, scientists must numerically solve the Navier-Stokes equations. A complete and reliable solution should resolve all the wavenumbers down to Kolmogorov's scale η. This approach does not require any modelling and it is called *Direct Numerical Simulation* (DNS). Nevertheless, performing a DNS is usually not possible for practical applications, where the Reynolds number *Re* based on the domain characteristic dimension *L* is too high. It can be shown for the lengthscale separation that

$$\frac{l_I}{\eta} \sim Re^{\frac{3}{4}} \tag{3}$$

thus in 3D calculations one will need more than $Re^{\frac{9}{4}}$ grid points to perform a DNS calculation. Since in practical applications it is easy to find $Re_L \sim O(10^6)$ or higher, one can understand how the computational effort necessary to perform a DNS is not affordable by any present computer. To given an idea, the physical time required to perform a time step on a grid with $4.5 \cdot 10^6$ nodes, with a single core of a core2 duo Intel processor P8700 and the HeaRT code used in this work, is approximately 25 s. The simulated time during a numerical time step is $O(10^{-8})$ s.

In order to overcome the computational cost of a DNS, two modelling strategies are available:

- *Large Eddy Simulation* (LES): only a part of the spectrum is directly simulated while the highest frequencies are modelled. This approach allows to retain the unstationary features of turbulence and the results have an high level of reliability. The computational effort is still quite heavy.

- *Reynolds Average Navier Stokes* (RANS): all the turbulent spectrum is modelled and the time dependence is removed from the solution. It is the most widely spread technique because of its low computational cost. Nevertheless RANS models are complex and their applicability not certain. Calibration constants may change from a configuration to another and the final results are thus not so reliable.

The LES approach is thus growing in importance since, when a sufficient portion of the energy spectrum is resolved, it is the only available and reliable tool with prediction capability for complex flows. In the present work this features will be coupled with new techniques developed for the dispersed phase in order to obtain a predictive tool for dispersed multiphase flows under dilute conditions.

Physics of the dispersed phase

Dispersed multiphase flows involve different physical phenomena each of them characterized by a proper time and length scale. For example, a particle moving in a carrier phase is subjected to the effects of several forces (drag, lift, added mass...etc); when the considered particle is not rigid, his shape and integrity depend on the balance of the pressure, viscous stresses and surface tension. Furthermore, when mass exchanges take place at the particle interface they introduce a continuous variation of the considered forces, caused by the change of particle dimensions. This large variety of phenomena and associated scales imposes to carefully choose the modelling strategy looking for the phenomena that are negligible or that can be evaluated by simple relations, in order to develop a reliable but also usable model.

Following the above considerations, the first thing to be done is to provide a classification of the different possible regimes for dispersed multiphase flows, and to select then the conditions the model to be developed is supposed to be applied to. The first classification that can be easily found in the literature is related to the different levels of coupling between the carrier phase and the dispersed ones. This classification is based on the dispersed phase volume fraction α; another useful parameter to understand the kind of interaction between particles and turbulence is the local Stokes number St, which is the ratio between a particle response time to the aerodynamic forces and a characteristic time of turbulence. The level of coupling is generally classified into four degrees [3]; in Figure 3 the classification for particle-laden flows is reported. Coupling regimes are classified into

- one-way: whereby the particle motion is affected by the continuous phase but not vice-versa. This is the case of dilute dispersions of small particles that do not exchange mass with the carrier flow;

- two-way: whereby the dispersed phase affects the continuous phase through the inter-phase coupling, e.g. (mass, momentum and energy exchange). These are the conditions typically met inside fuel spray combustors as well as in powder burners, far enough from the injector, where the fuel volume fraction is small enough to neglect particle-particle interactions. Under these conditions small particles (i.e. small St) will subtract energy to the turbulent scales while larger particles (higher St) will transfer energy to the scales comparable to their wake

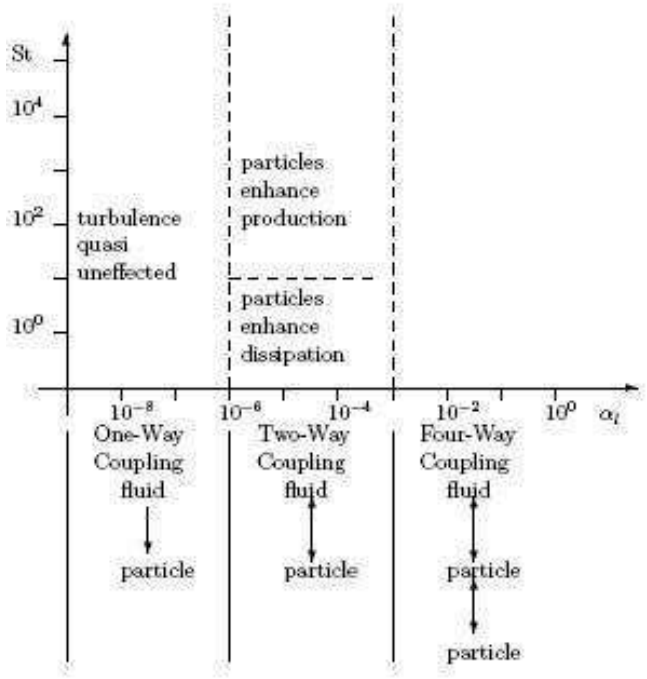

Figure 3: Turbulent particle laden flow regimes. Adapted from reference [2]

dimension;

- three-way: whereby individual particle flow disturbances locally affect the motion of the other nearby particles, i.e. fluid-dynamic interactions between particles;

- four-way: whereby particle collisions are present and have an influence on the overall particle motion.

Note that in Figure 3 the range for three-way coupling is not shown explicitly because, for particle laden flows, it overlaps the four-way coupling one: when particles are so close to each other to feel the interaction through the aerodynamic disturbances induced by the particles themselves, it is likely they will also collide.

In the present work dilute conditions for inertial particles are assumed. This assumption allows not to model particle-particle interactions and to focus on the dispersed phase evolution under conditions that are of interest in real combustor applications. Consider, for example, a spray injector in a gas-turbine combustor: few millimeters after the fuel injection the spray is completely developed and the fuel volume

fraction is sufficiently small to justify the use of a two-way coupling model. It seems therefore reasonable to separately model the spray injection, instead of conditioning the model for the all chamber to account for conditions that will only occur in a small portion of the domain. Similar considerations hold for coal powder entrained flow reactors or slurry reactors. Since the present work is oriented towards this kind of applications, only two-way coupling effects will be accounted for in the model and particle-particle interactions will be neglected. Furthermore the assumption of dilute conditions allows to estimate the needed source terms in the carrier phase equations by a proper averaging procedure of the exchange terms calculated for a single particle, while under three-way coupling assumption this would not be strictly possible.

The second step is to determine the mass, momentum and energy exchange mechanism for the isolated particle. The momentum transfer between particle and carrier phase depend on the force F_p acting on the particle; this force can be splitted in different contributions [4]

$$\sum F_p = F_D + F_g + F_L + F_S + F_H + F_W \tag{4}$$

where F_D is the aerodynamic drag force, F_g is the gravity force, F_L is the lift force, F_S is the Tchen force, F_H is the Basset History force and F_W is the wall interaction force. F_S takes into account the acceleration of the carrier flow at the position occupied by the particle while the history force accounts for its wake development. The above separation is not always valid as there can be non linear interactions between various forces but typically they are small enough to be neglected. A preliminary estimation of the weight of each force shows (see [2]) that for heavy particles the prominent forces acting are the gravity force, the drag force and the Basset force. The history force scales like the inverse of the diameter while the drag force scales as the square of inverse diameter [2]; the drag force is thus the dominant force, together with the gravity, for small particles. In our model the drag force for the single particle is modeled by an expression based on the Stokes drag (strictly valid only for creeping flows) corrected by a factor f function of the particle Reynolds number Re_p

$$Re_p = \frac{|u_{f@p} - c_p| d_p}{\nu_f} \tag{5}$$

where $u_{f@p}$ is the carrier phase velocity at the particle location, c_p is the particle velocity, d_p is the particle diameter. With this assumption the drag force acting on a particle can be expressed by $F_D = \frac{-(c_p - u_{f@p})}{\tau_p}$. Here τ_p is the particle relaxation

time that can be interpreted as the time taken by the particle to reach the 63 % of the carrier phase velocity, when the particle is initially at rest and the carrier phase velocity is constant. This parameter is used, together with a characteristic time τ_f of the carrier phase (e.g. a turbulent time scale τ_f^t), to build the non dimensional Stokes number $St = \frac{\tau_p}{\tau_f}$. The Stokes number is a very important parameter since it measures the possibility for the particle to follow the velocity fluctuations corresponding to a given scale of the fluid velocity field.

Regarding the mass and energy exchange, they will not be an object of the present work since the latter will be focused on the transport model improvement. In addition, the mass exchange model depends on the particular fuel and operational range and will therefore not be treated in this work.

As to particle heating, when practical applications are considered, the models adopted in the literature are usually rather simple. This is due to the fact that particle heating should be modelled taking into account the effects of turbulence, combustion and all related phenomena in realistic 3D enclosures. Hence, a compromise between the complexity of the involved phenomena and the computational efficiency of the adopted models is an essential precondition for a CFD tool. A complete model should account for:

- the effect of convection;
- the effect of the flow around the particle (e.g. different mass flow between upstream and downstream stagnation point);
- fractional mass exchange of multicomponent fuels;
- temperature distribution inside the particle;
- the effect of internal recirculation caused by the frictional stresses on the surface (for liquid fuels);
- other minor phenomena.

Several models can be found in the literature [5]; the so called "Infinite conductivity model" is usually selected because of its simplicity. In this model the particle inner temperature is radially constant but variable with time. Since this model is developed for a particle in a stagnant environment an empirical correlation is used to account

for convection (Ranz-Marshall). This model has been implemented in the CFD code used for the validation of the transport model but, since no reactive validation could be performed during this work, it has not been validated.

From the brief review of the phenomena concerning an isolated particle in an hot convective environment, one can easily see the importance of the particle diameter. In real devices a spectrum of particle sizes is usually found. These dimensions range from below the micron up to the hundred of microns, depending on the kind of reactor that is being considered. It is worth to say that even if it were possible to inject only particles of a given size, the cloud becomes polydispersed [6]. This is due to the different mass exchange rates experienced by the particles in different zones of the combustor. From experiments and theoretical observation many researchers developed different size distribution functions, but, since many of the models are developed for monodisperse distributions, it is useful to define some representative diameters that can reproduce some aspect of the polydispersed nature of the spray. They are usually defined as

$$D_{ij} = \frac{\int D^i * f(D) dD}{\int D^j * f(D) dD} \tag{6}$$

The most known are the Sauter diameter D_{32} and the surface diameter D_{20}. The first one has the same volume to surface ratio of the whole particle cloud and for this reason is frequently used in combustion; the latter has the same surface of the whole particle system and is sometimes preferred to the Sauter diameter for problems in which the mass exchange rate is particularly important (e.g. ignition).

State of the art

In scientific literature several modeling strategies for the simulation of multiphase dispersed flows are present; they can be roughly divided in two classes, Lagrangian and Eulerian, with respect to the framework in which the secondary phase is described. In the past, LES technique has been used together with a Lagrangian description for the dispersed phase [7]. This is due to the easiness in modeling a single particle behavior with respect to model the behavior of a group of particles, present in a given control volume at a given time instant. This historical trend makes it easy today to find LES simulations of reacting two-phase flows in literature [8], performed with this approach.

Greater attention has been more recently gained by the Euler-Euler formulation. This is mainly due to the massive diffusion of parallel computation techniques as a standard to increase computational capacity. The parallelization of a numerical code for two-phase dispersed flow application with the Eulerian-Lagrangian (EL) approach is a difficult task. Workload distribution among processors is not straightforward. In addition the large amount of informations that have to be exchanged among the CPUs, and the time needed to do it, tend to decrease parallelization efficiency. This is especially true when particle distribution is not uniform throughout the domain [9].

A two-fluid Eulerian model was first proposed by Druzhinin and Elghobashi [10]. This model laid on the assumption that particle equations were obtained by filtering on a length scale Δ smaller than the smallest characteristic scale l_p of particle velocity field. This hypothesis ensures the unicity of $\boldsymbol{u}_p$ at the scale l_p.

Simonin et al. [11] proposed a model for dispersed two-phase flows, based on the separation of particle velocities into a "mesoscopic" correlated part, representative of a group of particles, and an uncorrelated part proper of each single particle. They also proposed a correlation, strictly holding for Homogeneous Isotropic Turbulence (HIT), for the evaluation of the turbulent kinetic energy part due to uncorrelated motion. Kaufmann [2] proposed models for the second order velocity moments and the terms appearing after filtering the equations of Simonin et al. [11] model, under the assumption of non-colliding particles. Moreau [12] made an *a priori* evaluation of the closures proposed by Kaufmann [2] by applying them to Direct Particle Simulation (DPS) results. Selected models were then applied in LES simulations of particle laden flows [13] and confined bluff-body gas-solid flows [9].

All the cited models are strictly developed for monodisperse sprays but extension to polydispersion are also present in literature. The classical way to extend a model to polydispersion is called Sectional Method. The size PDF is splitted in n classes, each of them representing a monodisperse distribution. For each class it is possible to apply one of the cited model adding proper relations to define the migration of particles between different classes. Another way is the so called "Presumed Shape PDF"[14] that calculates the deviation from monodispersion as moments of the PDF.

Summary of this work

In Chapter 1 the model equation for both continuous and dispersed phase will be presented. For the latter in particular the model discussed by Moreau [12] and further developed in [15] will be presented. The model applicability holds when inertial particles within dilute conditions are considered. These are the conditions typically met in industrial as well as in aeroengine burners, with the exception of the injector region, where the diluition assumption is often not met. A revised *Fractal Model* (FM) for the SGS terms closure is also presented. The coupling between continuous and dispersed phase will be treated by classic empiric correlations and mass exchange models taken from the literature.

In Chapter 2 the adopted numerical treatment for both phases is described. A robust numerical treatment for the dispersed phase, based on a *Finite Volume* ENO (Essentially Non Oscilatory) scheme is here proposed.

In Chapter 3 the validation of the adopted transport model and of the developed numerics is presented. The obtained results are described and criticized.

Chapter 1

Mathematical model

1.1 Continuous phase model

When two-phase flows are considered, great attention must be paid to the assumptions under which the adopted model is developed, since these assumptions will affect the transport equations that govern the evolution of the two-phase system. The model developed in the present work is based on two main hypothesis: a) a condensed phase is dispersed in a continuous gaseous phase; b) dilute conditions are assumed. Under these hypothesis two way coupling between phases can be assumed, meaning that the equations governing each phase evolution present terms that account for the interaction with the other phase. Under dilute conditions it is also possible to model this interaction in the continuous phase by simply adding source terms to the single phase balance equations.

Let a mixture of N_s ideal gases in local thermodynamic equilibrium and chemical non-equilibrium be considered. The complete set of transport equations for the gas phase, that expresses the conservation of mass, momentum, energy and chemical species mass fractions, together with the thermodynamic state equation, is

- Conservation of Mass

$$\frac{\partial \rho_f}{\partial t} + \nabla \cdot \left(\rho_f \mathbf{u}_f\right) = -\Gamma_p \tag{1.1}$$

- Conservation of Momentum

$$\frac{\partial \rho_f \mathbf{u}_f}{\partial t} + \nabla \cdot \left(\rho_f \mathbf{u}_f \mathbf{u}_f\right) = \nabla \cdot \underline{\mathbf{S}} + \rho_f \sum_{i=1}^{N_s} Y_i \mathbf{f}_i - \Gamma_p \mathbf{u}_p + \alpha_p \rho_p \left(\frac{\mathbf{u}_p - \mathbf{u}_f}{\tau_p}\right) \tag{1.2}$$

- Conservation of Energy (internal + kinetic)

$$\frac{\partial}{\partial t}\rho_f(\mathcal{E}+\mathcal{K})+\nabla\cdot[\rho_f\mathbf{u}_f(\mathcal{E}+\mathcal{K})]=\nabla\cdot(\underline{\mathbf{S}}\mathbf{u}_f)-\nabla\cdot\mathbf{q} \tag{1.3}$$

$$+\rho_f\sum_{i=1}^{N_s}Y_i\mathbf{f}_i\cdot(\mathbf{u}_f+\mathbf{V}_i)+\underbrace{\frac{\alpha_p\rho_p}{\tau_p}(\mathbf{u}_p-\mathbf{u}_f)\cdot\mathbf{u}_f}_{E_{pf}}+\underbrace{\frac{\alpha_p\rho_p}{\tau_p}(\mathbf{u}_p-\mathbf{u}_f)^2}_{Q_{pf}}$$

$$-\underbrace{\Gamma_p H_p}_{\Gamma_h}-\Gamma_p\left(\frac{1}{2}\mathbf{u}_p\cdot\mathbf{u}_p\right)-\Pi_p$$

- Conservation of Species Mass Fraction

$$\frac{\partial\rho_f Y_i}{\partial t}+\nabla\cdot\left(\rho_f\mathbf{u}_f Y_i\right)=-\nabla\cdot\mathbf{J}_i+\rho_f\omega_i-\Gamma_{p,i} \tag{1.4}$$

- Thermodynamic State Equation

$$p=\rho_f\sum_{i=1}^{N_s}\frac{Y_i}{W_i}\mathcal{R}_u T_f \tag{1.5}$$

The terms E_{pf} and Q_{pf} in equation (1.3) represent the work done by the aerodynamic force on the continuous phase and the energy dissipation into heat during aerodynamic interaction respectively. When larger particles are considered (large Re_p) part of Q_{pf} should account for the energy transferred to the turbulent structures in the particle wake. However, in the limit of small particles, the energy injection will occur at dissipative scales and the assumption that all Q_{pf} is dissipated into heat is acceptable.

In equations (1.3) and (1.4) the relation between the mass flux $\mathbf{J}_i$ of the i^{th} species due to diffusion and the corresponding diffusion velocity $\mathbf{V}_i$ has been used

$$\mathbf{J}_i=\rho_f Y_i\mathbf{V}_i \tag{1.6}$$

Equations (1.1)-(1.5) must be coupled with the constitutive equations which describe the type of flow, and in particular its behavior in relation to molecular properties.

It should be noted that summation of all species conservation equations in (1.4) yields total mass conservation equation (1.1), so that these N_s+1 equations are linearly dependent and one of them is redundant. Furthermore, to be consistent with mass

conservation, the diffusion fluxes and source terms due to chemical reactions and mass exchange between the two phases must satisfy

$$\sum_{i=1}^{N_s} \mathbf{J}_i = 0 \qquad \sum_{i=1}^{N_s} \omega_i = 0 \qquad \sum_{i=1}^{N_s} \Gamma_{p,i} = \Gamma_p \tag{1.7}$$

where Γ_p is the overall mass flux from the dispersed towards the gas phase while $\Gamma_{p,i}$ is the fraction of such mass flux involving the i^{th} species.

After subtracting from (1.3) the conservation equation for the kinetic energy[16], the energy equation can be written in terms of enthalpy $\mathcal{H}_f$ as:

$$\begin{aligned} \frac{\partial}{\partial t}\left(\rho_f \mathcal{H}_f\right) + \nabla \cdot \left(\rho_f \mathcal{H}_f \mathbf{u}_f\right) &= \frac{Dp}{Dt} - \nabla \cdot \mathbf{q} + \Phi_f - Q_{loss} + \rho_f \sum_{i=1}^{N_s} Y_i \mathbf{f}_i \cdot \mathbf{V}_i \\ &\quad - \underbrace{\Gamma_p H_p}_{\Gamma_h} - \Pi_p + Q_{pf} \end{aligned} \tag{1.8}$$

Here $\mathbf{q}$ is the heat flux; $\Phi_f = \underline{\tau} : \underline{\nabla \mathbf{u}}$ is the dissipation function, being $\underline{\tau}$ the viscous part of the stress tensor; Q_{loss} the heat loss (e.g., by radiation), $\mathbf{f}_i$ the body force per unit of mass acting on the i^{th} chemical species that diffuses at velocity $\mathbf{V}_i$.

The heat flux $\mathbf{q}$ is given by three contributions, Fourier, Dufour and that associated to the diffusion of each species transporting its own enthalpy:

$$\mathbf{q} = \mathbf{q}_F + \mathbf{q}_D + \mathbf{q}_{V_i} = -k^f \nabla T_f + \mathbf{q}_D + \rho_f \sum_{i=1}^{N_s} Y_i \mathcal{H}_{f,i}(T_f) \mathbf{V}_i \tag{1.9}$$

1.1.1 Filtered conservation equations

It is common practice, while studying turbulent flows, to treat velocities and scalars with classical Reynolds averaging, where the quantity q is split into a mean $\overline{q}$ and a deviation from the mean denoted by q'. Nevertheless, in turbulent flames, fluctuations of density are observed because of the thermal heat release and classical Reynolds averaging induces some additional difficulties. For example, averaging the mass balance equation leads to:

$$\frac{\partial \overline{\rho}_f}{\partial t} + \frac{\partial}{\partial x_i}\left(\overline{\rho_f u_i} + \overline{\rho'_f u'_i}\right) = 0 \tag{1.10}$$

where the velocity/density fluctuations correlation $\overline{\rho'_f u'_i}$ appears.
To avoid the explicit modeling of such correlations, a Fávre (mass weighted) average $\widetilde{[]}$ is introduced and the generic quantity q is then decomposed into $q = \widetilde{q} + q''$ where

$$\widetilde{q} = \frac{\overline{\rho_f q}}{\overline{\rho_f}} \tag{1.11}$$

The objective of Large Eddy Simulation is to explicitly compute the largest structures of the flow (typically the structures larger than the computational mesh size), while the effects of the smaller ones are modeled. In LES, the relevant quantities q are filtered in the spectral space (components greater than a given cut-off frequency are suppressed) or in the physical space (e.g. weighted averaging in a given volume). The filter operation is defined by:

$$\overline{f}(x) = \int_D f(x') \, G_\Delta(x, x') \, dx' \tag{1.12}$$

where G_Δ is the filter function. The latter must have the following properties:

1. $G_\Delta(x) = G_\Delta(x')$;
2. $\int_D G_\Delta(x, x') \, dx' = 1$;
3. $G_\Delta(x)$ small outside the compact domain $\left[x - \frac{\Delta}{2}, x + \frac{\Delta}{2}\right]$.

Standard filters are:

- A cut-off filter in the spectral space:

$$\overline{G_\Delta}(k) = \begin{cases} 1 & \text{if } k \leq \pi\Delta \\ 0 & \text{otherwise} \end{cases} \tag{1.13}$$

  where k is the spatial wave number. This filter preserves the length scales greater than the cut-off length scale 2Δ.

- A box filter in the physical space:

$$G_\Delta(x_1, x_2, x_3) = \begin{cases} \frac{1}{\Delta} & \text{if } |x_i| \leq \frac{\Delta}{2} \\ 0 & \text{otherwise} \end{cases}$$

  where (x_1, x_2, x_3) are the spatial coordinates of the location x. This filter corresponds to an averaging of the quantity q over a box of size Δ.

- A Gaussian filter in the physical space:

$$G_\Delta(x_1,x_2,x_3) = \left(\frac{6}{\pi\Delta^2}\right)^{3/2} exp\left[-\frac{6}{\Delta^2}\left(x_1^2+x_2^2+x_2^2\right)\right]$$

By applying the filter operator to the system equations, balance equations for the filtered quantities $\overline{q}$ and $\widetilde{q}$ are obtained. In this work, the filter operation is implicitly defined by the mesh size. The uncertainties related to the procedure of exchanging the order of the filter and differential operators (commutation errors), are neglected and assumed to be incorporated in the sub-grid scale modeling. It has however been demonstrated that the commutation error is $O(\Delta^2)$ [17]. Fávre filtering leads to a set of equations formally similar to the Reynolds averaged balance equations:
Mass:

$$\frac{\partial\overline{\rho}_f}{\partial t}+\frac{\partial}{\partial x_j}(\overline{\rho}_f\widetilde{u}_{f,j}) = -\overline{\Gamma}_p \tag{1.14}$$

Momentum:

$$\begin{aligned}\frac{\partial}{\partial t}(\overline{\rho}_f\widetilde{u}_{f,i})+\frac{\partial}{\partial x_j}(\overline{\rho}_f\widetilde{u}_{f,i}\widetilde{u}_{f,j}) &= -\frac{\partial\overline{p}}{\partial x_i}+\frac{\partial\overline{\tau}_{ij}}{\partial x_j}-\frac{\partial\tau_{ij}^{SGS}}{\partial x_j} \\ &- \overline{\Gamma_p u_{p,i}}+\overline{\alpha_p\rho_p\left(\frac{u_{p,i}-u_{f,i}}{\tau_p}\right)}+\overline{\rho}_f\sum_{s=1}^{N_s}\widetilde{Y_s f_{s,i}}\end{aligned} \tag{1.15}$$

$$\overline{\tau}_{ij} = \overline{\mu}\left(\frac{\partial\widetilde{u}_{f,i}}{\partial x_j}+\frac{\partial\widetilde{u}_{f,j}}{\partial x_i}\right)-\frac{2}{3}\overline{\mu}\frac{\partial\widetilde{u}_{f,k}}{\partial k}\delta_{ij} \tag{1.16}$$

$$\tau_{ij}^{SGS} = \overline{\rho}_f\widetilde{u_{f,i}u_{f,j}}-\overline{\rho}_f\widetilde{u}_{f,i}\widetilde{u}_{f,j} \tag{1.17}$$

Species equations:

$$\frac{\partial}{\partial t}(\overline{\rho}_f\widetilde{Y}_i)+\frac{\partial}{\partial x_j}\left(\overline{\rho}_f\widetilde{Y}_i\widetilde{u}_{f,j}\right) = -\frac{\partial}{\partial x_j}\left(\overline{\rho}_f\widetilde{Y}_i\widetilde{V}_{ij}\right)+\overline{\rho}_f\widetilde{\omega}_i-\frac{\partial J_{ij}^{SGS}}{\partial x_j}-\overline{\Gamma}_{p,i} \tag{1.18}$$

$$J_{ij}^{SGS} = \overline{\rho}_f\widetilde{Y_i u_{f,j}}-\overline{\rho}_f\widetilde{Y}_i\widetilde{u}_{f,j} \tag{1.19}$$

where the assumption has been made, and will be used in the further development, that the subgridscale effects due to diffusion, arising from $\widetilde{J_{ij}}$, may be neglected with respect to those due to the SGS species transport $\mathbf{J}_i^{SGS}$.

As to the energy equation:

$$\frac{\partial}{\partial t}\left(\overline{\rho}_f \widetilde{\mathcal{H}}_f\right) + \frac{\partial}{\partial x_j}\left(\overline{\rho}_f \widetilde{\mathcal{H}}_f \widetilde{u}_{f,j}\right) = \frac{D\overline{p}}{Dt} - \frac{\partial}{\partial x_j}\left(\overline{q}_j + q_j^{SGS}\right) + \overline{\Phi}_f - \overline{Q}_{loss} \tag{1.20}$$

$$+\overline{\rho}_f \sum_{i=1}^{N_s} \widetilde{Y}_i \widetilde{f}_{ij} \widetilde{V}_{ij} - \overline{\Gamma}_h - \overline{\Pi}_p + \overline{Q}_{pf}$$

$$q_{h,j}^{SGS} = \overline{\rho}_f \widetilde{\mathcal{H}_f u_{f,j}} - \overline{\rho}_f \widetilde{\mathcal{H}}_f \widetilde{u}_{f,j} \tag{1.21}$$

Again the subgridscale heat flux due to diffusion effects has been considered negligible with respect to SGS heat transport $\mathbf{q_h}^{SGS}$.

Finally, the filtered equation of state is

$$\overline{p} = \overline{\rho}_f \sum_{i=1}^{N_s} \mathcal{R}_u \widetilde{\frac{Y_i}{W_i} T_f} \simeq \overline{\rho}_f \sum_{i=1}^{N_s} \mathcal{R}_u \frac{\widetilde{Y}_i}{W_i} \widetilde{T}_f \tag{1.22}$$

Another important assumption that has been adopted in the development of the present model is that particles present a high value of their inertia. The meaning of this sentence and its importance in the development of the model is explained in [15]. Among other implications, the restriction to highly inertial particles allows to assume that particle motion is not influenced by the unresolved scales of turbulence. A first exploitation of this statement leads to the absence of SGS modeling in the dispersed phase balance equations. Another turnaround is the possibility to model the filtered source terms that account for phase interaction, by means of their unfiltered form, where gas-phase filtered variables take the place of their unfiltered values. This possibility is also granted by the fact that most of the source terms accounting for phase interaction are modeled after semi-empirical correlations (see for example [2]) that implicitly take into account the turbulence effects. Nevertheless, these correlations are based on the gas-particle relative velocity and correction may be necessary when this parameter is small but the turbulence intensity is high. In such a situation the correlations may in fact predict a laminar behavior. These effects are probably more important in the evaluation of the mass (Γ_p) and heat (Π_p) exchange than in aerodynamics forces, since when the gas-particle relative velocity is low the particle momentum is close to its equilibrium, while temperature and species concentrations may be far from their own. Nevertheless, the improvement of the mass and heat exchange source terms goes beyond the objectives of the present work, being the latter oriented to improve the transport model and numerics. Therefore, these topics will not be addressed here.

The quantities to be modelled are:

- the unresolved Reynolds stresses $\underline{\tau}^{SGS}$, requiring a subgrid scale turbulence model;
- the unresolved molecular transport fluxes $\mathbf{J}_i^{SGS}$;
- the unresolved heat transport fluxes $\mathbf{q}^{SGS}$;
- the filtered chemical reaction rate $\widetilde{\omega}_i$;
- all the source terms accounting for phase interactions.

The filtered balance equations presented in this section, coupled with subgrid scale models, may be numerically solved to simulate the unsteady behavior of the filtered fields.

1.1.2 The Constitutive Equations

Each material has a different response to an external force, depending on the properties of the material itself. The constitutive equations describe this behavior. In particular, for a gas mixture they should model the stress-strain relation $\underline{\mathbf{S}} - \underline{\mathbf{E}}$, the heat flux $\mathbf{q}$ and the species mass flux $\mathbf{J}_i$. In the preceding section the hypothesis has been made that SGS effects other than those accounted for in the source terms and those due to small scale transport are negligible with respect to these contributions. Given this assumptions, all the quantities that will appear in the following development must be considered as filtered values. The average signs $\overline{[]}$ and $\widetilde{[]}$ are thus dropped.

The Diffusive Momentum Flux

For all gases that can be treated as a continuum, and most liquids, it has been observed that the stress at a point is linearly dependent on the rates of strain (deformation) of the fluid. A fluid that behaves in this manner is called a Newtonian fluid. With this assumption, it is possible to derive a general deformation law that relates the stress tensor $\underline{\mathbf{S}}$ to the pressure and velocity components:

$$\underline{\mathbf{S}} = \left(-p + \lambda \nabla \cdot \mathbf{u}_f\right) \underline{\mathbf{I}} + 2\mu \underline{\mathbf{E}} = -p\underline{\mathbf{I}} + \underline{\tau} \tag{1.23}$$

where $\underline{\mathbf{E}}$ is the strain rate, μ is the coefficient of viscosity (dynamic viscosity) and λ is the second coefficient of viscosity. The two coefficients of viscosity are related to the coefficient of bulk viscosity μ_b by the expression $\mu_b = 2/3\mu + \lambda$. In general, it is believed that μ_b is negligible except in the study of the structure of shock waves and in the absorption and attenuation of acoustic waves. With this assumption (Stokes hypothesis), λ is equal to $-2/3\,\mu$, and the viscous stress tensor becomes:

$$\tau_{ij} = \lambda \frac{\partial u_{f,i}}{\partial x_i} + 2\mu \left[\frac{1}{2} \left(\frac{\partial u_{f,i}}{\partial x_j} + \frac{\partial u_{f,j}}{\partial x_i} \right) \right] . \tag{1.24}$$

Pressure at the macroscopic level corresponds to the microscopic transport of momentum by means of molecular collisions in the direction of molecules motion. Instead, molecular momentum transport in other directions is what at macroscopic level is called viscosity. They are of different nature. In terms of work done, when continuous distribution are considered, pressure produces reversible transformations (changes of volume), while viscous stresses produce irreversible transformations where dissipation of energy into heat occurs.

The Diffusive Heat Flux

The heat flux **q** for a gaseous mixture of N_s chemical species consists of three different transport contributions.

The first is the heat transfer by conduction, modeled by the Fourier's law. At the microscopic level it is due to molecular collisions: since kinetic energy and temperature are equivalent, molecules with higher kinetic energy (at higher temperature) "energize" collisionally the ones with less kinetic energy (at lower temperature); in the continuum view, heat is transfered by means of temperature gradients.

The second heat transport contribution is due to molecular diffusion, acting in multicomponent mixtures and driven by concentration gradients: where $\nabla Yi \neq 0$, each species diffuses with its own velocity V_i. In this way each molecule transports its own enthalpy contribution; this means that there is energy transfer even in a gas at uniform temperature, or in a rarefied gas (with negligible conduction).

The third heat transport mechanism is the so called Dufour effect. The Onsager principle of microscopic reversibility in the thermodynamics of irreversible processes implies that if temperature gradients cause species diffusion (thermo-diffusive or Soret effect), concentration gradients must cause a reciprocal (Dufour effect) heat flux. The

Dufour effect is neglected. [18].

The total energy flux $\mathbf{q}$ is finally modeled:

$$\mathbf{q} = -k^f \nabla T_f + \rho_f \sum_{i=1}^{N_s} \mathcal{H}_{f,i} Y_i \mathbf{V}_i + \mathcal{R}_u T_f \sum_{i=1}^{N_s} \sum_{j=1}^{N_s} \frac{X_j \alpha_i}{W_i D_{ij}} \left(\mathbf{V}_i - \mathbf{V}_j \right) \ . \tag{1.25}$$

where α_i is the thermodiffusion coefficient of the i^{th} species

The Diffusive Species Mass Flux

To be useful, equation (1.4) requires the knowledge of diffusive species mass flux, $\mathbf{J}_i$, that expresses the relative motion of chemical species with respect to the motion of their (moving) center of mass. Within the continuum mechanics this motion can be expressed by a constitutive law rather than additional momentum equations for chemical species. Both modelling and calculation of individual species diffusive mass fluxes is not easy. The distribution of N_s chemical species in a multicomponent gaseous mixture, at low density, is rigorously obtained by means of kinetic theory [18]

$$\begin{aligned} \nabla X_i \ = \ & \underbrace{\sum_{i=1}^{N_s} \frac{X_i X_j}{D_{ij}} \left(\mathbf{V}_j - \mathbf{V}_i \right)}_{DV} + \underbrace{\left(Y_i - X_i \right) \frac{\nabla p}{p}}_{PG} + \\ & + \underbrace{\frac{\rho_f}{p} \sum_{j=1}^{N_s} Y_i Y_j \left(\mathbf{f}_i - \mathbf{f}_j \right)}_{BF} + \underbrace{\sum_{j=1}^{N_s} \frac{X_i X_j}{\rho_f D_{ij}} \left(\frac{\alpha_j}{Y_j} - \frac{\alpha_i}{Y_i} \right) \frac{\nabla T_f}{T_f}}_{SE} \end{aligned} \tag{1.26}$$

where D_{ij} is the binary diffusion coefficient of species i into the species j, X_j and Y_j are the molar and the mass fraction of the j^{th} species respectively, $\mathbf{f}_j$ the body force per unit mass, acting on species j, α_j the thermodiffusion coeffcient of species j. Equations (1.26) are referred to as the Maxwell-Stefan equations, since Maxwell [19, 20] suggested them for binary mixtures on the basis of kinetic theory, and Stefan [21, 22] generalized them to describe the diffusion in a gas mixture with N_s species. The main feature of (1.26) is that they couple inextricably all diffusion velocities $\mathbf{V}_j$, and thus all fluxes to all concentrations X_j and Y_j and their gradients. According to (1.26), concentrations gradients (e.g., $\nabla X i$) can be physically created by:

- differences in Diffusion Velocities (*DV*)

- Pressure Gradients (*PG*) ("pressure diffusion")
- differences in Body Forces (*BF*) per unit mass acting on molecules of different species;
- thermo-diffusion, or Soret Effect (*SE*), i.e., mass diffusion due to temperature gradients, driving light species towards hot regions of the flow.

This last effect, often neglected, is nevertheless known to be important, in particular for hydrogen combustion, and in general when very light species play an important role. The Soret effect has the Dufour effect as reciprocal, but is more important than this. The linear system (1.26) for the $\mathbf{V}_j$ has size N_s x N_s and requires knowledge of $Ns(Ns-1)/2$ diffusivities. Only N_s-1 equations are independent, since the sum of all diffusion fluxes must be zero. This system must be solved in each direction of the frame of reference (coordinate system), at every computational node and, for unsteady flows, at each time step. Extracting the diffusion velocities is a mathematically difficult task, therefore, simplified models, such as the Fick's law and the Hirschfelder and Curtiss' law, are preferred in most CFD (Computational Fluid Dynamics) computations. These simplified models still involve the estimation of individual chemical species diffusion coefficients into the rest of the mixture; also at this step some simplifications are usually assumed. These will be analyzed in the hereafter.

Many combustion codes use a simplified model for the diffusion velocities, the Fick's law approximation, assuming

- binary mixture (two species *A* and *B*),
- thermo-diffusion negligible,
- $\mathbf{f}_A = \mathbf{f}_B$

This law is usually adopted for the sake of simplicity also for multi- component mixtures (more than binary):

$$\mathbf{J}_i = \rho_f Y_i \mathbf{V}_i = -\rho_f D \nabla Y_i \tag{1.27}$$

A more accurate (but still simple) approximate formula for diffusion velocities in a multicomponent mixture is that of Hirschfelder and Curtiss, which has been used in this work.

$$\mathbf{V}_i = -D_i \frac{\nabla X_i}{X_i} \tag{1.28}$$

with :

$$D_i = \frac{1 - Y_i}{\sum_{j=1,\ j\neq i}^{N_s} \frac{X_j}{D_{ji}}} \tag{1.29}$$

The coefficient D_i is not a binary diffusion but an equivalent diffusion coefficient of species i into the rest of the mixture. Mass conservation problem arises in calculations when inexact expressions for diffusion velocities are used (as when using Hirschfelder's or Fick's laws), and in general when differential diffusion effects are considered, i.e., the species diffusion coefficients are different. In fact, the diffusion velocities do not necessarily satisfy the constrain $\sum_{i=1}^{N_s} \mathbf{J}_i = \sum_{i=1}^{N_s} \rho_f Y_i \mathbf{V}_i = 0$. A simple empirical remedy to impose global mass conservation consists in subtracting any residual artificial diffusional velocity from the flow velocity in the species transport equations. In fact, summing all species transport equations, the mass conservation equation must be obtained, while it is found:

$$\frac{\partial \rho_f}{\partial t} + \nabla \cdot \left(\rho_f \mathbf{u}_f\right) = -\nabla \cdot (\rho_f \sum_{i=1}^{N_s} Y_i \mathbf{V}_i) \tag{1.30}$$

Thus, in order for the conservation of mass to be respected, a term $\rho_f \mathbf{V}^c$ involving a correction velocity $\mathbf{V}^c$ must be introduced. $\mathbf{V}^c$ is defined as

$$\mathbf{V}^c = -\sum_{i=1}^{N_s} Y_i \mathbf{V}_i \tag{1.31}$$

and assuming Hirschfelder's law holds, it becomes

$$\mathbf{V}^c = \sum_{i=1}^{N_s} \frac{W_i}{W_{mix}} D_i \nabla X_i \tag{1.32}$$

The correction velocity must be computed at each time step and added to the flow velocity in the species convective term. The corrected convective term of species transport equations must then become

$$\nabla(\rho_f \mathbf{u}_f Y_i) \rightarrow \nabla(\rho_f (\mathbf{u}_f + \mathbf{V}^c) Y_i) \tag{1.33}$$

With this "trick", any artificial flow due to the nonzero diffusional mass flux is thereby cancelled, and solving for $N_s - 1$ species and global mass, results into a "correct" concentration for the last N_s species (the last species can be obtained as $1 - \sum_{i=1}^{N_s - 1} Y_i$).

1.1.3 Some Thermodynamics Definitions

In a multi-species system the enthalpy, $\mathcal{H}_f(Y_i, T_f)$, is given by two contributions: one is the potential energy of the molecular force field (expressed in terms of formation energies that must depend on temperature because the molecular force field changes when temperature changes), and the other is the kinetic energy of molecules (sensible enthalpy), obtained considering all their degrees of freedom (expressed in terms of specific heat) and not only the effect of temperature T_f. The enthalpy $\mathcal{H}_f(Y_i, T_f)$ is defined as

$$\mathcal{H}_f(Y_i, T_f) = \sum_{i=1}^{N_s} Y_i \mathcal{H}_{f,i}(T_f) \tag{1.34}$$

and therefore

$$\mathcal{H}_f(Y_i, T_f) = \sum_{i=1}^{N_s} Y_i \left[h^0_{f_i}(T_f) + h_{s_i}(T_f) \right] = \sum_{i=1}^{N_s} Y_i h^0_{f_i}(T_f) + h_s(Y_i, T_f) \tag{1.35}$$

where Y_i is the mass fraction of the i^{th} chemical species, $h^0_{f_i}(T_f)$ and $h_{s_i}(T_f)$ are respectively the formation and the sensible enthalpies of the i^{th} species.

The sensible enthalpy is defined thermodynamically:

$$dh_s = C_p dT_f \tag{1.36}$$

and therefore

$$h_s(Y_i, T_f) = \int_{T_{f,r}}^{T_f} C_p(Y_i, T_f) dT + h_s(Y_i, T_{f,r}) \tag{1.37}$$

where $T_{f,r}$ is a reference temperature and $C_p(Y_i, T_f)$ is the specific heat at constant pressure given by

$$C_p(Y_i, T_f) = \sum_{i=1}^{N_s} Y_i C_{p_i}(T_f) \ . \tag{1.38}$$

Also the internal energy is defined thermodynamically:

$$de_s = C_v dT_f \tag{1.39}$$

and therefore

$$e_s(Y_i, T_f) = \int_{T_{f,r}}^{T_f} C_v(Y_i, T_f) dT + e_s(Y_i, T_{f,r}) \tag{1.40}$$

where $C_v(Y_i, T_f)$ is the specific heat at constant volume given by

$$C_v(Y_i, T_f) = \sum_{i=1}^{N_s} Y_i C_{v_i}(T_f) \ . \tag{1.41}$$

The relation between the sensible enthalpy and the internal energy is obtained by subtracting (1.40) from (1.37):

$$dh_s = de_s + (C_p - C_v)dT_f = de_s + R_g dT_f \tag{1.42}$$

having used

$$C_p - C_v = R_g \ . \tag{1.43}$$

The gas constant R_g is defined as

$$R_g = \frac{\mathcal{R}_u}{W_{mix}} = \frac{\mathcal{R}_u}{1/\sum_{i=1}^{N_s} Y_i/W_i} = \mathcal{R}_u \sum_{i=1}^{N_s} \frac{Y_i}{W_i} \tag{1.44}$$

where $\mathcal{R}_u$ is the universal gas constant, and W_{mix} and W_i are respectively the mixture and the single species molecular weight.

Energy Equation in Terms of T_f and C_p

The aim of this subsection is to derive the energy equation written in terms of the filtered temperature and specific heat at constant pressure starting from equation (1.20), since this is the form used in the HeaRT code used for validation in the present work. When termodynamic relations are applied to filtered quantities, terms accounting for subgrid scale effects should appear. This terms will be omitted in the following derivation and their effect will be thought as modelled in the SGS heat flux $\mathbf{q}^{SGS}$ together with $\mathbf{q_h}^{SGS}$.

The material derivative of enthalpy $\mathcal{H}_f(Y_i, T_f)$ can be calculated as:

$$\begin{aligned} \frac{D\mathcal{H}_f(Y_i,T_f)}{Dt} &= \frac{D\mathcal{H}_f(Y_i,T_f)}{DT_f}\frac{DT_f}{Dt} + \sum_{i=1}^{N_s} \frac{D\mathcal{H}_f(Y_i,T_f)}{DY_i}\frac{DY_i}{Dt} = \\ &= C_p \frac{DT_f}{Dt} + \sum_{i=1}^{N_s} \mathcal{H}_{f,i}(T_f)\frac{DY_i}{Dt} \end{aligned} \tag{1.45}$$

having used equations (1.35) and (1.36) for working out $D\mathcal{H}_f(Y_i,T_f)/DT_f$ and equation (1.34) for working out $D\mathcal{H}_f(Y_i,T_f)/DY_i$. Using the species mass fraction transport equation for DY_i/Dt yields

$$\begin{aligned} \frac{D\mathcal{H}_f(Y_i,T_f)}{Dt} &= C_p \frac{DT_f}{Dt} + \sum_{i=1}^{N_s} \mathcal{H}_{f,i}(T_f)\left[\Gamma_p Y_i - \nabla\cdot\left(\rho_f Y_i \mathbf{V}^c\right)\right. \\ &\qquad \left. -\nabla\cdot\left(\rho_f Y_i \mathbf{V}_i\right) - \nabla\cdot\mathbf{J}_i^{SGS} + \rho_f\omega_i - \Gamma_{p,i}\right] \end{aligned} \tag{1.46}$$

where ω_i the production / destruction rate of species i and an approximated form for the i^{th} species diffusion velocity $\mathbf{V}_i$, with the correction for mass conservation $\mathbf{V}^c$, has been assumed.

The divergence of the diffusive heat flux $\mathbf{q}_{V_i}$, due to single species diffusion velocity (second term in (1.9)), can be written as

$$\nabla \cdot \mathbf{q}_{V_i} = \sum_{i=1}^{N_s} \left\{ \rho_f Y_i (\mathbf{V}_i + \mathbf{V}^c) \cdot \nabla \mathcal{H}_{f,i}(T_f) + \mathcal{H}_{f,i}(T_f) \nabla \cdot \left[\rho_f Y_i (\mathbf{V}_i + \mathbf{V}^c) \right] \right\} \tag{1.47}$$

Considering that

$$\nabla \mathcal{H}_{f,i}(T_f) = \nabla h^0_{f_i}(T_f) + \nabla h_{s_i}(T_f) = C_{p_i} \nabla T_f \tag{1.48}$$

equation (1.47) can be written as:

$$\nabla \cdot \mathbf{q}_{V_i} = \sum_{i=1}^{N_s} \left\{ \rho_f Y_i C_{p_i} (\mathbf{V}_i + \mathbf{V}^c) \cdot \nabla T_f + \mathcal{H}_{f,i}(T_f) \nabla \cdot \left[\rho_f Y_i (\mathbf{V}_i + \mathbf{V}^c) \right] \right\} \tag{1.49}$$

Substituting (1.46), (1.9) and (1.49) into equation (1.20), and taking into account the correction due to the approximation in the species diffusion, it is finally found:

$$\begin{aligned} \rho_f C_p \frac{DT_f}{Dt} &= \frac{Dp}{Dt} + \nabla \cdot \left[k^f \nabla T_f \right] - \nabla \cdot \left[\mathbf{q}_D + \mathbf{q}^{SGS} \right] + \sum_{i=1}^{N_s} \mathcal{H}_{f,i} \nabla \cdot \mathbf{J}_i^{SGS} \\ &+ \Phi_f - Q_{loss} + \rho_f \sum_{i=1}^{N_s} Y_i \left[\mathbf{f}_i - C_{p_i} \nabla T_f \right] \cdot (\mathbf{V}_i + \mathbf{V}^c) - \sum_{i=1}^{N_s} \rho_f \mathcal{H}_{f,i} \omega_i \\ &- \Gamma_p H_p - \Pi_p + Q_{pf} + \sum_{i=1}^{N_s} \mathcal{H}_{f,i} \Gamma_{p,i} \end{aligned} \tag{1.50}$$

It has to be observed that the last term depending on the formation enthalpies changes with temperature is erroneously neglected in many books and numerical codes. The formation enthalpies are usually calculated at a reference temperature, neglecting the dependence of the molecular force field with temperature.

Energy Equation in Terms of T_f and C_v

The aim of this subsection is to write equation (1.50) in terms of temperature and specific heat at constant volume. It is observed that the sum of the two terms containing the material derivative of temperature and pressure in (1.50) can be written as

$$\begin{aligned} \rho_f C_p \frac{DT_f}{Dt} - \frac{Dp}{Dt} &= \rho_f C_p \frac{DT_f}{Dt} - \rho_f R_g \frac{DT_f}{Dt} - \rho_f T_f \frac{DR_g}{Dt} - R_g T_f \frac{D\rho_f}{Dt} \\ &= \rho_f C_v \frac{DT_f}{Dt} - \rho_f T_f \frac{DR_g}{Dt} + p \nabla \cdot \mathbf{u}_f + R_g T_f \Gamma_p \end{aligned} \tag{1.51}$$

after having used the equation of state ($p = \rho_f R_g T_f$), the thermodynamic relation $C_p - R_g = C_v$, and the continuity equation

Substituting (1.51) into (1.50) leads to

$$\begin{aligned}\rho_f C_v \frac{DT_f}{Dt} &= -p\nabla\cdot\mathbf{u}_f + \nabla\cdot\left[k^f\nabla T_f\right] - \nabla\cdot\left[\mathbf{q}_D + \mathbf{q}^{SGS}\right] + \sum_{i=1}^{N_s}\mathcal{H}_{f,i}\nabla\cdot\mathbf{J}_i^{SGS} \\ &+\rho_f T_f\frac{DR_g}{Dt} + \Phi_f - Q_{loss} + \rho_f\sum_{i=1}^{N_s}Y_i\left[\mathbf{f}_i - C_{p_i}\nabla T_f\right]\cdot(\mathbf{V}_i+\mathbf{V}^c) - \sum_{i=1}^{N_s}\rho_f\mathcal{H}_{f,i}\omega_i \\ &-\Gamma_p\left(H_p + R_g T_f\right) - \Pi_p + Q_{pf} + \sum_{i=1}^{N_s}\mathcal{H}_{f,i}\Gamma_{p,i}\end{aligned} \tag{1.52}$$

Using equation (1.44) the following relation is obtained

$$\rho_f T_f\frac{DR_g}{Dt} = \rho_f\mathcal{R}_u T_f\sum_{i=1}^{N_s}\frac{1}{W_i}\frac{DY_i}{Dt}$$

When the expression for the mass fraction material derivative for the i^{th} chemical species is used in the above relation and it is substituted in (1.52) together with equation (1.28), the following form for the energy equation is finally obtained

$$\begin{aligned}\rho_f C_v \frac{DT_f}{Dt} &= -p\nabla\cdot\mathbf{u}_f + \nabla\cdot\left[k^f\nabla T_f\right] - \nabla\cdot\left[\mathbf{q}_D + \mathbf{q}^{SGS}\right] + \sum_{i=1}^{N_s}\mathcal{H}_{f,i}\nabla\cdot\mathbf{J}_i^{SGS} \\ &+\Phi_f - Q_{loss} - \sum_{i=1}^{N_s}\left[\mathbf{f}_i - C_{p_i}\nabla T_f\right]\cdot\left(\rho_f\frac{W_i}{W_{mix}}D_i\nabla X_i + \rho_f Y_i\mathbf{V}^c\right) \\ &+\mathcal{R}_u T_f\sum_{i=1}^{N_s}\frac{1}{W_i}\left[\nabla\cdot\left(\rho_f\frac{W_i}{W_{mix}}D_i\nabla X_i\right)\right. \\ &\left.-\nabla\cdot\left(\rho_f Y_i\mathbf{V}^c + \mathbf{J}_i^{SGS}\right) + \rho_f\omega_i - \Gamma_{p,i}\right] \\ &-\sum_{i=1}^{N_s}\mathcal{H}_{f,i}\left(\rho_f\omega_i - \Gamma_{p,i}\right) - \Gamma_p H_p - \Pi_p + Q_{pf}\end{aligned} \tag{1.53}$$

This form is useful in numerical codes because it contains the material derivative of T_f only. It is implemented in the HeaRT code which has been used for the validation of the models proposed in this work, even though no reactive simulation has been performed. The results that will be presented have been obtained neglecting the Dufour effect, the heat loss, the kinetic energy dissipation during aerodynamic interaction between phases and the dissipation function. The latters are usually small at the resolved scales, when low Mach number conditions are considered.

1.2 Dispersed phase model

The model that will be presented hereafter is based on the *Mesoscopic Formalism* that was first introduced by *Février et al.*[23] and takes advantage from the results of the *Kinetic Theory* for gases [24]. The derivation of the resulting system of equations and a proposed extension to the model are discussed in [15].

The model is made up of the conservation equations for the particle number, for the dispersed phase mass, momentum, enthalpy and functional group mass fractions Y_m respectively.

$$\frac{\partial}{\partial t} n_p + \frac{\partial}{\partial x_j} n_p u_{p,j} = 0 \tag{1.54}$$

$$\frac{\partial}{\partial t} \alpha_p \rho_p + \frac{\partial}{\partial x_j} \alpha_p \rho_p u_{p,j} = \Gamma_p \tag{1.55}$$

$$\frac{\partial}{\partial t} \alpha_p \rho_p u_{p,i} + \frac{\partial}{\partial x_j} \alpha_p \rho_p u_{p,i} u_{p,j} = \frac{\alpha_p \rho_p}{\tau_p} \left(u_{f@p,i} - u_{p,i} \right) + \Gamma_{u,i} \tag{1.56}$$

$$\frac{\partial}{\partial t} \alpha_p \rho_p H_p + \frac{\partial}{\partial x_j} \alpha_p \rho_p H_p u_{p,j} = \Pi_p + \Gamma_h \tag{1.57}$$

$$\frac{\partial}{\partial t} \alpha_p \rho_p Y_m + \frac{\partial}{\partial x_j} \alpha_p \rho_p u_{p,j} Y_m = \Gamma_m \qquad (m = 1..Ng) \tag{1.58}$$

The equations for the evolution of the functional groups are necessary in order to exploit detailed devolatilization models when coal combustion is studied, and to describe the drying phase, during which the moisture adsorbed in the coal structure is released. In the present work a recently developed devolatilization model [25] has been implemented in the HeaRT code. The drying and gasification/oxidation processes are instead modeled after [26]. The following equations hold for the functional groups

$$\sum_{m=1}^{Ng} \Gamma_m = \Gamma_p \tag{1.59}$$

$$\sum_{m=1}^{Ng} Y_m = 1 - Y_{ash} \tag{1.60}$$

meaning that the sum of the masses leaving (or entering) each functional must be equal to the mass leaving the condensed phase. In addition ashes are considered inert within the particle and the sum of ashes and of the transported functional groups mass fractions must return unity.

In the present model the density of the material in the dispersed phase is considered constant and it is assumed to be he same for all the functional groups (and ashes). The heat capacity of the single functional groups are assumed to be constant and evalueted following the procedure described by Merrick[27]. When the assumption of constant heat capacity is taken, it is trivial to obtain the particle temperature from the enthalpy and iterative procedures are not necessary.

The particle relaxation time τ_p appearing in the aerodynamic forces is defined by the following correlation

$$\tau_p = \frac{4\rho_p d_p^2}{3\mu f(Re_p)} \tag{1.61}$$

$$f(Re_p) = 24(1+0.15*Re_p^{0.687}) \qquad Re_p < 1000 \tag{1.62}$$

$$f(Re_p) = 0.44 \qquad Re_p \geq 1000 \tag{1.63}$$

The heat exchange due to convection is modeled as follows

$$\Pi_p = -(6\alpha_p)^{1/3}(n_p\pi)^{2/3}\lambda_f Nu\left(T_p - T_f\right) \tag{1.64}$$

1.3 Subgridscale closure model

In order for the equation system (1.14)-(1.22) to be closed it is necessary to model the terms accounting for SGS effects. A suitable turbulence model must be chosen for this goal. In the present work the Fractal Model (FM) [28, 29, 30, 31] has been selected. FM is a linear algebraic eddy viscosity model which, despite its simplicity, retains some important features in turbulent combustion: *a*) it "switches itself off" in the laminar zones of the flow; *b*) it takes into account the increase in dissipative scale length, due to the high temperature present in the regions where combustion occurs; *c*) it is able to give an estimate of the overall volume occupied by the reactive scales, which are identified with the dissipative scales.

In the present work two main changes have been made to the model:

1. *the model input*: the Reynolds number Re_Δ at the filter cut off length scale Δ is evaluated in a different way with respect to the original model [31];

2. *anisotropic model*: an anisotropic version of the FM, slightly different from the original Anisotropic Fractal Model (AFM) [28] has been developed to keep into account the differences in the three filter scales (Δ_z, Δ_r, Δ_ϑ) in the three directions.

The basics that underlay the fractal modeling of turbulence and a brief description of the FM are here recalled. A description of the changes made that led to the Large eddy Fractal Model (LFM) adopted in this work follows.

It is nowadays well known [32] that fractal theory is able to resemble same statistical and topological features of turbulent flows. Studies [33] have demonstrated that fractal theory is a useful tool in the interpretation of DNS and experimental data. Other studies searched for a correlation between the experimental fractal dimension of a turbulent flame and its propagation velocity [34, 35, 36].

The idea that is at the base of a fractal representation of the turbulent field is the "cascade". The fractal theory relays on the concepts of *fractal generation* and *self similarity*: an element of the fractal called "seed" generates N^C copies of itself, each generating N^C copies on its turn. This generation is here considered a model for the turbulent cascade in the inertial range, where kinetic energy is transfered from larger towards smaller scales, mainly under the effect of the vortex stretching. In Kolmogorov's theory [1] of turbulence, the assumptions are: *a*) within the inertial range, energy flux

occurs locally in frequency, that is between comparable scales; *b*) the energy flux is not depending on the considered frequency (*scale invariance*). This suggests that, when the cascade is to be modelled by a fractal generation, each seed belonging to the scale Δ_1 generates N^C copies at the scale Δ_2, slightly smaller than Δ_1. The self similarity concept, even though it is not strictly the same, seems to be not so distant from Kolmogorov's scale invariance.

This description of the turbulent cascade leads to a representation where the space is filled with eddies belonging to different scales. The iterative generation will stop at the diffusive scale η given by

$$Re_\eta = \frac{u_\eta \eta}{\nu_\eta} = 1 \tag{1.65}$$

where u_η is the velocity and ν_η is the cinematic viscosity corresponding to the dissipative scale.

It has already been pointed out that the fractal model is an algebraic linear eddy viscosity model, which means that it is assumed possible to model the Reynolds stress tensor as

$$\tau_{ij}^{SGS} = \overline{\rho}_f \left(\widetilde{u_i u_j} - \widetilde{u}_i \widetilde{u}_j \right) = -2\mu_t S_{ij} \tag{1.66}$$

where the eddy viscosity μ_t is not function of the strain tensor $\underline{\mathbf{E}}$ but is an algebraic function of the filtered variables. The aim of FM is to find an expression for μ_t.

Let Δ be the filter cut off lengthscale. As in Kolmogorov's theory the assumption is made that no dissipation occurs within the inertial range

$$\frac{u_\Delta^3}{\Delta} = N_\eta \frac{u_\eta^3}{\eta} \tag{1.67}$$

where N_η is the number of dissipative scales produced in the generation process. Given such a representation of the turbulent field, it can be written that

$$\mu_t \propto N_\eta \mu_\Delta \tag{1.68}$$

Following the procedure described in [29], where use is made of the fractal geometry theory, it is finally found

$$\mu_t = \sigma^{SGS} \pi^{-1} \left[\pi^{\frac{1}{3}} Re_\Delta \left(\frac{\nu_\Delta}{\nu_\eta} \right) - 1 \right] \tag{1.69}$$

where $\sigma^{SGS} \in [0.1, 0.6]$ is a calibration parameter and the ratio $\left(\frac{\nu_\Delta}{\nu_\eta}\right)$ has been introduced in order to take into account the effects of viscosity enhancement due to the heat release. The latter occurs in fact at the fine structures, where molecular mixing and chemical reactions take place. It should be noted that, while approaching a wall (or a laminar zone in general) $Re_\Delta \to 0$ and $\mu_t \to 0$ as expected without any need of wall treatment.

Fractal theory also provides [30] the fractal dimension D_3 of the generated fractal

$$D_3 = 3 - \frac{\ln \pi}{\ln\left[\frac{\Delta}{\eta} + \pi - 1\right]} \tag{1.70}$$

that can be regarded as a measure of the ratio between the overall volume Δ^3 and the part of it corresponding to the generated fractal. It is now possible to evaluate the effective reactive volume γ^* as the one occupied by the dissipative scales

$$\gamma^* = \gamma_{N_\eta} \left(\frac{\Delta}{\eta}\right)^{D_3 - 3} \tag{1.71}$$

where the ratio of the number of dissipative scales over the total number of scales γ_{N_η} is empirically fitted by the function

$$\gamma_{N_\eta} = 1 - \frac{0.36\left(\frac{\Delta}{\eta} - 1\right)}{1 + 0.0469\left(\frac{\Delta}{\eta} - 1\right)^{2.7}} \tag{1.72}$$

Following the *Eddy Dissipation Concept* (EDC) [37, 38] the filtered source term $\widetilde{\omega}$ due to chemical reactions is obtained by

$$\widetilde{\omega} = \gamma^* \omega^* \tag{1.73}$$

where ω^* is the source term as evaluated in the chosen reactor model that describes the fine structures. Since no reactive validations have been performed in this work, the possible reactor models, given their large variety, are not described here. Details on the practical implementation of a Perfectly Stirred Reactor may be found in [31].

In the validations of FM [28, 29, 30, 31] performed before the present work, the filtered velocity $\widetilde{\mathbf{u}}_f$ was used as the characteristic velocity u_Δ of the filter cut off length-scale in the evaluation of Re_Δ.

During the validation of the present work, when the Sommerfeld and Qiu [39] experiment has been simulated by means of the HeaRT code, two different necessity raised that pushed the author to apply the changes mentioned above: first, the performance of FM for given conditions were not satisfactory, leading to the impossibility to correctly reproduce the field topology, which is strongly influenced by it; second, since the HeaRT code solves the flow equations on a structured cylindrical grid, it happens to deal with grid cells that have very high aspect ratios. In the given conditions the calculation made by means of the HeaRT code showed the tendency to diverge.

In the present model the Reynolds number Re_Δ, which is the parameter that rules the fractal generation, is evaluated using an estimate of the amplitude of the mode of lengthscale 2Δ of the signal $\widetilde{\rho_f u_f}$, that will be addressed from now on as $(\rho u)_\Delta$, instead of $\widetilde{\rho}_f \widetilde{u}_f$. Note that the choice to use (ρu) fluctuations instead of u may also represent a link for acoustic-turbulence interactions to be modelled. In order to obtain the estimate for $(\rho u)_\Delta$ a stencil of 5 or 4 points is used, depending on whether the variable (ρu) is collocated in the point where the estimate is to be calculated or not, respectively. Consider the expansion

$$\widetilde{\rho u} = \sum_{n=1}^{N_x} A_n \sin\left(\frac{\pi x}{\Delta_x n} + \phi_n\right) + c_n \qquad (1.74)$$
$$N_x = \frac{L_x}{\Delta_x}$$

where L_x is the domain dimension in the x direction. Equation (1.74) is the part of the Fourier series that can be sampled on a uniform grid with cells width equal to Δ_x. For $n = 1$ the highest frequency mode is obtained. In order to properly use the FM one should be in the conditions to provide it with A_1. The latter can be obtained by applying some kind of high pass filter to the $\widetilde{\rho_f u_f}$ signal. This filter must be compact and fast. This is the first attempt to use such a procedure in conjunction with the FM and the easiest solution has thus been used obtaining satisfactory results. More refined filters could be used in the future thus improving the model performance.

Due to the staggered grid used by the gas solver (see section 2.1) two discrete filters have been used. With reference to Figure 1.1, when $(\rho u)_\Delta$ is to be obtained at the x_i point and the $\widetilde{\rho_f u}_f$ variable is collocated at the cell center (Figure 1.1 a) a 5 point stencil filter is used. This is the case when $\widetilde{\rho_f u}_{f,x}$ component is being filtered in the y direction. Differently, when the variable to be filtered is collocated at the grid nodes (Figure 1.1 b), a 4 point stencil is used. A linear combination of the $\widetilde{\rho_f u}_f$ values on

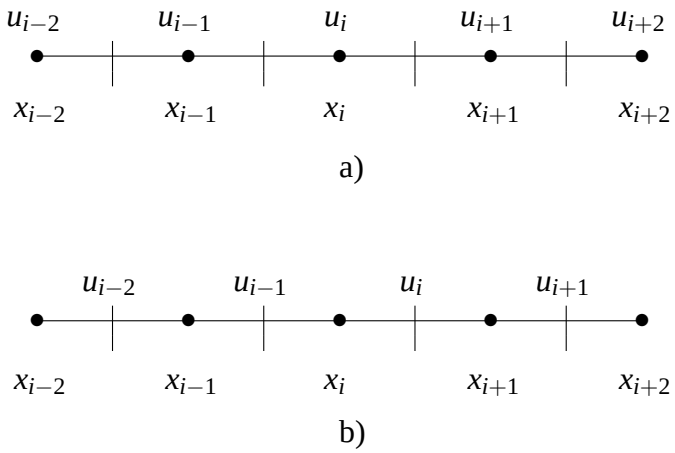

Figure 1.1: Filter stencil for $(\rho u)_\Delta$ estimation

the filter stencil around x_i is used. For a 4 point stencil it is

$$\left(\rho_f u_{f,j}\right)^i_{\Delta_x} = \sum_{p=-2}^{1} \chi_p \left(\widetilde{\rho_f u}_{f,j}\right)^{i+p} \tag{1.75}$$

while for a 5 point stencil

$$\left(\rho_f u_{f,j}\right)^i_{\Delta_x} = \sum_{p=-2}^{2} \chi_p \left(\widetilde{\rho_f u}_{f,j}\right)^{i+p} \tag{1.76}$$

is used, where i is the cell index in the filter direction, j is the direction of the $\rho_f u_f$ considered component and p is the point index on the filter stencil. The coefficients χ_p must satisfy the condition

$$\sum_p \chi_p = 0 \tag{1.77}$$

in order to return no fluctuations when a constant signal is filtered. When the expansion (1.74) is substituted into (1.75) or (1.76) the following expression is obtained

$$\left(\rho_f u_{f,j}\right)^i_{\Delta_x} = \sum_{n=1}^{N_x} \sum_p \chi_p A_n \left[\sin\left(\frac{\pi x}{\Delta_x n} + \phi_n\right) + c_n\right] \tag{1.78}$$

When a 4 point stencil and uniform grid are considered, the substitution of $\chi = \frac{1}{4}(-1,1,-1,1)$ in (1.78) and some algebra yields

$$\left(\rho_f u_{f,j}\right)^i_{\Delta_x} = A_1 \sin\phi_1 + \sum_{n=2}^{N_x} A_n \left[\cos\frac{\pi}{n} \cos\left(\frac{3}{2}\frac{\pi}{n} + \phi_n\right) \sin\frac{\pi}{n}\right] \tag{1.79}$$

It can be seen in equation (1.79) that the amplitude of the first mode ($n = 1$) will be dumped by the sin function of its phase ϕ_1; the mode for $n = 2$ will be cancelled while the other modes will be dumped because of the multiplication by 3 sin/cos functions. Thus, when $\phi_1 = \pm\frac{\pi}{2}$ equation (1.79) returns a value very close to A_1, while for $\phi_1 = k\pi$, k being an integer, equation (1.79) returns a dumped value of the amplitude of the lower frequency modes.

A similar result is obtained by selecting $\chi = \frac{1}{16}(1,-4,6,-4,1)$ for the 5 point stencil. In this case no cancellation of the mode for $n = 2$ is obtained but higher dumping for the modes for greater n is granted with respect to the 4 point stencil case.

For non uniform grid, if the grid stretching factor $\frac{\Delta x_{i+1}}{\Delta x_i} < 1.1$ the error introduced in the (1.79) is small and well within the model uncertainty and no additional corrections are taken.

Assuming that all the three cut off lengthscales are within the inertial range, under the hypothesis of homogeneous isotropic turbulence, it is possible to rescale the three filtered values obtained for each component by filtering in the three directions, on a unique lengthscale. In the present work the intermediate filter scale has been chosen, with the exception of walls treatment. Thus, if ($\Delta x < \Delta y < \Delta z$), by applying the conservation of the kinetic energy on the turbulent cascade it is possible to write

$$\left(\rho_f u_{f,j}\right)_{x,\Delta_y} = \left(\frac{\Delta_y}{\Delta_x}\right)^{\frac{1}{3}} \left(\rho_f u_{f,j}\right)_{x,\Delta_x} \qquad \left(\rho_f u_{f,j}\right)_{z,\Delta_y} = \left(\frac{\Delta_y}{\Delta_z}\right)^{\frac{1}{3}} \left(\rho_f u_{f,j}\right)_{z,\Delta_z} \quad (1.80)$$

which means that for the j^{th} component of the $\left(\rho_f \mathbf{u}_f\right)_\Delta$ vector three possible values have been obtained, depending on the direction where the high pass filter has been applied. The average of these values is taken in order to limit the error due to the signal phase ϕ_1 uncertainty

$$\left(\rho_f u_{f,j}\right)_\Delta = \frac{1}{3}\left[\left(\rho_f u_{f,j}\right)_{x,\Delta_y} + \left(\rho_f u_{f,j}\right)_{y,\Delta_y} + \left(\rho_f u_{f,j}\right)_{z,\Delta_y}\right] \quad (1.81)$$

Another error whose effects are limited with this procedure is the extrapolation from or to lengthscales that are outside the inertial range. This may sometimes occur locally in the domain.

A slightly different treatment is used in the wall boundary condition, since in that region the isotropic hypothesis is no longer valid. The filter scale on which fluctuations are rescaled there, is no longer the intermediate grid step in the three directions but the boundary cell width in the direction normal to the wall.

After the three components are evaluated, the module of $\left(\rho_f \mathbf{u}_f\right)_\Delta$ is simply obtained as

$$\left(\rho_f u_f\right)_\Delta = \left[\left(\rho_f u_{f,x}\right)_\Delta^2 + \left(\rho_f u_{f,y}\right)_\Delta^2 + \left(\rho_f u_{f,z}\right)_\Delta^2\right]^{\frac{1}{2}} \tag{1.82}$$

The Reynolds number at the cut off lengthscale Re_Δ that is used in (1.69) is then obtained as

$$Re_\Delta = \frac{\left(\rho_f u_f\right)_\Delta \Delta}{\mu_\Delta} \tag{1.83}$$

where Δ is the lengthscale over which the fluctuations have been rescaled.

A second problem that occurred in the simulation of Sommerfeld and Qiu test case [39] is due to the fact that the HeaRT code, which has been used for the validation of the models, solves the flow equations on a structured cylindrical grid. This constraint brought to have a computational grid presenting cells with aspect ratios, defined as the ratio between cell sizes on different directions, 10 or higher. Under these conditions the numerical scheme implemented in the HeaRT code (see section 2.1) showed a tendency to diverge. In order to perform the simulation the SGS model has been modified in order to add dissipation in the direction where the filter scale is greater than the one on which the fluctuations have been actually measured. The SGS model, as given in equation (1.66), has thus been modified as

$$\tau_{ij}^{SGS} = -\left(\mu_{t,j}\frac{\partial \widetilde{u}_i}{\partial x_j} + \mu_{t,i}\frac{\partial \widetilde{u}_j}{\partial x_i}\right) + \frac{2}{3}\mu_{t,k}\frac{\partial \widetilde{u}_k}{\partial k}\delta_{ij} \tag{1.84}$$

and equations (1.69) and (1.83) as

$$\mu_{t,j} = \sigma^{SGS}\pi^{-1}\left[\pi^{\frac{1}{3}} Re_{\Delta_j}\left(\frac{\nu_\Delta}{\nu_\eta}\right) - 1\right] \tag{1.85}$$

$$Re_{\Delta_j} = \frac{\left(\rho_f u_f\right)_\Delta \Delta_j}{\mu_\Delta} \tag{1.86}$$

It should be pointed out here that this anisotropic formulation has not been thought for modelling reasons, meaning that it does not take into account any anisotropy in the distribution of the turbulent structures.

Finally, the calibration constant σ^{SGS} changes its meaning with respect to the previous formulation of FM [29, 30]. While it is there supposed to account for the uncertainties on the cut off filtering, and can thus be tuned by a Germano procedure [40], in the present version of FM this uncertainties have been addressed, and the natural value

of σ^{SGS} is therefore 1. Higher values could be necessary to stabilize the numerical scheme, but they should be regarded as artificial viscosity rather than a model for SGS effects.

As to the models for the other SGS contributions ($J_{s,j}^{SGS}$ and q_j^{SGS}) they will be modelled in analogy with the Reynolds stress term

$$J_{sj}^{SGS} = -\rho_f \frac{Y_s}{X_s} D_{t,j}^s \frac{\partial X_s}{\partial x_j} \tag{1.87}$$

$$q_j^{SGS} = -k_{t,j} \frac{\partial T_f}{\partial x_j} \tag{1.88}$$

where

$$D_{t,j}^s = \left(1 + \frac{\mu_{t,j}}{\mu}\right) D_s$$

$$k_{t,j} = \left(1 + \frac{\mu_{t,j}}{\mu}\right) k$$

Chapter 2

Numerical approach

2.1 Numerical scheme for the gas phase equations

The system of equations (1.14)-(1.22) that govern the evolution of the gas phase filtered variables is numerically solved by means of the HeaRT code developed in ENEA. The gas phase solver is based on a centered II order finite difference scheme on a staggered cylindrical non uniform grid. The idea is to define a different grid for each velocity component as shown in two dimensions in Figure 2.1. Each velocity component is staggered in space by half grid width with respect to the scalar variables, ρ, p, T and Y_i. Consider (Figure 2.2) an hexaedral cell, whose faces lay on a coordinate plane. The velocity vectorial component in the j^{th} direction

$$\mathbf{u}_{f,j} = u_{f,j}\hat{\mathbf{n}}_j = u_{f,j}\hat{\mathbf{i}}_j \tag{2.1}$$

normal to the cell face is collocated at the face center. In (2.1) $\hat{\mathbf{n}}_j$ is the versor normal to the cell surface in the outcoming direction while $\hat{\mathbf{i}}_j$ is the j^{th} coordinate direction versor. Finally, scalar variables are collocated at the cell center.

This discretization technique leads to a higher precision and to a more robust discretization of the time-dependent continuity equation, for which no interpolations are performed.

In order to simplify the notation let the following difference (δ_{x_k}) and interpolation ($\overline{u}^{x_k}$) operators be defined as

$$\delta_x(u_{i,j}) = \frac{u_{i+1/2,j} - u_{i-1/2,j}}{\Delta x}, \;\; \delta_y(u_{i,j}) = \frac{u_{i,j+1/2} - u_{i,j-1/2}}{\Delta y}. \tag{2.2}$$

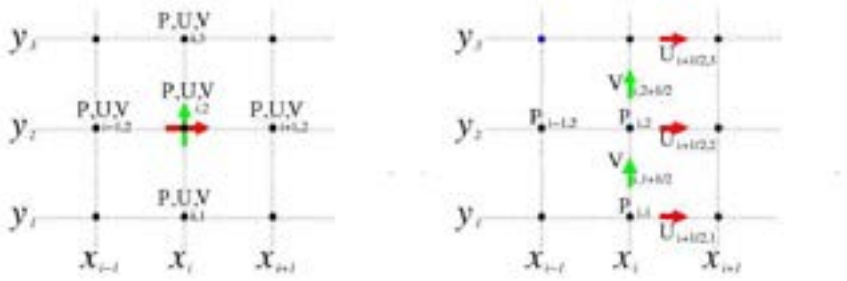

Figure 2.1: Left) Collocated grid; Right) Staggered grid.

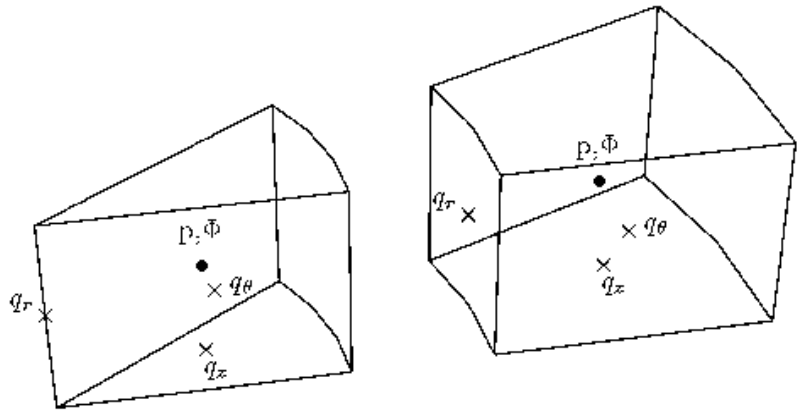

Figure 2.2: Example of a cylindrical staggered grid.

and

$$\overline{u}^{x}_{i,j} = \frac{u_{i+1/2,j} + u_{i-1/2,j}}{2}\,, \quad \overline{u}^{y}_{i,j} = \frac{u_{i,j+1/2} + u_{i,j-1/2}}{2}\,, \tag{2.3}$$

The difference and interpolation operators produce a second order accurate estimate of the derivatives of the variables and of the variables themselves at the center of the operator support. When the equations are generalized on nonuniform grids, the interpolation and differencing operators are modified as

$$\overline{u}^{x}_{i+1/2} = c_i u_{i+1} + (1-c_i)u_i\,, \quad \delta_x(u)_{i+1/2} = \frac{u_{i+1} - u_i}{x_{i+1} - x_i}\,, \tag{2.4}$$

where

$$c_i = \begin{cases} \frac{1}{2} & \text{for velocity component} \\ \frac{x_i - x_{i-1}}{x_{i+1} - x_{i-1}} & \text{for scalar variables} \end{cases} \tag{2.5}$$

and x_i is the coordinate in the x direction where the velocity component in the same direction, for the i^{th} grid cell, is collocated.

When this staggered shifting is properly taken into account, this notation can be used to write the discrete equations in an index-free form, with the convention that any two quantities that are added or multiplied must be at the same location on the space grid. The expression of the discretized governing equations will be simplified by introducing the intermediate variable g_i for the momentum per unit volume, which is defined according to:

$$g_i = \overline{\rho}_f^{x_i} u_{f,i}\,, \quad u_{f,i} = g_i / \overline{\rho}_f^{x_i}\,. \tag{2.6}$$

With this notation the governing set of equations discretized on a cylindrical grid (with r the radial direction, x the axial direction and ϑ the azimuthal direction) takes the following form

continuity:

$$\delta_t(\rho) + \delta_z(g_z) + \frac{1}{r}\delta_r(r g_r) + \frac{1}{r}\delta_\vartheta(g_\vartheta) = -\Gamma_p$$

momentum:

$$\delta_t(g_z) = \delta_z(f_{zz}) + \frac{1}{r}\delta_r(r f_{zr}) + \frac{1}{r}\delta_\vartheta(f_{z\vartheta}) - \Gamma_p u_{p,z} + \alpha_p \rho_p \left(\frac{u_{p,z} - u_{f,z}}{\tau_p}\right)$$

$$\delta_t(g_r) = \delta_z(f_{rz}) + \frac{1}{r}\delta_r(r f_{rr}) + \frac{1}{r}\delta_\vartheta(f_{r\vartheta}) - \frac{\overline{f_{\vartheta\vartheta}}^r}{r} - \Gamma_p u_{p,r} + \alpha_p \rho_p \left(\frac{u_{p,r} - u_{f,r}}{\tau_p}\right)$$

$$\delta_t(g_\vartheta) = \delta_z(f_{\vartheta z}) + \frac{1}{r}\delta_r(r f_{\vartheta r}) + \frac{1}{r}\delta_\vartheta(f_{\vartheta\vartheta}) + \frac{\overline{f_{\vartheta r}}^r}{r} - \Gamma_p u_{p,\vartheta} + \alpha_p \rho_p \left(\frac{u_{p,\vartheta} - u_{f,\vartheta}}{\tau_p}\right)$$

$$f_{zz} = 2\mu[\delta_z(\overline{u_{f,z}}^t) - \frac{1}{3}\Theta] - \overline{g_z}^z \overline{u_{f,z}}^z - p$$

$$f_{rr} = 2\mu[\delta_r(u_{f,r}) - \frac{1}{3}\Theta] - \overline{g_r}^r \overline{u_{f,r}}^r - p$$

$$f_{\vartheta\vartheta} = 2\mu[\frac{1}{r}\delta_\vartheta(u_{f,\vartheta}) + \frac{\overline{u}^r_{f,r}}{r} - \frac{1}{3}\Theta] - \overline{g_\vartheta}^\vartheta \overline{u_{f,\vartheta}}^\vartheta - p$$

$$f_{zr} = \overline{\overline{\mu}^z}^r [\delta_z(u_{f,r}) + \delta_r(u_{f,z})] - \overline{g_r}^z \overline{u_{f,z}}^r$$

$$f_{rz} = \overline{\overline{\mu}^r}^z [\delta_z(u_{f,r}) + \delta_r(u_{f,z})] - \overline{g_z}^r \overline{u_{f,r}}^z$$

$$f_{r\vartheta} = \overline{\overline{\mu}^r}^\vartheta [\delta_r(u_{f,\vartheta}) + \frac{1}{r}\delta_\vartheta(u_{f,r}) - \frac{\overline{u_{f,\vartheta}}^r}{r}] - \overline{g_\vartheta}^r \overline{u_{f,r}}^\vartheta$$

$$f_{\vartheta r} = \overline{\overline{\mu}^r}^\vartheta [\delta_r(u_{f,\vartheta}) + \frac{1}{r}\delta_\vartheta(u_{f,r}) - \frac{\overline{u_{f,\vartheta}}^r}{r}] - \overline{g_r}^\vartheta \overline{u_{f,\vartheta}}^r$$

$$f_{z\vartheta} = \overline{\overline{\mu}^z}^\vartheta [\delta_z(u_{f,\vartheta}) + \frac{1}{r}\delta_\vartheta(u_{f,z})] - \overline{g_\vartheta}^z \overline{u_{f,z}}^\vartheta$$

$$f_{\vartheta z} = \overline{\overline{\mu}^z}^\vartheta [\delta_z(u_{f,\vartheta}) + \frac{1}{r}\delta_\vartheta(u_{f,z})] - \overline{g_z}^\vartheta \overline{u_{f,\vartheta}}^z$$

generic scalar transport:

$$\delta_t(\rho\phi) = \delta_z(q_z) + \frac{1}{r}\delta_r(rq_r) + \frac{1}{r}\delta_\vartheta(q_\vartheta) + \rho w$$

$$q_z = \overline{\rho\alpha}^z \delta_z(\phi) - g_z \overline{\phi}^z$$

$$q_r = \overline{\rho\alpha}^r \delta_r(\phi) - g_r \overline{\phi}^r$$

$$q_\vartheta = \overline{\rho\alpha}^\vartheta \delta_\vartheta(\phi) - g_\vartheta \overline{\phi}^\vartheta$$

where w is the generic source term for the transported scalar.

2.1.1 Treatment of variables on the axis

All the quantities are staggered with respect to the centerline in the radial direction (i.e. they lie at $\Delta/2$ from the axis), except $u_{f,r}$, that is collocated on the axis. The values of $u_{f,r}$ at the centerline are obtained averaging the values of $u_{f,r}$ near the axis as described below:

$$u_{f,r}(r=0,\vartheta) = \frac{1}{2}\left[u_{f,r}(\Delta r,\vartheta) + u_{f,r}(\Delta r,\vartheta+\pi)\right]. \tag{2.7}$$

The angular distribution of $u_{f,r}$ on the point near the axis of symmetry does not ensure a single value of $u_{f,r}$ on the axis.

2.1.2 Metric correction

When discrete volumes are considered, instead of infinitesimal ones, a correction for the derivatives in azimuthal direction is needed, that is

$$\delta_\vartheta(u_{i,j,k}) = \frac{u_{i,j,k+\frac{1}{2}} - u_{i,j,k-\frac{1}{2}}}{2\sin\frac{\Delta\vartheta}{2}} \tag{2.8}$$

In addition, when the azimuthal component of the velocity is interpolated at the cell center the following correction is used

$$\overline{u}^\vartheta_{f,\vartheta\|i,j,k} = \frac{u_{f,\vartheta\|i,j,k+\frac{1}{2}} + u_{f,\vartheta\|i,j,k-\frac{1}{2}}}{2}\cos\frac{\Delta\vartheta}{2} \tag{2.9}$$

2.2 Dispersed phase

The equation system (1.54-1.58) will be numerically solved on the same computational grid used for the gas phase scalar variables, by means of a finite volume technique (or Godunov's method). Let the vector of the average variables $\bar{\mathbf{U}}$ be defined by averaging the variable vector $\mathbf{U}$ over the control volume

$$\bar{\mathbf{U}}_{ijk} = \frac{1}{r\Delta z\Delta r\Delta\vartheta}\int_{\Delta\mathcal{V}} r\mathbf{U}d\mathcal{V} \tag{2.10}$$

and the average source term $\check{\mathbf{H}}$

$$\check{\mathbf{H}}_{ijk} = \frac{1}{r\Delta z\Delta r\Delta\vartheta}\int_{\Delta\mathcal{V}} \mathbf{H}d\mathcal{V} \tag{2.11}$$

be approximated by the value of the function $\left(\frac{\mathbf{H}}{r}\right)$ at the cell center. When this definitions are substituted into the equations (1.54-1.58) under integral form and the surface fluxes are approximated with first order accurate values, the equation system can be written as

$$\begin{aligned}\frac{\partial\bar{\mathbf{U}}_{ijk}}{\partial t} = -\frac{1}{r\Delta z\Delta r\Delta\vartheta}\Big\{ & \left[(r\mathbf{F}_z - r\mathbf{G}_z)_{i+\frac{1}{2}} - (r\mathbf{F}_z - r\mathbf{G}_z)_{i-\frac{1}{2}}\right]\Delta r\Delta\vartheta \\ & + \left[(r\mathbf{F}_r - r\mathbf{G}_r)_{j+\frac{1}{2}} - (r\mathbf{F}_r - r\mathbf{G}_r)_{j-\frac{1}{2}}\right]\Delta z\Delta\vartheta \\ & + \left[(\mathbf{F}_\vartheta - \mathbf{G}_\vartheta)_{k+\frac{1}{2}} - (\mathbf{F}_\vartheta - \mathbf{G}_\vartheta)_{k-\frac{1}{2}}\right]\Delta r\Delta z \Big\} \\ & + \check{\mathbf{H}}_{ijk} + O(\Delta^2)\end{aligned} \tag{2.12}$$

In order for the method to be well defined it is necessary to select:

1. a reconstruction algorithm that enables to find the flux values at the cell boundaries;

2. a time evolution algorithm.

The time evolution scheme is the same for both phases and will be described in section (2.3).

2.2.1 Reconstruction method

The reconstruction algorithm will be here presented for a 1-D scheme, for reasons of notation simplicity, without any lost in generality. As already mentioned, a linear reconstruction around the averaged values of the conserved variables is taken. The averaged values are considered to be equal to the local value at the cell center as shown in Figure 2.3. In the case where the uncorrelated motion is neglected it can be shown [41]

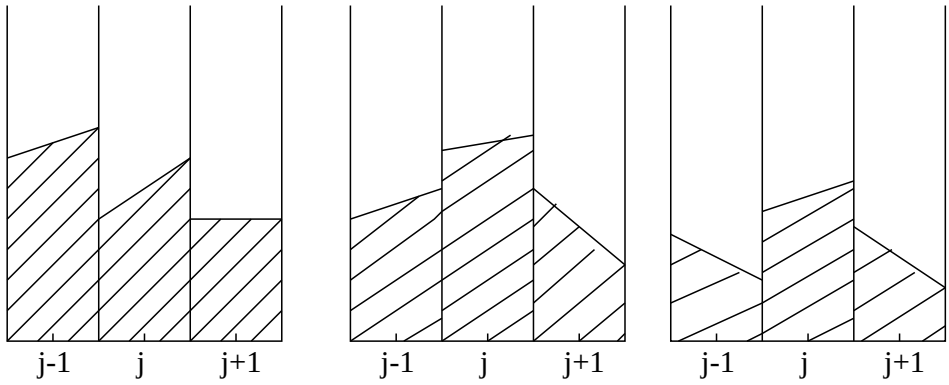

Figure 2.3: Linear reconstruction of the variables within the cell

that the system of equations for the dispersed phase has three coincident eigenvalues equal to the dispersed phase velocity. An upwind scheme has thus been selected for the reconstruction phase. The numerical scheme should not produce oscillation in the presence of dispersed phase fronts, *i.e.* the cells that divide regions where particles are present from those where particle are absent. If the numerical scheme allowed the solution for particle number density n_p or volumetric fraction α_p to present oscillations in this cells, it could be possible for this variables to become negative. This is unphysical and would lead the calculation to diverge. The reconstruction phase for the dispersed phase mass flux is thus very important in order to prevent spurious oscillation to occur in the front regions.

For the i^{th} direction, the reconstruction phase of the fluxes at the point x_j, where the interface between cells j and $j+1$ is collocated, can be finally summarized as

1. evaluate the slopes of the mass flux variable $(\alpha_p \rho_p u_{p,i})$ normal to the considered interface, for both cell j and $j+1$;

2. evaluate the mass flux for both the left $(\alpha_p \rho_p u_{p,i})^L$ and the right side $(\alpha_p \rho_p u_{p,i})^R$ of the interface (see Figure 2.4);

3. solve the Riemann problem at the interface;

4. depending on the solution of the Riemann problem evaluate the slope for all the other variables in the cell placed upwind with respect to the considered interface (see Figure 2.5) ;

5. from the average value in the upwind cell reconstruct the variable value at the interface.

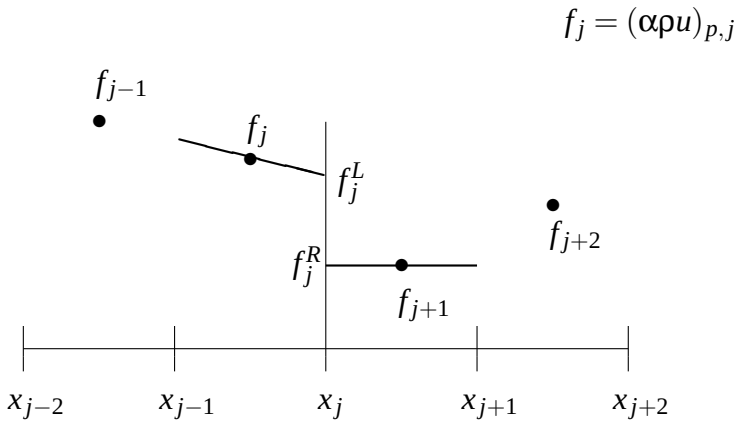

Figure 2.4: Mass flux reconstruction at the interface

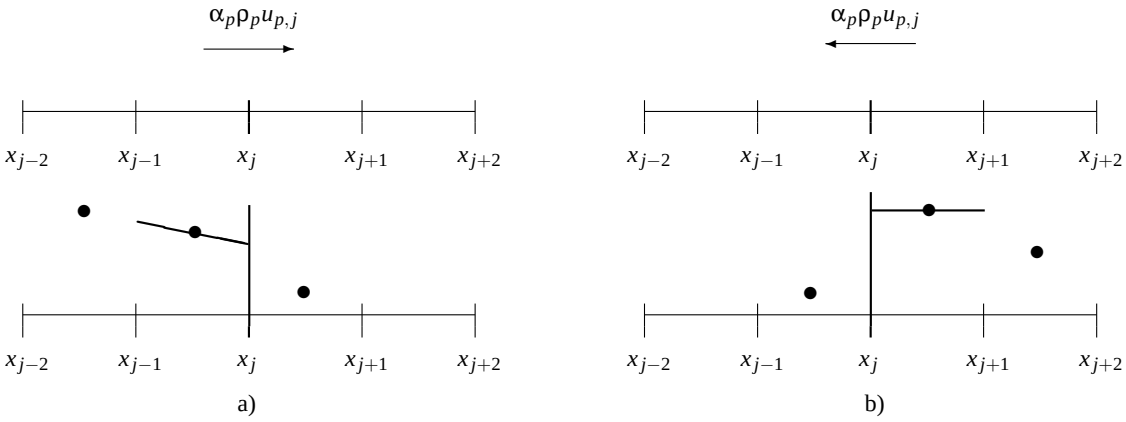

Figure 2.5: Upwind reconstruction at the interface for the generic variable

For both points 1 and 4 the evaluation of the variable slope Sl_j in the j^{th} cell is made, accordingly with the ENO (Essentially Non-Oscillatory) scheme theory, by applying a limiter in order to prevent oscillations and keep the calculation stable. The

minmod limiter has been adopted here. In the calculation of the slope of the mass flux component normal to the considered interface a modified version (Algorithm 2.2.1) of the classic *minmod* limiter has been used, while for the other variables the generic algorithm (Algorithm 2.2.2) is adopted. Examples of the *minmod* limiter action are shown in Figures (2.4) and (2.5).

Algorithm 2.2.1 Modified *Minmod* Algorithm for mass flux variables

if $f_j = 0$ **then**
  $Sl_j = 0$
else
  evaluate $Sl_R = 2\frac{f_{j+1}-f_j}{x_{j+1}-x_{j-1}}$
  evaluate $Sl_L = 2\frac{f_j-f_{j-1}}{x_j-x_{j-2}}$
  if $Sl_R \cdot Sl_L \leq 0$ **then**
    $Sl_j = 0$
  else if $|Sl_R| < |Sl_L|$ **then**
    $Sl_j = Sl_R$
  else
    $Sl_j = Sl_L$
  end if
  $\Delta f = \frac{1}{4}\left(x_{j+1} - x_{j-1}\right) Sl_j$
  if $f_j^2 - \Delta f^2 < 0$ **then**
    $Sl_j = 0$
  end if
end if

Due to the piecewise reconstruction of the solution, discontinuities will arise at the cell boundaries. It is thus necessary to evaluate the associated Riemann problem, in order to evaluate the fluxes $\underline{\mathbf{F}}$ and $\underline{\mathbf{G}}$.

Riemann solver for the correlated motion

After the reconstruction phase, two different values for the mass flux ($\alpha_p \rho_p u_{p,i}$) at the generic interface in the i^{th} direction will be available (see Figure 2.4). As already said it is very important to well predict the solution of this Riemann problem to keep the numerical algorithm stable during the calculation. Besides the value of the mass flux that will be used in the evolution step f_j, the Riemann solver must return the upwind

Algorithm 2.2.2 Generic *Minmod* Algorithm

evaluate $Sl_R = 2\frac{f_{j+1}-f_j}{x_{j+1}-x_{j-1}}$
evaluate $Sl_L = 2\frac{f_j-f_{j-1}}{x_j-x_{j-2}}$
if $Sl_R \cdot Sl_L \leq 0$ **then**
  $Sl_j = 0$
else if $|Sl_R| < |Sl_L|$ **then**
  $Sl_j = Sl_R$
else
  $Sl_j = Sl_L$
end if

direction dir that will be used in the reconstruction of the other variables. The Riemann solver adopted in this work is presented in Algorithm 2.2.3. It is worth to note here that it returns value equal to zero for the mass flux when the values reconstructed from both sides of the interface are exiting from the interface itself. On the contrary, when both values are entering the interface, their sum is taken as a solution. When none of these two cases occurs, the upwind flux is selected as a solution of the Riemann problem.

Algorithm 2.2.3 Riemann solver for the correlated motion

$dir \leftarrow$left
$f_j = 0$
if $f_j^L > 0$ **then**
  $f_j = f_j^L$
  if $f_j^L \cdot f_j^R < 0$ **then**
    $f_j = f_j^L + f_j^R$
  end if
else if $f_j^R < 0$ **then**
  $f_j = f_j^R$
end if
if $f_j < 0$ **then**
  $dir \leftarrow$right
end if

Particular attention should be paid to the condition when both fluxes are entering the interface. This is a shock since both the characteristics of the same family are cross-

ing each other at the interface. The solution adopted here, has its physical justification in the assumption of dilute conditions. Since the particles coming from the two control volumes divided by the interface, and crossing there one another's trajectory, will not collide, the net mass flux will actually be the difference in module (their sum in fact) of the two reconstructed values. Nevertheless this kind of solution, which conserves the effective mass of the system, imply a dissipation of kinetic energy. The Riemann solver is thus non-conservative and only when the uncorrelated motion will be taken into account it will be possible to address this kind of problem.

2.3 Time evolution scheme

In the time evolution step, a numerical scheme is used in order to advance the solution from the time t^n to the time t^{n+1}. In the present work a one-step explicit Runge-Kutta III order accurate scheme has been used. A generic Runge-Kutta scheme can be expressed by

$$\begin{cases} u^{n+1} = u^n + h\sum_{i=1}^{s} b_i k_i^n & n = 0,..,N-1 \\ u^0 = u(t_0) \end{cases} \tag{2.13}$$

where

$h = t^{n+1} - t^n$

$k_i^n = F\left(t_n + c_i h, \quad u^n + h\sum_{j=1}^{i-1} a_{ij} k_j^n\right) \qquad i = 1,..,s$

$c_1 = 0$

$\sum_{j=1}^{0} \cdots = 0$

a_{ij}, c_i, b_i:=coefficients to be determined;

s:=substeps in the Runge-Kutta scheme.

In order to obtain a III order accurate scheme $s = 3$ must be chosen. In the scheme here adopted [42] the coefficients are set to

$c_2 = c_3 = 0$

$b_1 = b_2 = \frac{1}{6} \quad b_3 = \frac{2}{3}$

$a_{21} = 1 \quad a_{31} = a_{32} = \frac{1}{4}.$

In order to ensure the calculation stability two conditions must be respected: the condition on the *Courant-Friedricks-Lewy* (CFL) condition and the condition on the *Von Neumann* number VNN for the stability of transport-diffusion systems. The CFL (or *Courant*) number is defined as

$$CFL = \lambda_j^{MAX} \frac{\Delta t}{\Delta x_j} \tag{2.14}$$

where λ_j^{MAX} is the maximum local eigenvalue in the j^{th} direction. The physical meaning of this condition can be explained with reference to Figure 2.6. $CFL = 1$ implies that Δt is the time by which the signal entering the control volume crosses it reaching the opposite interface. Δt is therefore the time by which the flux estimate should be updated, unless the initial estimate already takes into account the outcoming flux variation.

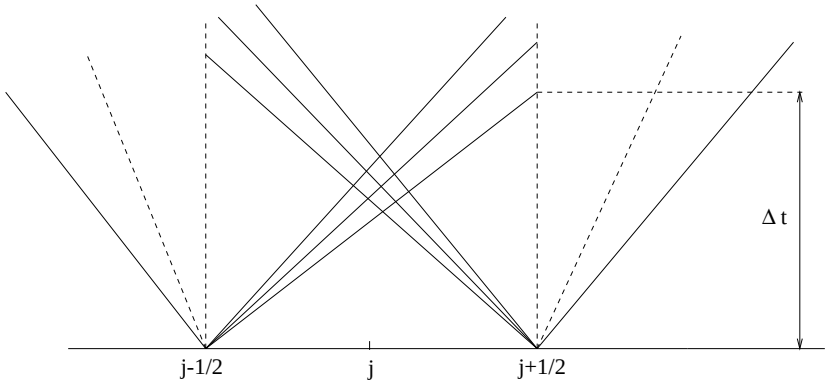

Figure 2.6: Physical interpretation of the CFL condition

The non-linear stability of this scheme, in conjunction with a ENO reconstruction is reported in [42] to be given by the condition $CFL < 1$. Nevertheless, the application of III order R-K schemes, in conjunction with the staggered discretization described in section (2.1), to compressible flow LES is reported in [43] to be performed using $CFL = 0.1$ in order to limit the effects of the truncation error. For conventional applications, the module of the system maximum eigenvalue will be much greater for the gas phase (depending on the speed of sound) than for the dispersed phase. The satisfaction of the CFL condition will thus be evaluated for the gas phase only.

The condition on the VNN defined as

$$VNN = \nu \frac{\Delta t}{(\Delta x)^2} \tag{2.15}$$

for a Forward-Time-Centered-Space (FTCS) it is reported to be $VNN < 0.5$ proven that a condition for the cell Reynolds number Re_Δ is satisfied. The complete analysis of the FTCS scheme stability is reported in [44].

Chapter 3

Model validation

In the present chapter the activity on the validation of the two-phase flow model will be presented and the results associated to the proposed numerical approach will be shown.

It must be pointed out here that the equation system (1.54-1.58) is ready for reactive test cases once that a mass exchange model between phases is provided, even though a non reacting test case is here presented. As will be cleared in the following sections the accuracy granted by the present model justifies the adoption of a LES technique. In fact, the model for the dispersed phase that has been tested up to this point is very similar to those adopted in other codes (CERFACS AVBP) with different numerical strategies. The main difference, under a modelling point of view, is that a SGS model is used there for the dispersed phase which here has been considered unjustified. It can be shown that the Stokes number based on SGS turbulent characteristic timescale approches unity for very small particles (few microns). The results from the validation performed seem to confirm the assumption on SGS modelling made in this work to be correct.

The Sommerfeld and Qiu test case [39] has been selected as a test case since it presents a sufficiently detailed database to assess that:

1. the numerical implementation for the transport model is robust and reliable;

2. the assumption that no SGS modelling is needed for particle relaxation time based on turbulence characteristic time $\tau_p^t >> 1$ is verified;

3.1 Sommerfeld and Qiu experiment

In the Sommerfeld and Qiu [39, 45] experiment a particle laden flow is obtained by injecting small ($20 - 80$ μm) glass particles in a confined swirled flow. In Figure 3.1 the experimental set-up can be seen. The injection system composes of a cylindrical duct and of an annular duct coaxial to the first one. Air and particles flow through the cylindrical duct to the test chamber while from the annular duct a swirled air flow is introduced in the test section. The swirl number is 0.47. At the end of the test chamber an expansion chamber is present.

Measures of both air and particle velocities are taken on 8 different radial planes, from 3 mm from the injection plane down to 315 mm from it. Data for both phases mean and RMS velocities and their radial distributions are taken. Different classes of particle size are considered.

There are different reasons that suggested the choice of this experiment for the validation of the models and numerics developed in this work: *a*) there is a large variety of numerical publications based on it; *b*) the extensive database of measures suits well to the validation objectives outlined at the beginning of this chapter; *c*) similar flow configurations can be found in pulverized coal burners and the particle size is within

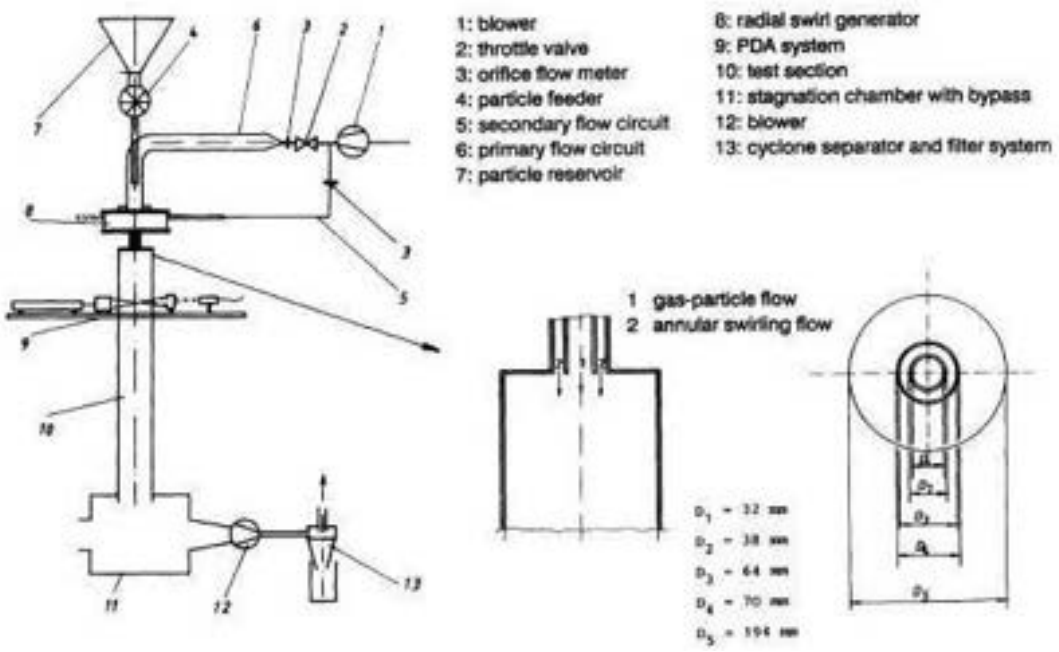

Figure 3.1: Sommerfeld and Qiu experimental set-up. (From ref [45])

the range typically used for these applications, though the mean diameter is smaller ($\sim 45\ \mu$m) here compared to the one ($\sim 100 \div 200 \mu$m) usually adopted for power plant burners.

The test case conditions are summarized in the following table while in Figure 3.2 the computational domain is reproduced. The test chamber is 0.703 m long while the inlet duct length is 0.127 m. The expansion chamber is 0.464 m long and has a diameter $D_6 = 0.630$ m. The other radial dimensions are those reported in Figure 3.1

Air flow	
Mass flow rate of the primary jet M_{f1} (g/s)	9.9
Mass flow rate of the secondary jet M_{f2} (g/s)	38.3
Inlet Reynolds number (with D_3 = 64 mm)	52400
Swirl number	0.47
Particle phase	
Particle mass flow rate M_p (g/s)	0.34
Particle loading in the primary jet	0.034
Particle properties	
Particle mean diameter (μm)	45
Particle material density (kg/m^3)	2500

Table 3.1: Flow conditions and particle properties for the Sommerfeld and Qiu experiment

Figure 3.2: Computational domain (left) and a detail of the inlet (right)

3.1.1 Computational grid

The computational grid is structured and cylindrical. It is composed by 4 blocks: two for the inlet ducts, one for the test chamber and one for the expansion chamber. All these blocks present 64 azimuthal planes. In Figure 3.3 the overall grid and the grid distribution in radial planes for the different blocks is presented. In Table 3.2 the grid dimensions with minimum and maximum step size for each direction are reported. As to the axial distribution, a uniform step size $\Delta z = 0.001$ m is adopted in the inlet ducts and in the first part of the test chamber. After $z = 0.2$ m ($z = 0$ m is the section where the inlet flow enters the test chamber) the grid step size is gradually increased. At the last experimental station ($z = 0.315$ m) it is $\Delta z = 0.0035$ m. The distribution of the grid

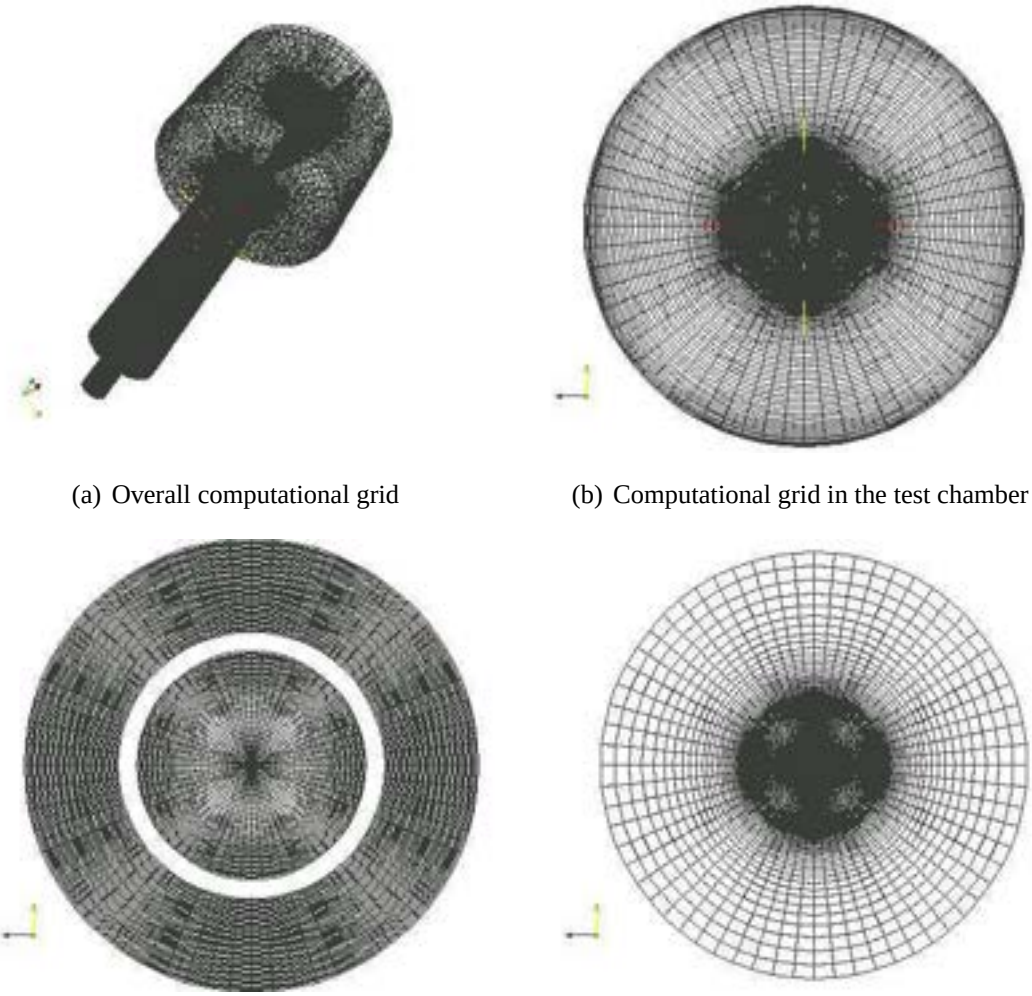

(a) Overall computational grid

(b) Computational grid in the test chamber

(c) Computational grid in the inlet zone

(d) Computational grid in the expansion chamber

Figure 3.3: Computational grid

steps in the radial direction starts with $\Delta r = 0.0007$ m close to the axis and it decreases

down to $\Delta r = 0.0002$ m before the inner duct wall. It is then kept constant through the entire annular duct and only for $r > D_3$ (see Figure 3.1) the step size is gradually increased up to $\Delta r = 0.002$ m before being decreased again down to 0.00064 m at the test chamber walls.

Block	$N_z \times N_r \times N_\vartheta$	Δz_{min}[m]	Δz_{max}[m]	Δr_{min}[m]	Δr_{max}[m]
Inner inlet duct	$(128 \times 38 \times 64)$	0.001	0.001	0.0002	0.0007
Annular inlet duct	$(128 \times 52 \times 64)$	0.001	0.001	0.0002	0.0002
Test chamber	$(306 \times 158 \times 64)$	0.001	0.011	0.0002	0.002
Expansion chamber	$(32 \times 192 \times 64)$	0.011	0.02	0.0002	0.02

Table 3.2: Grid characteristics for each block

3.1.2 Boundary conditions

Appropriate boundary conditions must be specified for both phases at the inlet, at the outlet and at the walls.

Inlet boundary conditions

At the inlet section the momentum, temperature and species mass fractions are specified for the gas phase.

The following law, reproducing a developed turbulent mean profile in a cylindrical duct, is imposed for the internal duct

$$\begin{aligned} \rho_f u_{f,r}(r) &= 0 \\ \rho_f u_{f,\vartheta}(r) &= 0 \\ \rho_f u_{f,z}(r) &= (\rho_f u_{f,z})^{MAX} \left(\frac{D_1 - 2r}{D_1} \right)^{\frac{1}{n^t}} \\ (\rho_f u_{f,z})^{MAX} &= M_{f,1} \frac{(2n^t+1)(n^t+1)}{2(n^t)^2 A^{(1)}} \\ A^{(1)} &= \frac{D_1^2 \pi}{4} \end{aligned} \tag{3.1}$$

with $n^t = 8$. At the inlet of the annular duct the following laws are imposed in order to grant the right swirl number at the test chamber inlet.

$$
\begin{aligned}
\rho_f u_{f,r}(r) &= 0 \\
\rho_f u_{f,z}(r) &= \frac{M_{f,2}}{A^{(2)}} \\
\rho_f u_{f,\vartheta}(r) &= \begin{cases} \frac{\rho_f u_{f,z}(r)}{0.06} \tan\left(\frac{\pi}{2.81}\right) r & r \leq R_M = \frac{D_3}{2} - 0.003 \\ \rho_f u_{f,z}(R_M)\left(1 - \frac{r - R_M}{\frac{D_3}{2} - R_M}\right) & r > R_M \end{cases} \\
A^{(2)} &= \frac{D_3^2 - D_2^2}{4}\pi
\end{aligned}
\tag{3.2}
$$

It can be seen how a constant axial momentum is imposed while two distributions linear with the radius are used for the azimuthal component. Finally, for the temperature and the mixture fractions the following values are imposed

$$
\begin{aligned}
T_f &= 300K \\
Y_{O_2} &= 0.2 \\
Y_{N_2} &= 0.8
\end{aligned}
$$

In order to reproduce a turbulent inlet, a technique [46] to generate synthetic turbulence inflow with coherence in both space and time has been implemented in the HeaRT code.

As to the dispersed phase, due to the upwind nature of the equations (no characteristics coming from the domain) all the variables must be imposed. Particles enter the inlet duct at the same velocity and temperature of the gas. The volumetric fraction α_p is obtained from the mass flux M_p

$$\alpha_p = \frac{M_p}{\rho_p u_{p,z}} \frac{4}{\pi D_1^2} \tag{3.3}$$

and the particle number from the particle diameter d_p

$$n_p = \frac{6\alpha_p}{\pi d_p^3} \tag{3.4}$$

In the present validation a monodispersed class of particles with $d_p = 45$ μm is simulated. Finally a particle temperature of 300 K is imposed and null gradient for turbulent viscosity is also set.

Outlet boundary conditions

Partially non-reflecting boundary conditions based on the characteristic waves [47] are applied at the outflow for the gas phase. The asymptotic pressure is set to 1 atm. Null gradient for shear viscous stresses are set as suggested in [48].

For the dispersed phase it was sufficient to set $\mathbf{u_p} = \mathbf{0}$ in a ghost cell. The values of the other variables are linearly extrapolated from inside the domain In this way, upwind values coming from the inside are always taken in the reconstruction of the exiting fluxes.

Walls

As to gas phase, adiabatic no-slip conditions are adopted for this calculation. Turbulent viscosities values are extrapolated from inside the domain and only when this extrapolation returns a negative value they are set to zero.

Due to the absence of the uncorrelated motion [15] in the model, the dispersed phase has been treated at the walls in the same way as at the outlet. This choice was made in order to avoid a progressive accumulation of particles at the corners. It is in fact impossible to reproduce the effect of particles hitting the walls and rebounding off without taking into account the uncorrelated motion.

3.1.3 Code settings

In order to keep the calculation stable it was necessary to add artificial viscosity by increasing the value of the SGS calibration constant. $\sigma^{SGS} = 2$ has thus been set for the present calculation. This choice, due to the poor resolution of the computational grid in the azimuthal direction will obviously have an impact on the calculation quality. However, this problem is grid depending and does not subtract generality to the conclusions of the present work. The reflection coefficient for the outlet boundary conditions K^{out} has been set to 0.1. As to the stability coefficients (see section 2.3) the following constraints have been used

$$CFL = 0.25 \qquad VNN = 0.1$$

3.2 Results

In the following sections the results for the gas and the dispersed phase will be presented.

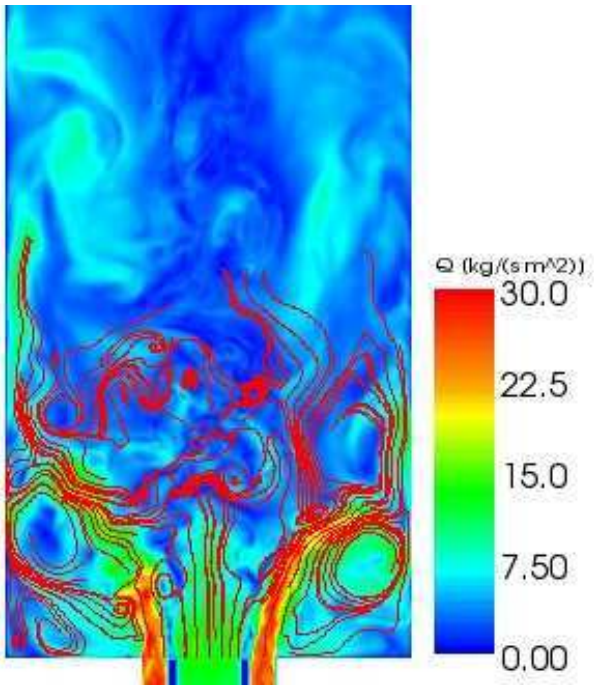

Figure 3.4: Gas phase velocity field structure

3.2.1 Gas phase

In Figure 3.4 the field structure of the gas phase momentum is presented for a given instant, for the test section zone. A radial plane is shown where the streamlines are drawn. The streamlines are in each point parallel to the gas phase velocity component laying on the plane. The momentum module $|\rho u_f|$ of the gas phase is also shown by means of contour levels. Since the gas density is almost constant, showing oscillations on the fourth significant digit around a mean value of $\rho_f = 1.165$ kg/m^3, the contour plots of the momentum closely resemble those of the gas velocity.

The field structure is typical of swirled combustors. Two recirculating zones are present just aside from the injection zone, and extends up to $z \simeq 0.085$ m, where z is the distance from the plane where the injection ducts enter the test chamber. A stagnation point is present at the center of the domain for $z \simeq 0.09$ m, after which a great toroidal recirculation zone extends for more than 20 cm in the axial direction. The instantaneous field shown in Figure 3.4 is characterized by a considerable asymmetry and by the presence of many small structures that only through a LES technique can be captured.

If attention is paid to the single components of the momentum, it is more difficult to see the smallest structures but the overall behavior of the momentum field is clearer.

In Figure 3.5(a) the axial momentum is presented while the azimuthal momentum is shown in Figure 3.5(b). From Figure 3.5(a) it is clear how the mass flux, due to the swirled flow entering from the annular duct, is mainly constrained in the outer part of the test chamber. The complexity of the flow structure is instead well reproduced in Figure 3.5(b), where it can be seen how the azimuthal momentum is redistributed through the all domain, due to turbulence effects. If the attention is focused in particular on the central recirculation zone, it can be seen how the fluctuations in the azimuthal momentum are larger than those in the axial direction. Finally, in order to give the best idea of the three-dimensional structure of the flow field, the module of the gas phase momentum over an axial and a radial plane normal to the axis is presented in Figure 3.6(a)-Figure 3.6(d). Four different positions for the radial plane are considered from $z = 45$ mm to $z = 345$ mm.

As already mentioned above, only small fluctuations are present in the gas phase density. There are no large structures to be seen in Figure 3.7, where the distribution of this variable is presented. The texture-like appearance of the density distribution could be due to the spherical waves that are released from the injection plane. This is

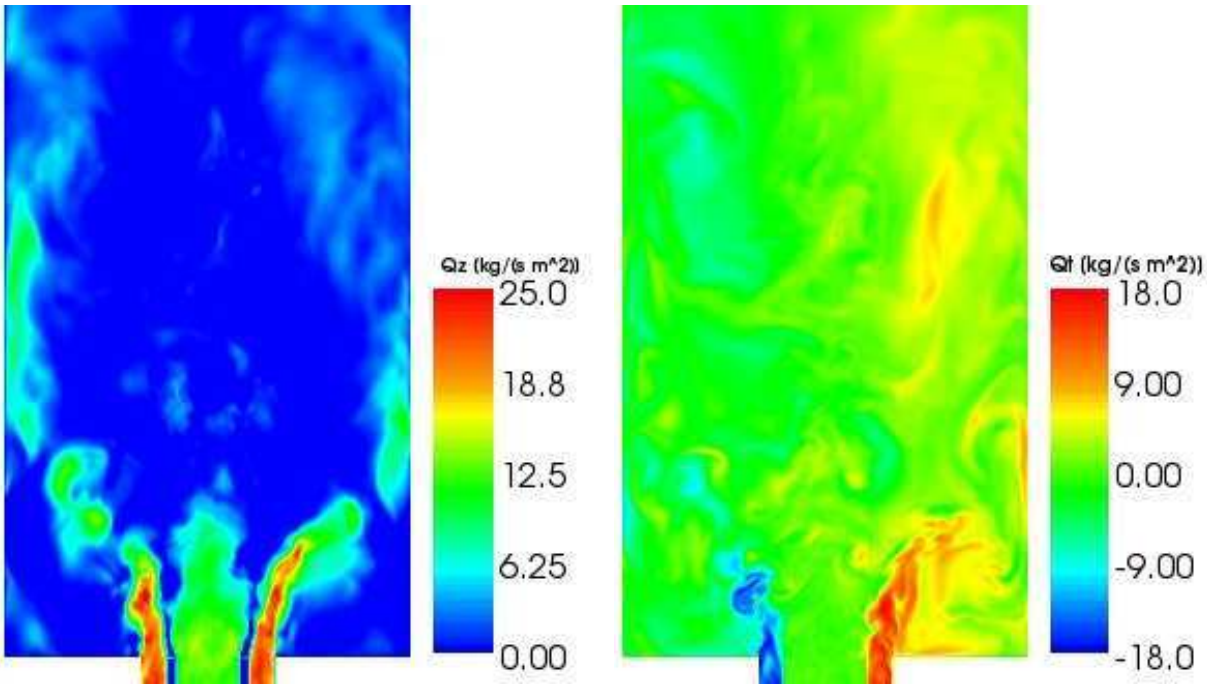

(a) (b)

Figure 3.5: Gas phase momentum field. Axial (a) and azimuthal (b) momentum

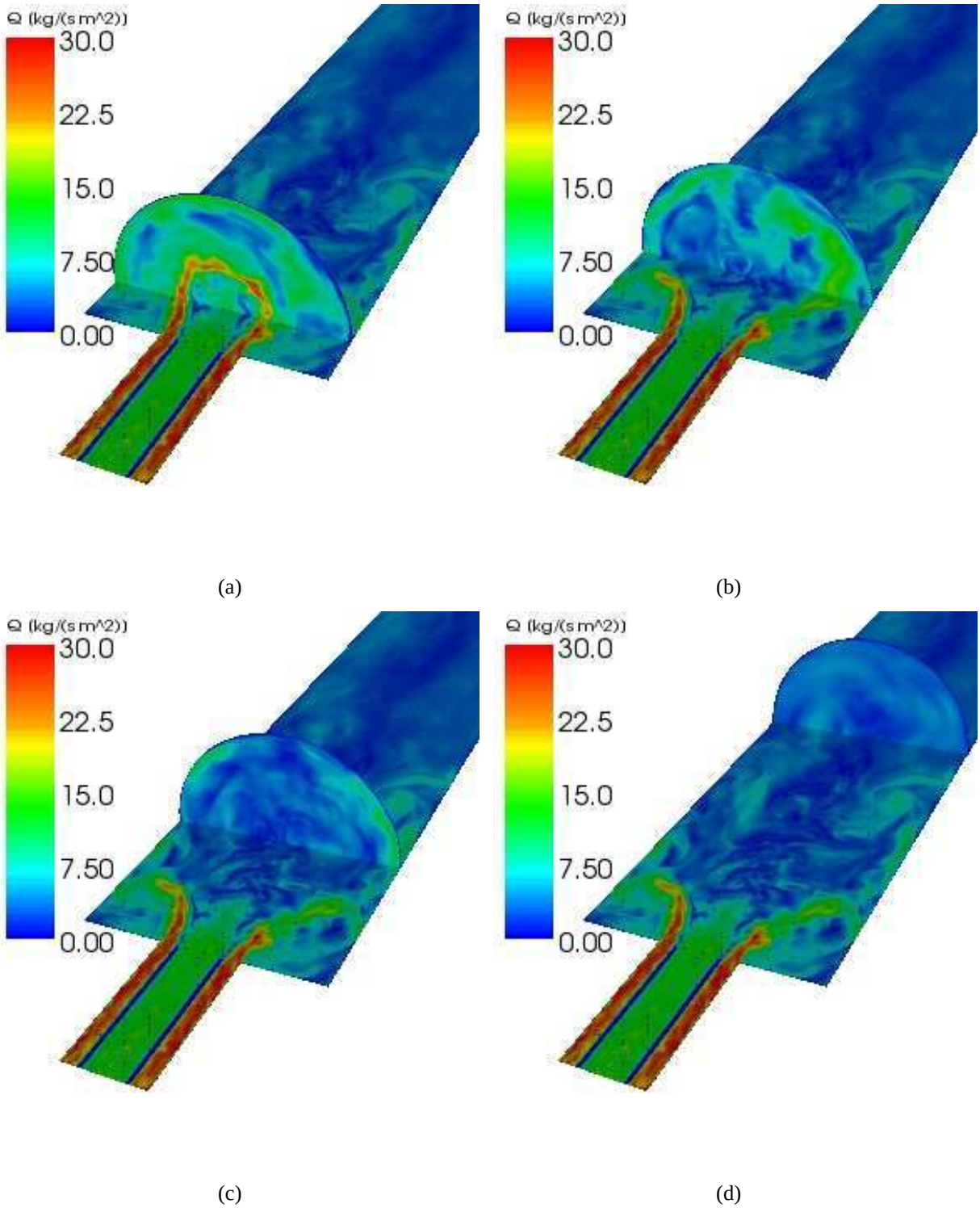

Figure 3.6: Instantaneous field of the momentum module ρ_f. Four positions for the plane normal to the axis are considered: (a) $z = 45$ mm; (b) $z = 90$ mm; (c) $z = 150$ mm; (d) $z = 345$ mm

due to the vortex shedding present at both sides of the annular duct entrance in the test

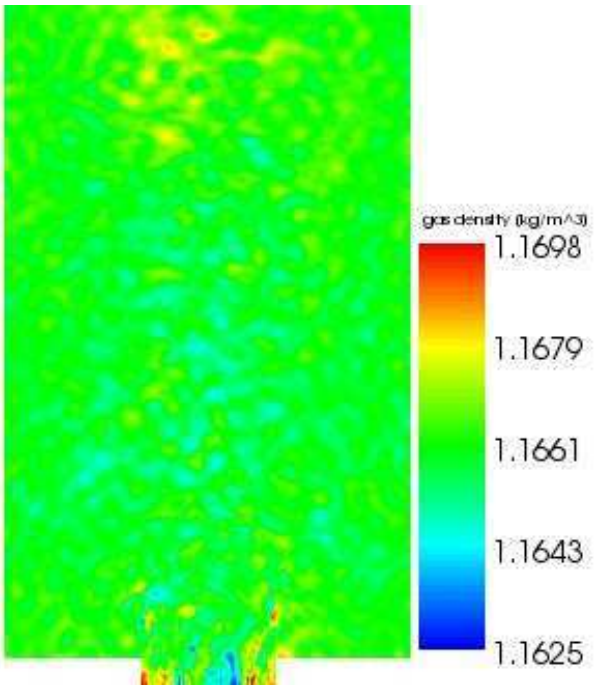

Figure 3.7: Instantaneous field of the gas phase density ρ_f

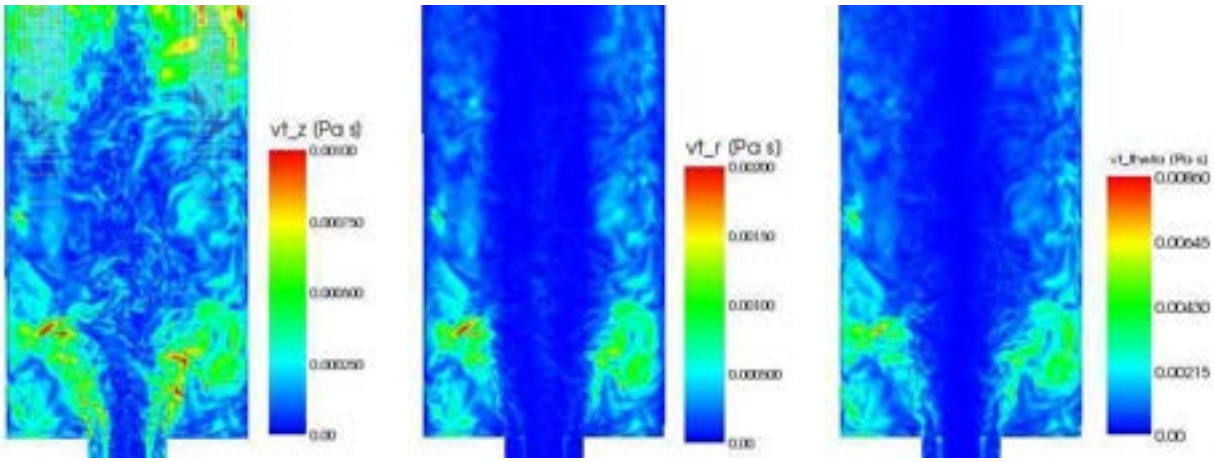

(a) (b) (c)

Figure 3.8: Instantaneous field of the eddy viscosities: $\mu_{t,z}$ (a), $\mu_{t,r}$ (b), $\mu_{t,\theta}$ (c)

chamber. Spherical waves are then reflected at the walls and reflected waves interact with the released ones.

The temperature and pressure distributions are similar to the density one and do not add anything in the result analysis. They are therefore omitted here.

In Figures 3.8(a)-3.8(c) the distribution of the eddy viscosities applied to the principal directions (z, r and ϑ respectively) are presented. In Figure 3.8(a) it has been

chosen to use a wireframe representation in order to give an idea of the zone where the computing grid gets coarser. The step size in z-direction Δz is gradually increased after $z = 0.15$ m from $\Delta z = 1$ mm to $\Delta z = 5.5$ mm, while Δr has its maximum around $r = 0.08$ m. By comparing Figures 3.8(a) and 3.5(a) it can be seen how the higher values for $\mu_{t,z}$ can be found in the mixing layer of the annular flow, close to the injection plane, and after the central recirculation zone. Although the velocity fluctuations are much greater close to the injection plane than in the second region, the modelled eddy viscosities are comparable in the two zones. The reason may be searched in the linear dependence of the eddy viscosities on the different filter scales of the directions they are applied to, as described in in section 1.3. At the upper part of the figure Δz is five times greater then in the lower part, which counteracts the decrease of the amplitude of the velocity fluctuations. Another thing that can be observed in the upper part of Figure 3.8(a) is the fact that the value of $\mu_{t,z}$ is greater where the grid in the r-direction is more refined. This may be an evidence of the fact that the filter scale along z is outside the inertial range. In this region, the filter scale Δz is the intermediate one. The fluctuations extracted from the high pass filters along directions r and ϑ will be rescaled using the equations (1.80) on Δz. Nevertheless, it must be remembered that these equations relay on the hypothesis of being inside the inertial range of turbulence. If one tries and rescales the fluctuations measured outside the inertial range on a lengthscale inside of it, he will finally get a fluctuation much smaller than it should be. On the contrary, if one measures a velocity fluctuation inside the inertial range and uses (1.80) to rescale it on a lengthscale outside of this range, he will obtain a great overestimation of this fluctuation.

It has already been pointed out that the greatest velocity fluctuations can be found in the mixing layer of the annular duct flow. Both $\mu_{t,r}$ and $\mu_{t,\vartheta}$ have their maximum values in this region. Since Δr and $\Delta\vartheta$ are greater than Δz there, the highest values of $\mu_{t,r}$ and $\mu_{t,\vartheta}$ are greater than the one of $\mu_{t,z}$ and they present overall greater values in the regions where the respective filter lengthscales are larger.

Validation against the experimental data

In this section the comparison between the experimental data and the results computed in the present work will be presented. Data from the computation have been sampled over an interval of $\Delta t = 0.04$ s, which represents approximately two times the revolution period of the lateral recirculation zones.

In Figure 3.9 the experimental data and the computed solution are presented for the plane at $z = 3$ mm, thus very close to the injection plane. Solid lines refer to the present work while dashed lines are taken from [49] and have been obtained by means of the AVBP code for comparison. In Figures 3.9(a) and 3.9(c) it can be recognized how both mean values and fluctuating velocities are well reproduced. The radial positions of local maximum are perfectly caught, the magnitudes are in very good agreement with the experiments. The same cannot be said for the radial component. Both the shape and the level of the RMS are not well predicted. This can be due to the poor resolution adopted in front of the bluff body separating the inner and outer duct. In fact, since $\Delta z = 3$ mm only 3 grid points are present before the plane where the measures are taken and it will not be possible to reconstruct smaller structures in that zone.

In Figure 3.10 the computed solution is compared to the experimental data for $z = 52$ mm. In Figure 3.10(a) it can be seen how both the mean and RMS axial velocities are very well reproduced by the HeaRT code. On the contrary, for both radial and tangential components, the RMS velocities are very well predicted at all the radial positions with a slight overprediction for the tengential component.

At $z = 85$ mm the mean radial component is well predicted close to the center of the domain and in the outer part. The axial component presents an underprediction in the central part. This may be an effect of the spourious particle accumulation in the stagnation region. The simulation has been run for nearly 20M iterations in order to test different strategies and this eventually led to this problem. Once the code has been developed this is not expected to happen under normal conditions.

In Figures 3.12-3.15 the comparison between experimental and computed data for planes at $z = 112$ mm, $z = 155$ mm, $z = 195$ mm and $z = 315$ mm. The mean velocities are well predicted. The overall level of the fluctuations is generally well reproduced. Local underpredictions by a $30\% - 50\%$ appear expecially moving far away from the injection zone, where the grid step in the axial direction becomes larger.

In order to improve the solution, the calculation should be performed on more regular grid, expecially in the azimuthal direction. The constraint to use structured cylindrical grids requested by the HeaRT code makes it unfeasible. Studies are on the way in ENEA to release at least one of the two constraints (structured or cylindrical). Only when these improvements will be available it will be possible to try and obtain better results.

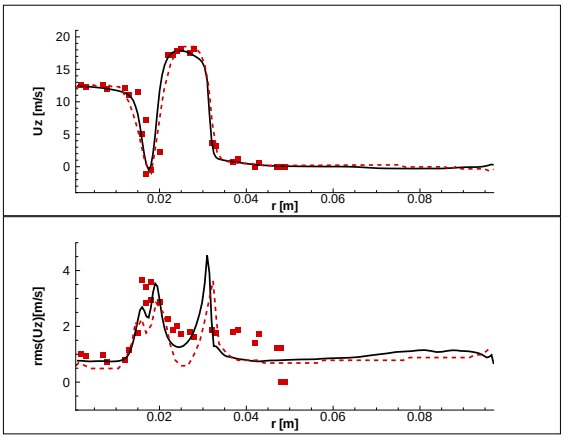

(a)

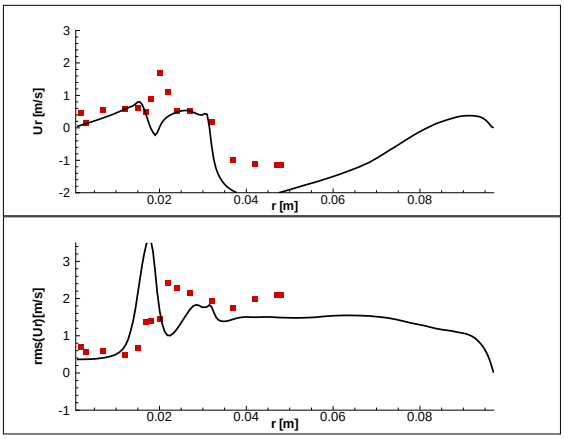

(b)

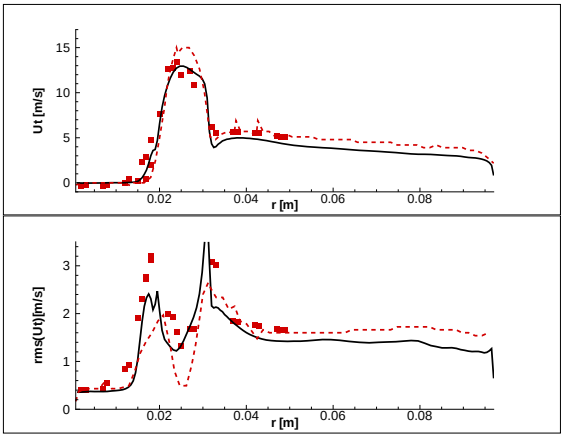

(c)

Figure 3.9: Mean (upper part) and RMS (lower part) axial (a), radial (b) and tangential (c) velocities for $z = 3$ mm. Symbols are taken from experiments. Lines are computed

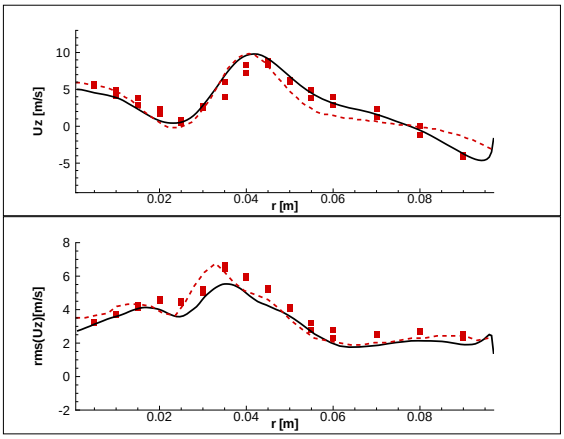

(a)

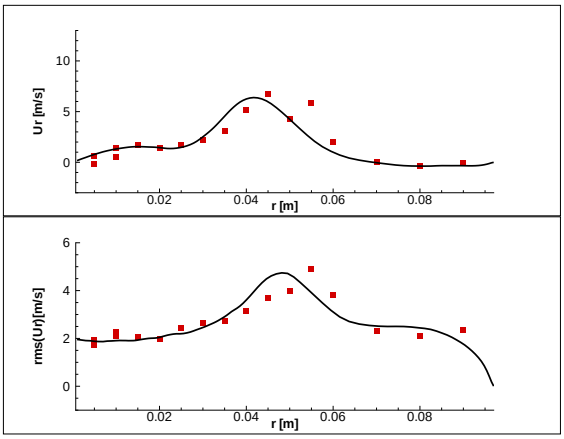

(b)

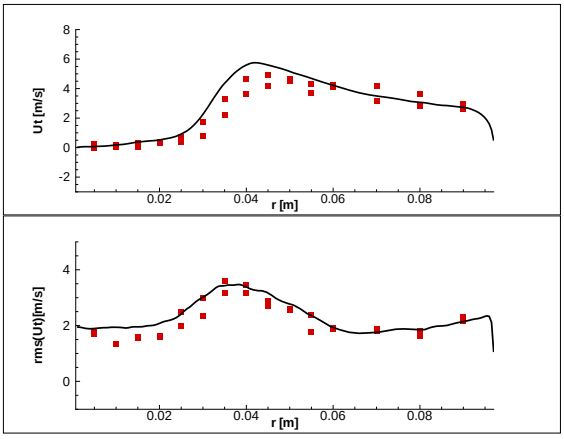

(c)

Figure 3.10: Mean (upper part) and RMS (lower part) axial (a), radial (b) and tangential (c) velocities for $z = 52$ mm. Symbols are taken from experiments. Lines are computed

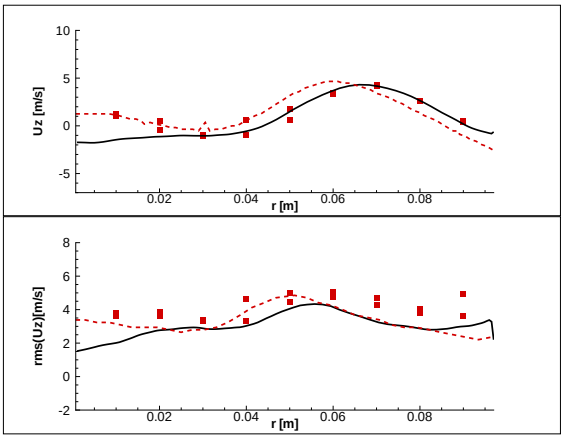

(a)

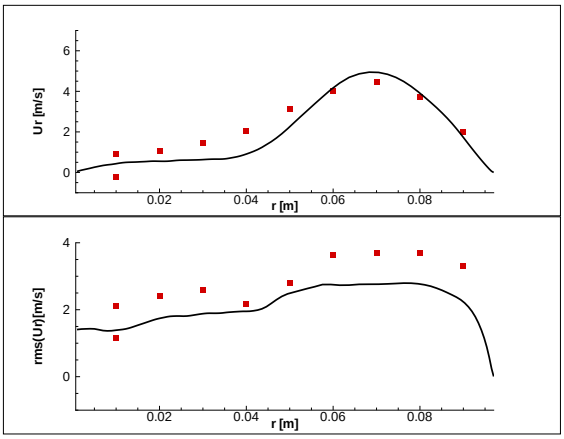

(b)

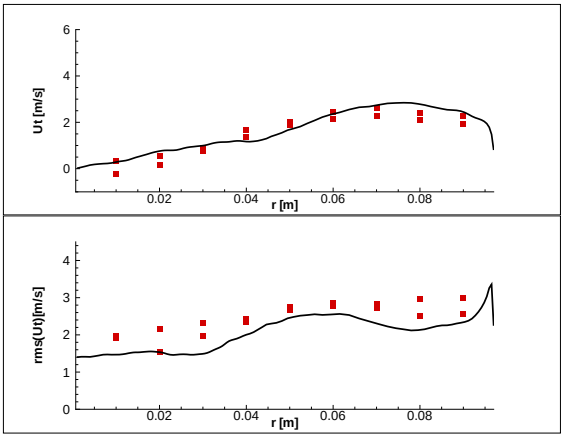

(c)

Figure 3.11: Mean (upper part) and RMS (lower part) axial (a), radial (b) and tangential (c) velocities for $z = 85$ mm. Symbols are taken from experiments. Lines are computed

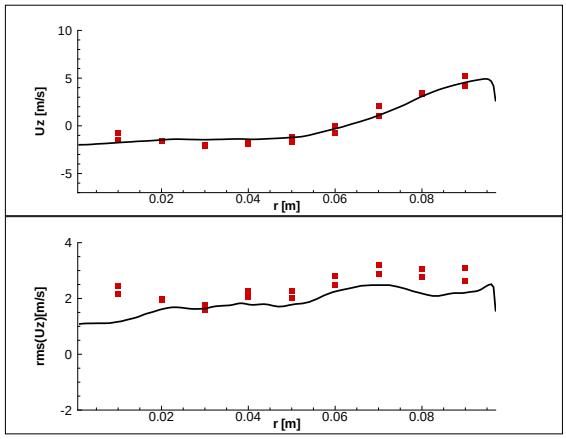

(a)

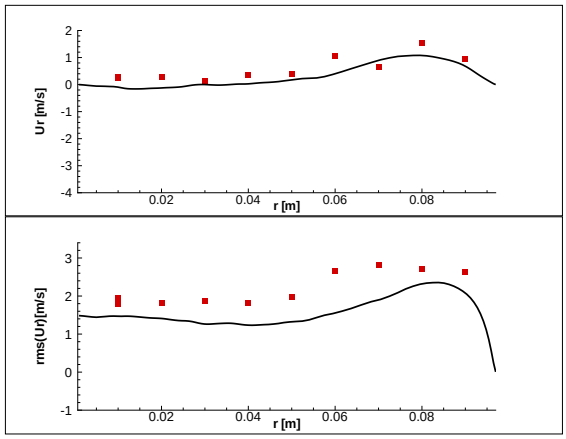

(b)

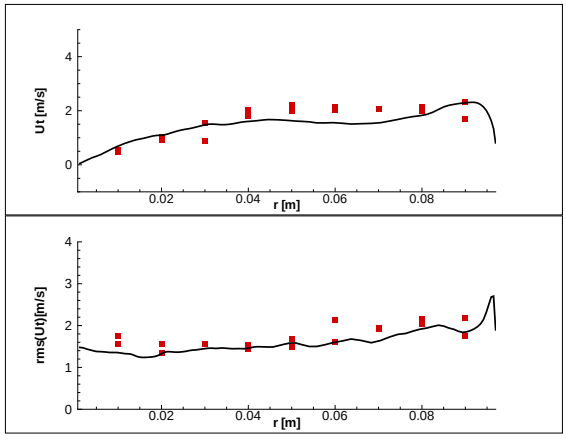

(c)

Figure 3.12: Mean (upper part) and RMS (lower part) axial (a), radial (b) and tangential (c) velocities for $z = 112$ mm. Symbols are taken from experiments. Lines are computed

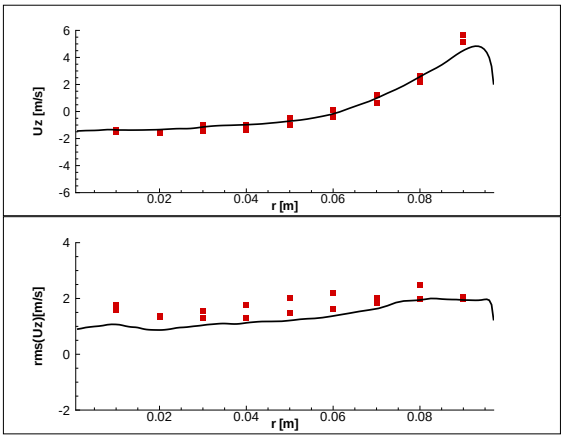

(a)

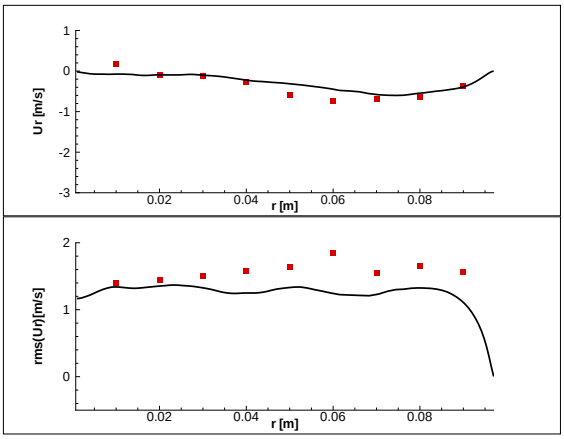

(b)

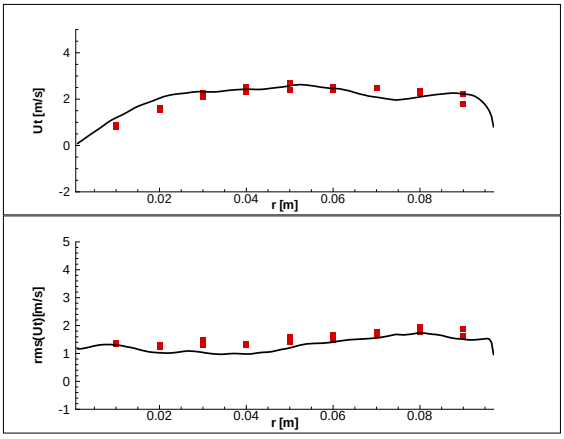

(c)

Figure 3.13: Mean (upper part) and RMS (lower part) axial (a), radial (b) and tangential (c) velocities for $z = 155$ mm. Symbols are taken from experiments. Lines are computed

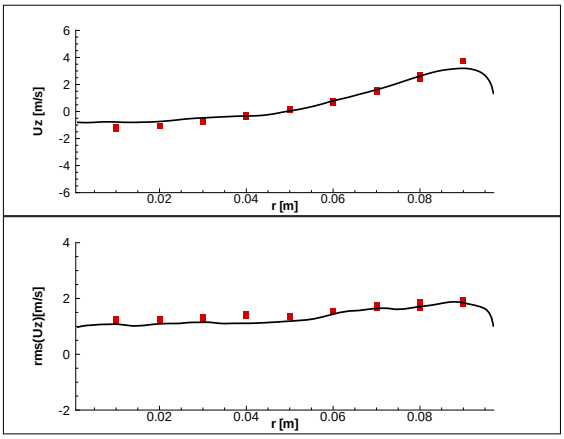

(a)

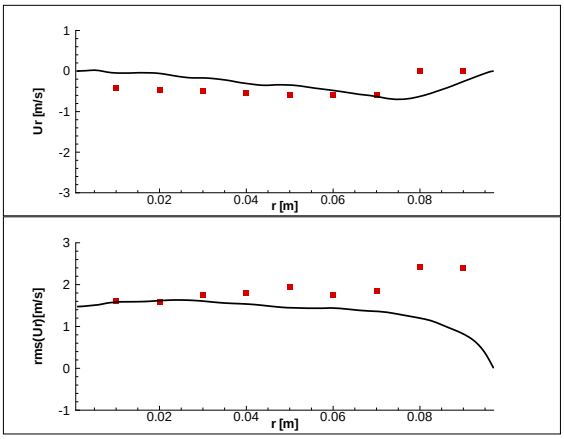

(b)

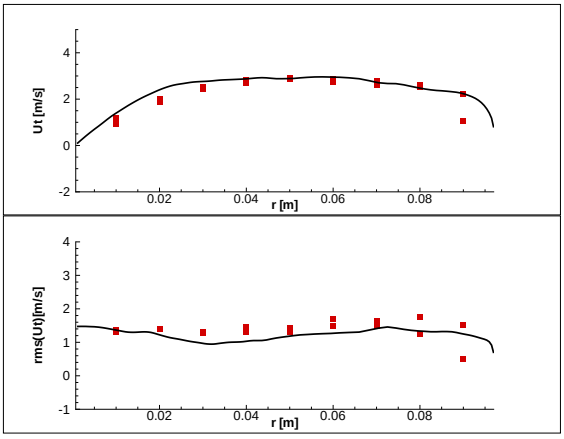

(c)

Figure 3.14: Mean (upper part) and RMS (lower part) axial (a), radial (b) and tangential (c) velocities for $z = 195$ mm. Symbols are taken from experiments. Lines are computed

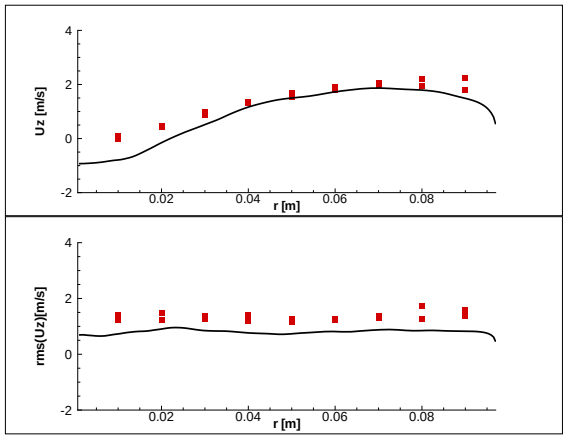

(a)

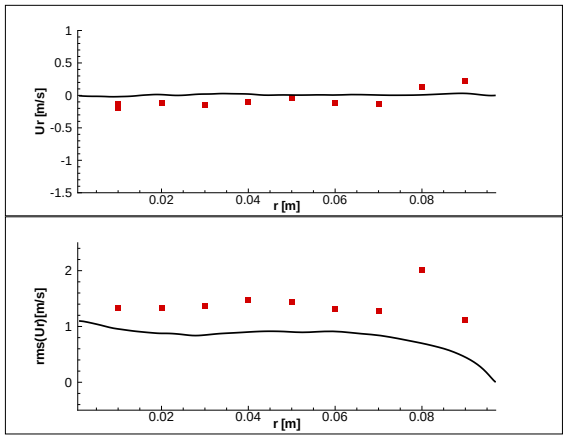

(b)

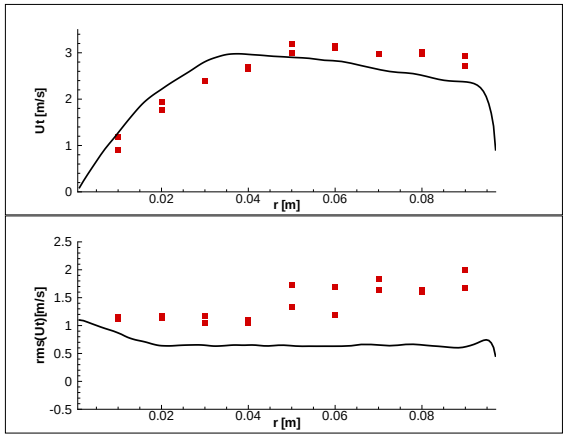

(c)

Figure 3.15: Mean (upper part) and RMS (lower part) axial (a), radial (b) and tangential (c) velocities for $z = 315$ mm. Symbols are taken from experiments. Lines are computed

3.2.2 Dispersed phase

In this section the results obtained for the dispersed phase will be analyzed.

In Figure 3.16 the distribution of the dispersed phase volumetric fraction is shown. It can be seen how the dispersed phase has the tendency to concentrate in thin layers. This is due to the nature of the equations that have been integrated (see system (1.54)-(1.58)). When the trajectories of two groups of particles cross each other, in this model, they will have to proceed with the same velocity and this will lead to an accumulation process. The latter is sketched in Figure 3.17 a). This process is unphysical when dilute conditions are considered since there is no impact among particles. There is thus no reason for momentum to be transferred from a particle parcel to another. In addition, the equation system (1.54)-(1.58) does not conservate the kinetic energy of the dispersed phase, as it should, when the phase coupling is removed.

What is expected to happen when a particle crosses other particles trajectories under dilute conditions is sketched in Figure 3.17 b) for the case of a fast particle reaching a slower particle front. The fast particle will surpass the slower ones without momentum exchange. If the aerodynamics effects are neglected, both momentum and kinetic energy will be conserved by the system and by the single particles as well. The set-

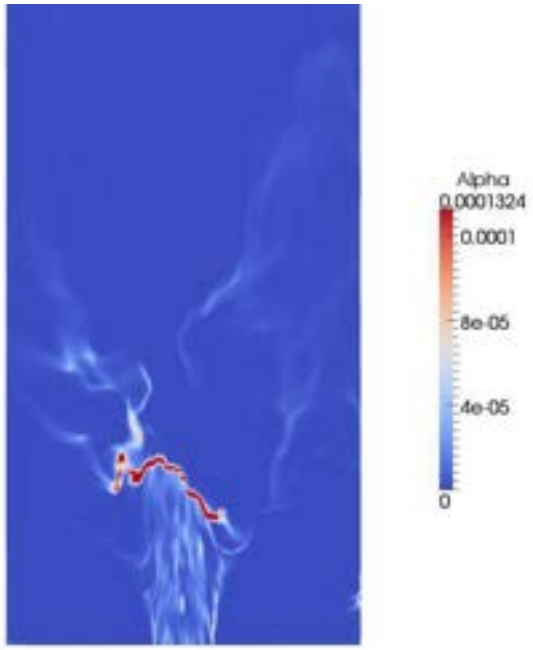

Figure 3.16: Instantaneous field of the dispersed phase volumetric fraction α_p

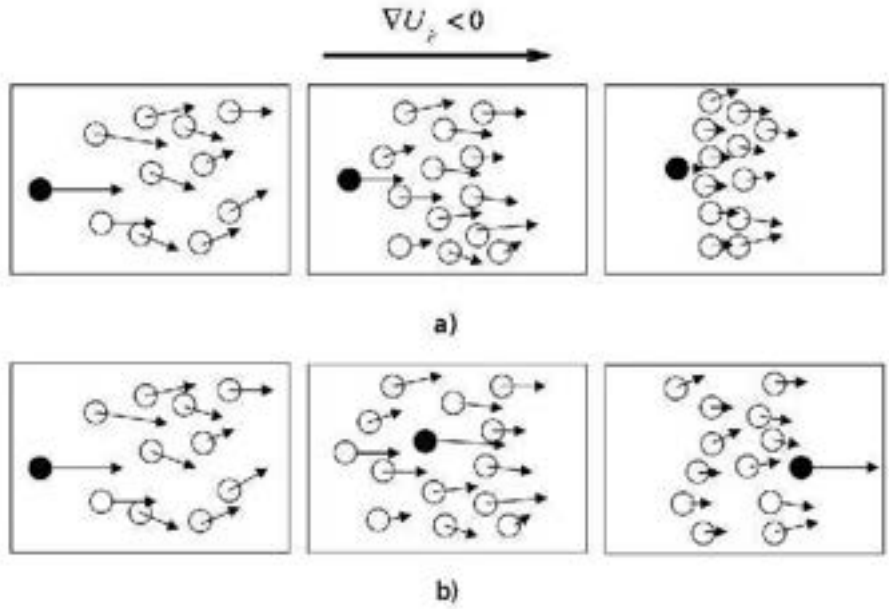

Figure 3.17: Particle accumulation process as seen by the validated model without uncorrelated motion a) and real physical behaviour b)

tlement of such a spourious particle concentration in the stagnation regions will have the tendence to increase during the simulation, due to an accumulation process. This will eventually affect the experimental data and, if not controlled, may take the model outside of the hypothesis of dilute regimes. This has happened in this simulation since it has been used to develop the code and almost 20M iterations have been performed, but is not expected to happen for normal simulations. As already mentioned, possible solutions to this problem have already been investigated [15]

In Figures 3.18 and 3.19 three-dimensional views of the distribution of the dispersed phase volume fraction α_p is shown. It can be seen, besides the attitude to concentrate in small volumes, how the action of the gas phase is sufficient to induce the particle dispersion. In Figure 3.19, in particular, isosurfaces of α_p are presented for different levels of this variable. The isocontour colours refer to the particle velocity. It can be seen how the condensed phase is dispersed in a large variety of structures. If attention is paid to the upper part of Figure 3.19(d), for example, the effect of the swirl on particle distribution is clearly visible.

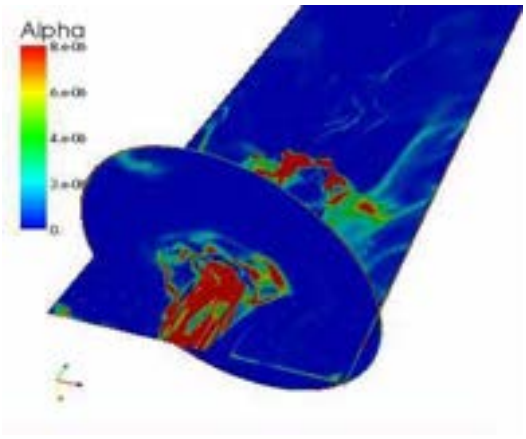

(a)

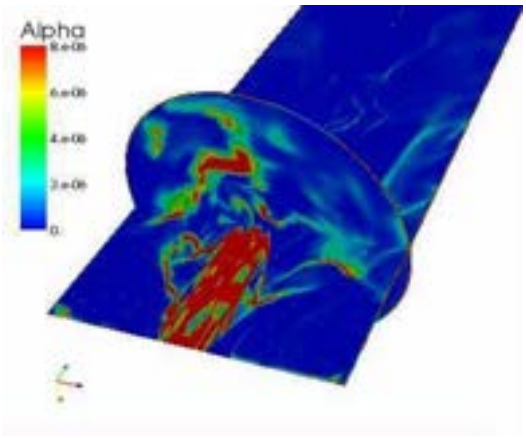

(b)

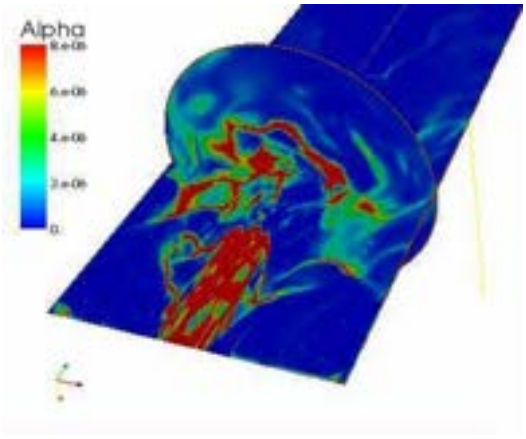

(c)

Figure 3.18: Instantaneous field of the dispersed phase volume fraction α_p for different positions of the plane normal to the axis: (a) $z = 0.05$ m; (b) $z = 0.1$ m; (c) $z = 0.15$ m

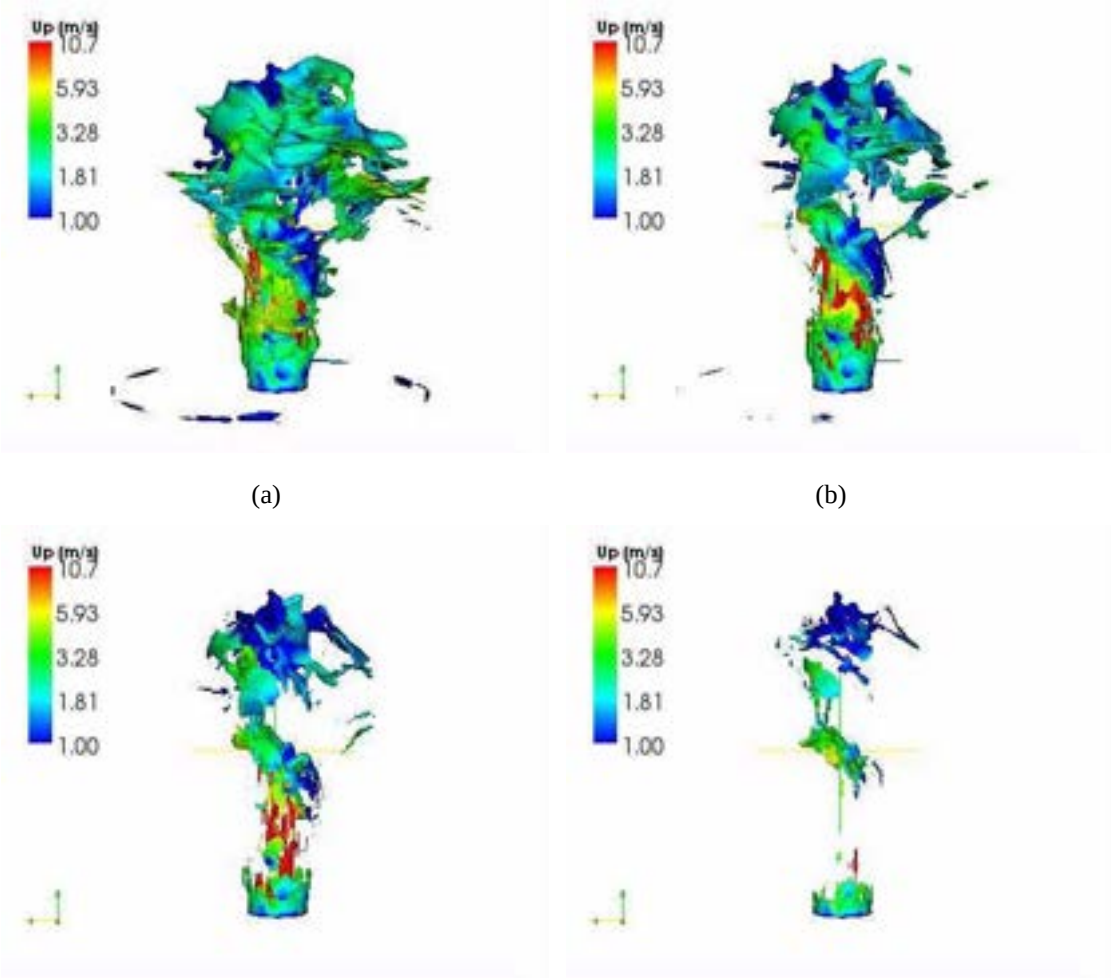

Figure 3.19: Instantaneous isosurfaces of the dispersed phase volume fraction α_p: (a) $\alpha_p = 1.e-5$; (b) $\alpha_p = 2.e-5$; (c) $\alpha_p = 4.e-5$; (d) $\alpha_p = 8.e-5$

In Figure 3.20 the distributions of the particle velocity components are shown. It can be seen how the fluctuations for particle velocity are less marked than for the gas flow. The axial component maintains high values for a larger extension with respect to the gas phase, meaning that particles follow the gas phase motion with some delay, as they are expected to do.

This conclusion is even clearer when attention is paid to Figure 3.21 where the field of the particle velocity module is presented together with isolines showing where $\alpha_p = 10^{-6}$. It can be observed that most of the particles are concentrated inside the central recirculation zone, where the low velocity induce an accumulation effect.

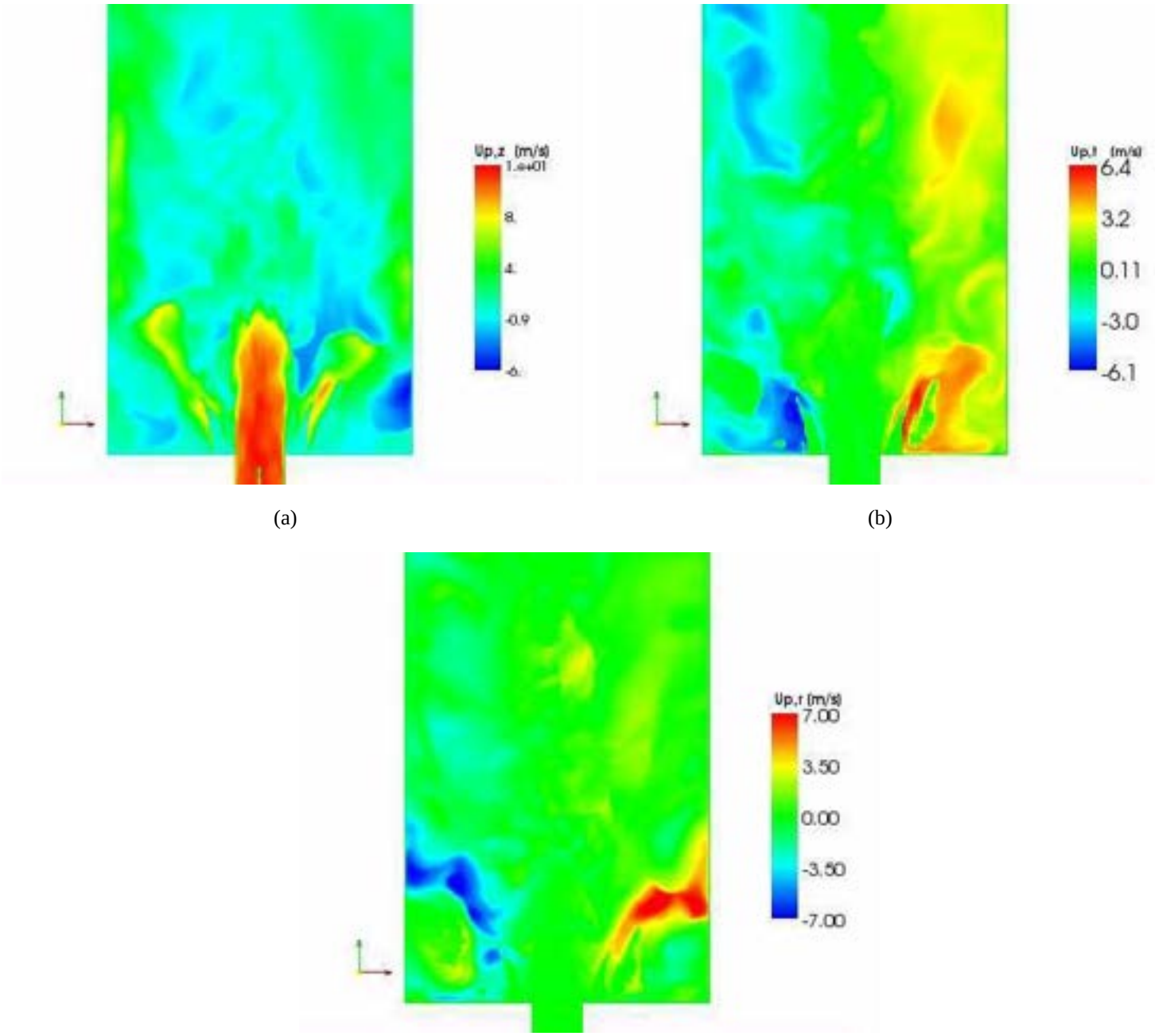

(a) (b)

(c)

Figure 3.20: Instantaneous field of the dispersed phase velocity u_p: (a) $u_{p,z}$; (b) $u_{p,\vartheta}$; (c) $u_{p,r}$

Validation against the experimental data

In Figures 3.22-3.28 the comparison between the experimental mean and RMS velocities of the dispersed phase are presented. In Figure 3.22 the results for $z = 3$ mm is shown. It can be seen how the RMS velocities are undervalued by the present model. The reason is to be searched in the particle accumulation process that has been de-

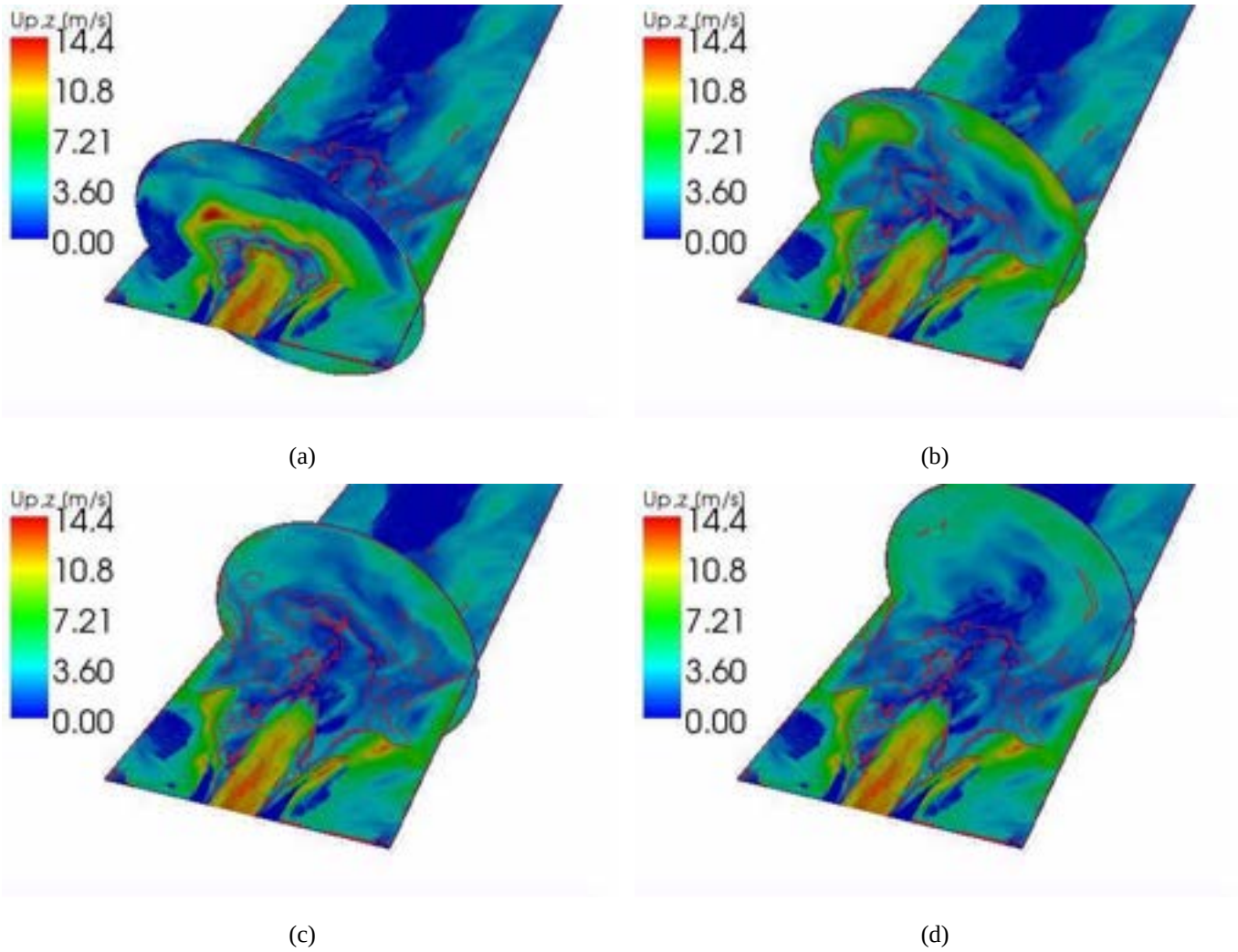

Figure 3.21: Instantaneous field of the dispersed phase velocity u_p for different positions of the plane normal to the axis: (a) $z = 0.05$ m; (b) $z = 0.1$ m; (c) $z = 0.15$ m; (d) $z = 0.204$ m. The isolines refer to $\alpha_p = 10^{-6}$

scribed: the model do not conservate the kinetic energy and small scale fluctuations are thus destroyed.

At greater distances from the injection plane ($z = 0$ mm), the solution is acceptable. Low levels of axial RMS velocities can be seen in Figure 3.23(a) but these are comparable with other codes (CERFACS AVBP) results also presented in the figure. The reason for the underprediction in the azinuthal RMS velocities shown in Figure 3.23(c) is under investigation but it may be again due to an excess in the particle concentration.

Tha values at planes at greater distance from the injection are well captured as far as the mean components are considered. Underpredictions can be seen for the radial RMS in the external part of the domain in Figures 3.24(b)-3.28(a) and are mainly inherited

from the gas phase solution.

Other sources of misprediction are instead due to the dispersed mode itself. Besides the dissipation of the kinetic energy of the smaller turbulent scales, that has already been outlined while discussing Figure 3.22, in Figures 3.26(a) and 3.27(a) it can be seen how, close to the axis, the dispersed phase axial velocity is zero when a positive component is expected. It is here hard to say whether the mechanism that leads to this misprediction is the same that leads to the small scales kinetic energy destruction. It must be outlined anyway that the mean axial gas velocity at higher values of z is negative. Therefore, particles may be trapped in the central recirculation zone and pushed back towards the injection plane by the flow. This would lead these particles to cross the incoming parcels trajectories and then to kinetic energy destruction.

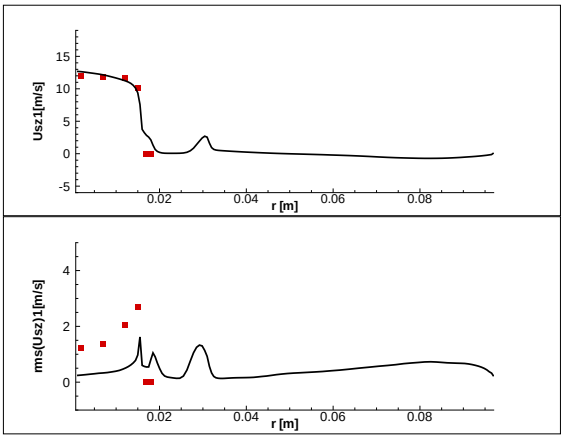

(a)

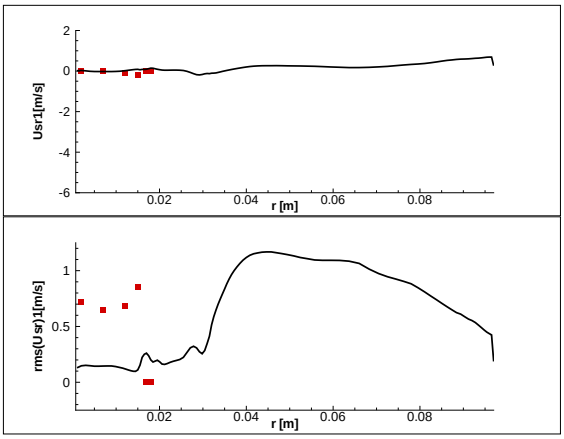

(b)

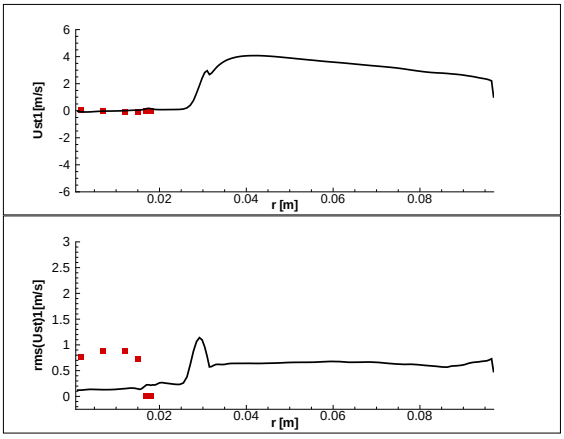

(c)

Figure 3.22: Mean (upper part) and RMS (lower part) axial (a), radial (b) and tangential (c) velocities for $z = 3$ mm. Symbols are taken from experiments. Lines are computed

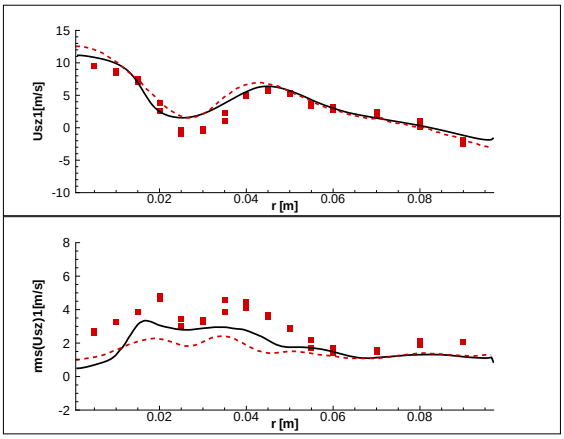

(a)

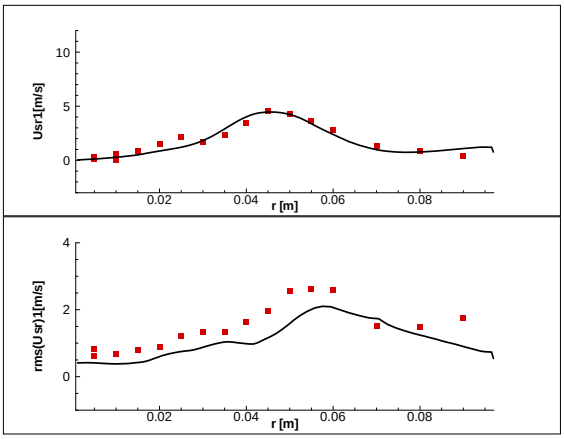

(b)

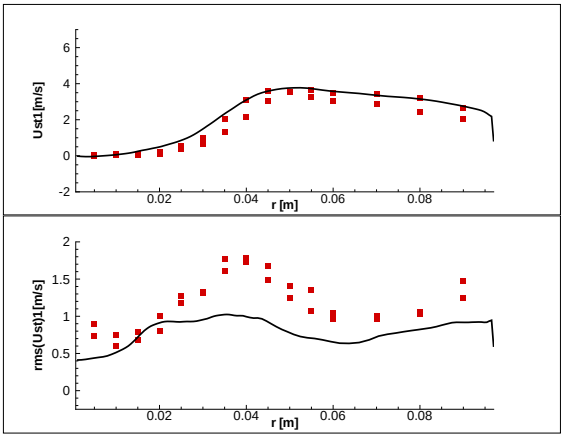

(c)

Figure 3.23: Mean (upper part) and RMS (lower part) axial (a), radial (b) and tangential (c) velocities for $z = 52$ mm. Symbols are taken from experiments. Lines are computed

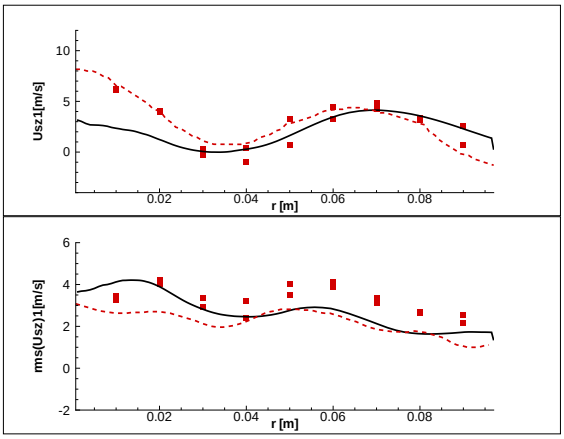

(a)

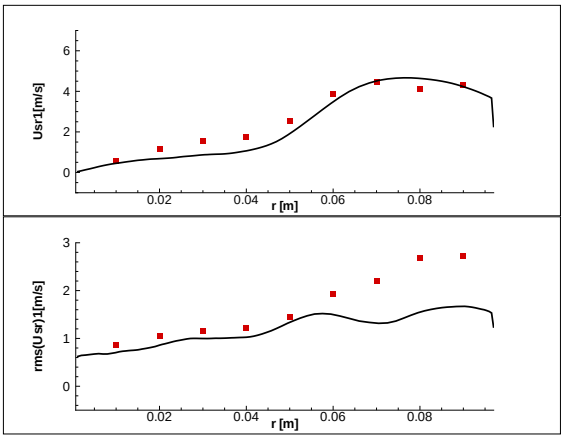

(b)

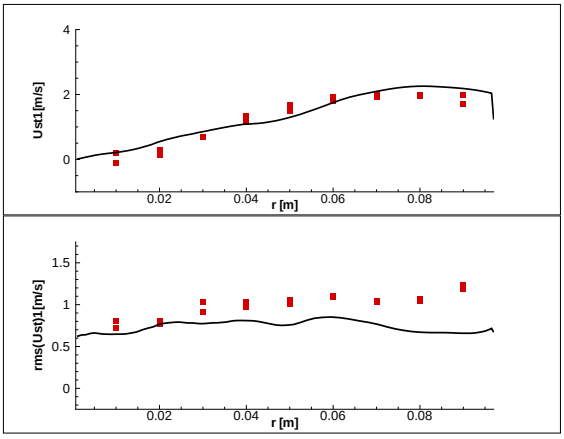

(c)

Figure 3.24: Mean (upper part) and RMS (lower part) axial (a), radial (b) and tangential (c) velocities for $z = 85$ mm. Symbols are taken from experiments. Lines are computed

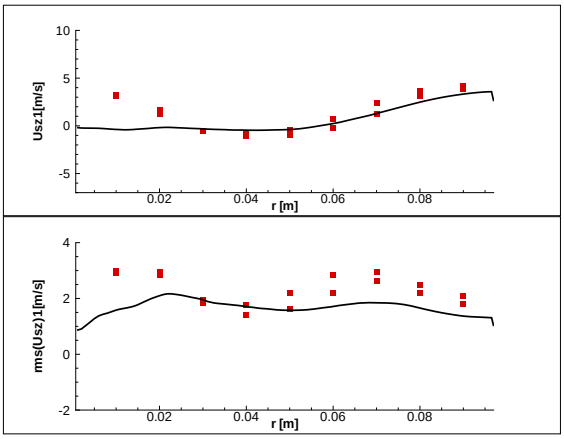

(a)

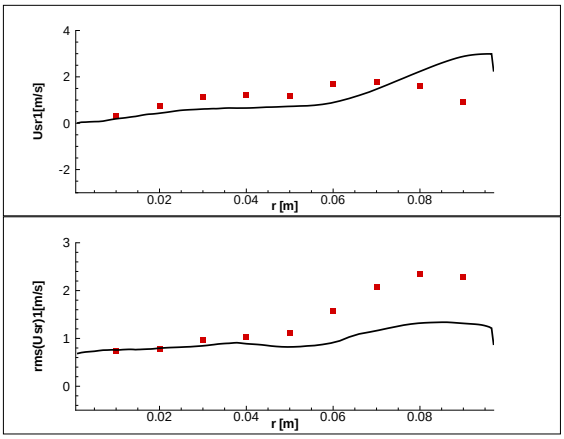

(b)

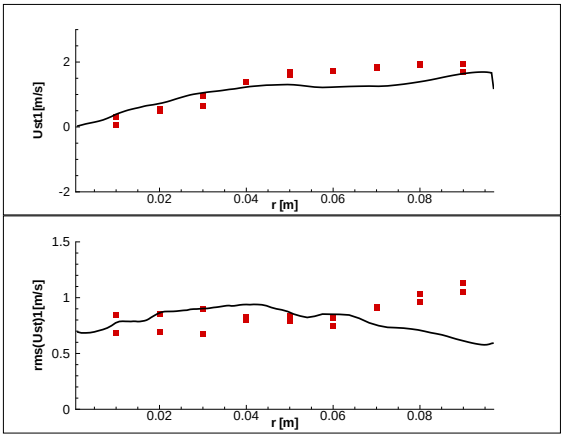

(c)

Figure 3.25: Mean (upper part) and RMS (lower part) axial (a), radial (b) and tangential (c) velocities for $z = 112$ mm. Symbols are taken from experiments. Lines are computed

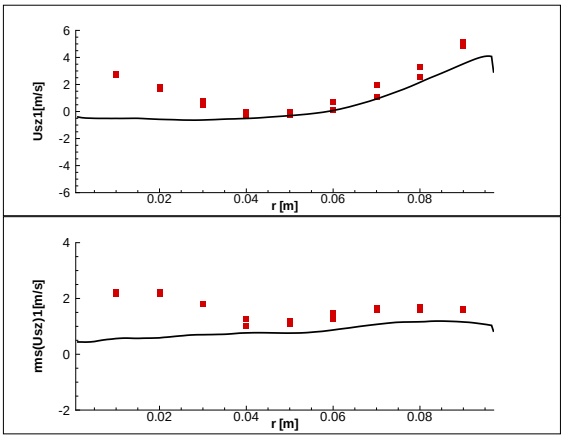

(a)

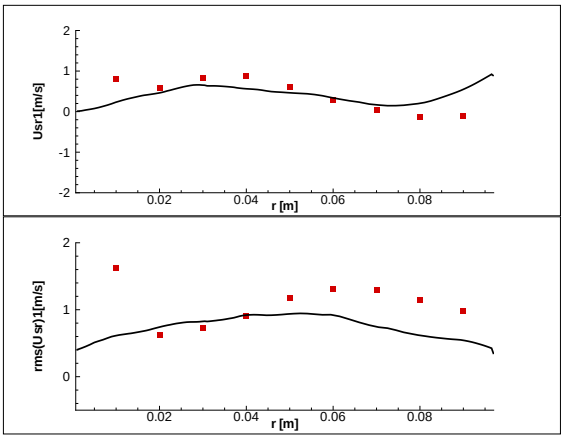

(b)

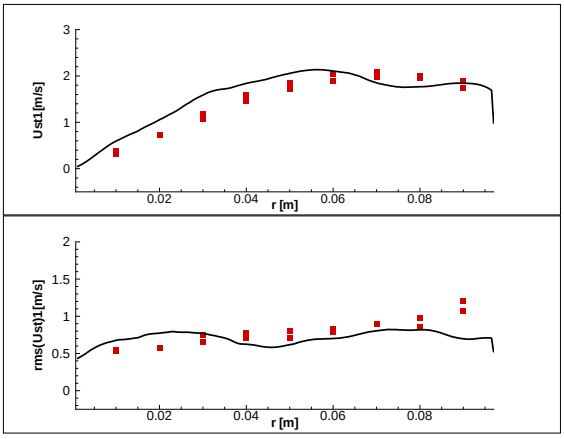

(c)

Figure 3.26: Mean (upper part) and RMS (lower part) axial (a), radial (b) and tangential (c) velocities for $z = 155$ mm. Symbols are taken from experiments. Lines are computed

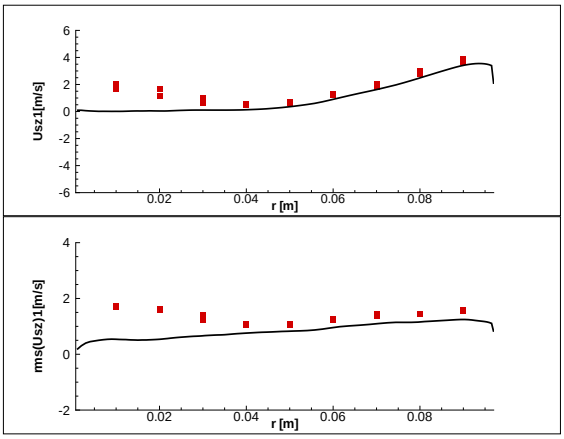

(a)

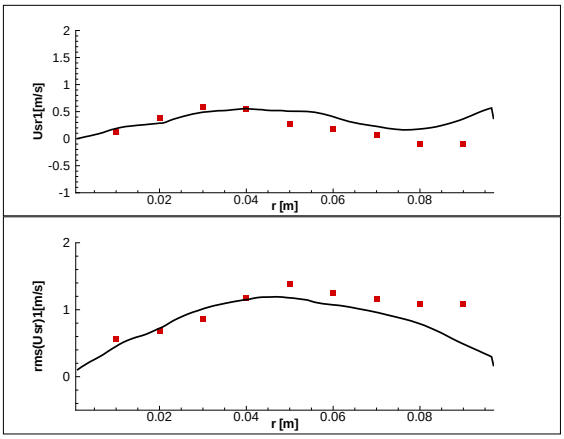

(b)

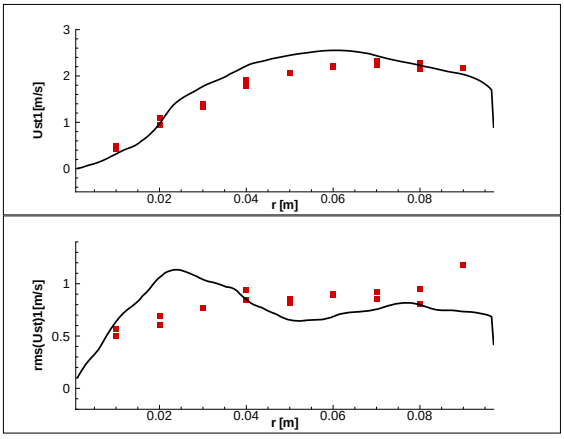

(c)

Figure 3.27: Mean (upper part) and RMS (lower part) axial (a), radial (b) and tangential (c) velocities for $z = 195$ mm. Symbols are taken from experiments. Lines are computed

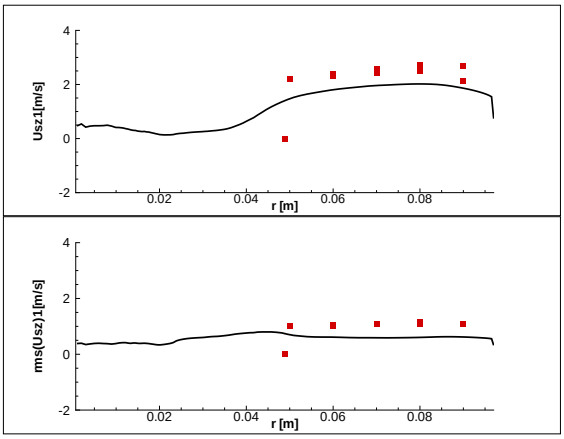

(a)

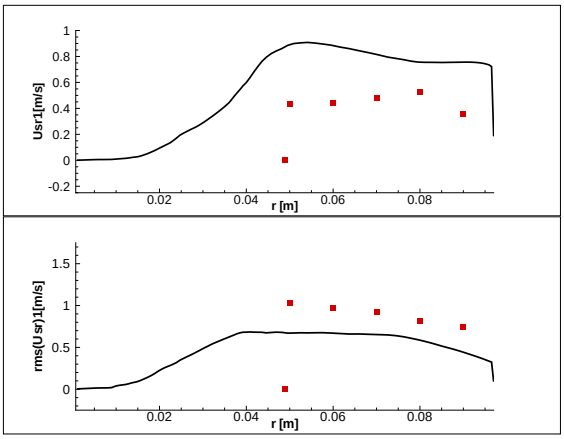

(b)

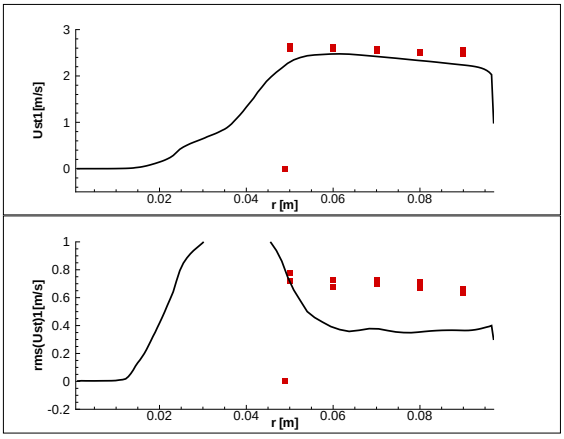

(c)

Figure 3.28: Mean (upper part) and RMS (lower part) axial (a), radial (b) and tangential (c) velocities for $z = 315$ mm. Symbols are taken from experiments. Lines are computed

3.3 Chapter conclusions

In the present chapter the dispersed phase reference model (equations 1.54-1.58) with the adopted numerics has been validated. The simulation results show an overall good agreement with the experimental data for both phases, as far as the mean flow is considered. They also present an under estimation of the velocity fluctuations, especially at increasing distances from the injection plane. Most of the discrepacies of the predicted velocity of the dispersed phase from their experimental values are to be addressed to the errors in the gas phase prediction due to the poor resolution imposed by the structured grid constraint. Nevertheless, in some parts of the domain, the errors in the particle velocity can be indentified as the result of the adopted model limits. The addition of the terms and equations of the model connected to the uncorrelated energy and in particular those proposed in [15], are expected to overcome these problems or, at least, to reduce their effects.

As already said the SGS model also needed to be changed in order to well reproduce the Sommerfeld & Qiu experiment. The final solution was found by adopting the strategies reported in section 1.3.

Conclusion

The numerical simulation of two-phase flows is becoming an important resource for manufacturers when combustion applications are considered. Both aeroengines and industrial burners need the adoption of more and more complex design techniques in order to fulfil the environmental regulation and the necessity of granting higher performance. Among these design assisting tools, LES of multiphase flows is growing in importance in the last years because of its ability in providing a large amount of details, its reliability and relatively easiness to be used when compared to RANS techniques. In the framework of dispersed multiphase flows, LES modeling of the carrier phase is generally used in conjunction with a Lagrangian description of the motion of the inclusions [7]. However, in the last years, researchers also focused on the Eulerian/Eulerian formulation, where both phases are modelled within an Eulerian frame of reference [2, 23, 12, 14, 50]. The reasons for these new attention must be searched in the possibility to use techniques already developed for gaseous flows and in the greater efficiency that can be obtained in the parallelization of the algorithms [9].

The applicability of two-fluid models to combustion applications has been proved [51] in conjunction with the adoption of SGS modelling for the dispersed phase. Nevertheless, these models do not take into account yet the uncorrelated motion of each particle with respect to the particle cloud it belongs to. Although this feature has been studied and models proposed in several publications [2, 23, 12] and its inclusion in the model is considered important to reproduce particle dispersion, its applicability has never been proved. The simulations based on the models developed to resemble this characteristic of the dispersed phase result in the laminarization of the particle flow [13].

Within the presented framework, the objectives of the present work were:

1. to select a model for the simulation of multiphase reacting flows, applicable to coal powder combustion applications under dilute regimes, and test it in conjunction with LES modelling of turbulence in the carrier phase;

2. to propose and validate a robust numerical treatment for the dispersed phase equations;

3. to implement the submodels needed to describe the evolution of coal in the burner.

In order to complete the second point in the above list, the choice was made to use the HeaRT code developed by the *High Performance Computing Group* (HPCG) in ENEA, the Italian National Agency for the New Technologies, Energy and Sustainable Development.

In Chapter 1 a complete model for two-phase dispersed flows is presented. Mass exchange submodels necessary in order to accurately model the evolution of the coal particles have been implemented in the HeaRT code as well.

In Chapter 2 suitable numerics for the two-fluid model adopted in the validation is described. Differently from other numerical implementations of two-fluid models (CERFACS AVBP) [51], no SGS terms are present in the model for the dispersed phase validated in the present work. A II order finite volume upwind scheme with ENO reconstruction has been proposed for the discretization of this part of the overall model. *Ad hoc* Riemann solvers and flux limiters have been developed in order to reproduce the inherent upwind nature of the inertial particle flow in dilute conditions, and the non negativity of some variables like the particle number density n_p and the dispersed phase volumetric fraction α_p.

A particle laden flow experiment [39] from the literature has been selected for the validation, because of the complex flow configuration, that can be also found in industrial burners, and the large amount of available data. The results of this validation are showed in Chapter 3. The numerical solution resembles the main features of both phases and, given the complexity of flow, can be considered acceptable. The predicted level of fluctuations is in overall agreement with the experimental data.

The performed simulations allowed to state that:

1. the chosen numerical treatment for the transport equations is sufficiently robust;

2. the choice not to introduce any SGS model in the dispersed phase equations seems to be confirmed by the agreement of predicted fluctuations compared with the experimental ones, in correspondence to the larger gas phase structures, where the gas phase fluctuation are well predicted;

3. the simulation shows the problems of underprediction of small scale fluctuations in the dispersed phase motion and of the particle front velocity that are considered, in this work, to be due to the impossibility of the implemented model to fully resemble the evolution of inertial particles under dilute condition.

Bibliography

[1] A.N. Kolmogorov. *Dokl. Akad. Nauk*, 30:299, 1941.

[2] A. Kaufmann. Towards eulerian-eulerian large eddy simulation of reactive two-phase flows. Phd thesis, CERFACS Toulouse, 2004.

[3] C.T. Crowe, editor. *Multiphase Flow Handbook*. Taylor and Francis, 2006.

[4] E.Loth. Numerical approaches for motion of dispersed particles, droplets and bubbles. *Progress in Energy and Combustion Science*, 26:161–223, 2000.

[5] W.A.Sirignano. Fluid dynamics and trasport of droplets and sprays. 1999.

[6] C.Pera J. Réveillon, M.Massot. Analysis and modeling of the dispersion of vaporizing polydispersed sprays in turbulent flows. In *Proceedings of the summer program*, Centre for Turbulence Research, 2002.

[7] J.C. Oefelein. Large eddy simulation of turbulent combustion processes in propulsion and power systems. *Prog. Aerosp. Sci.*, 42:2–37, 2006.

[8] F. Ham et al. Unstructured LES of reacting multiphase flows in realistic gas turbine combustors. *Annual Research Briefs, Center for Turbulence Research*, 2003.

[9] M. García E. Riber O. Simonin and T. Poinsot. Comparison between euler/euler and euler/lagrange LES approaches for confined bluff-body gas-solid flow. *International Conference on Multiphase Flow*, 2007.

[10] O.A. Druzhinin and S. Elghobashi. Direct numerical simulations of bubble-laden flows using the two-fluid formulation. *Phys. Fluids*, 10:685–697, 1998.

[11] O. Simonin, P. Février, and J. Laviéville. On the spatial distribution of heavy-particle velocities in turbulent flow: from continuous field to particulate chaos. *Journal of Turbulence*, 3:1–18, 2002.

[12] M. Moreau. *Modélisation numérique direct et des grandes échelles des écoulements turbulents gaz-particules dans le formalisme eulérien mésoscopique*. Phd thesis, Institut National Polytechnique de Toulouse, 2006.

[13] E. Riber. Developpement de la methode de simulation aux grandes echelles pour les ecoulements diphasiques turbulents. Phd thesis, CERFACS Toulouse, 2007.

[14] J.-B. Mossa. *Extension polydisperse pour la description euler-euler des écoulements diphasiques réactifs - TH/CFD/05/74*. PhD thesis, Institut National Polytechnique de Toulouse, 2005.

[15] F. Donato. Numerical modeling of multiphase reacting flows. Phd thesis, "Sapienza" University of Rome, 2010.

[16] T. Poinsot D. Veynante. *Theoretical and Numerical Combustion, 2nd edition*. Edwards, Philadelphia, 2005.

[17] L. Bognetti. Modellistica LES. Internal report, Dipartimento di Meccanica ed Aeronautica, UniversitÃ degli Studi di Roma "La Sapienza", 1998.

[18] K.K. Kuo. *Principles of Combustion*. John Wiley & Sons, New-York, 1986.

[19] Maxwell J.C. *Phil. Mag.*, XIX:19–32, 1960.

[20] Maxwell J.C. *Phil. Mag.*, XX:21–36, 1968.

[21] Stefan J. *Sitzungsber. Kais. Akad. Wiss.*, LXIII(2):63–124, 1971.

[22] Stefan J. *Sitzungsber. Kais. Akad. Wiss.*, LXV(2):323–363, 1972.

[23] P. Février, O. Simonin, and K.D. Squires. Partitioning of particle velocities in gas-solid turbulent flows into a continuous field and a spatially uncorrelated random distribution: theoretical formalism and numerical study. *j. Fluid Mech*, 533:1–46, 2005.

[24] S. Chapman and T.G. Cowling. *The mathematical theory of non-uniform gasses*. Cambridge University Press, Cambridge, 1958.

[25] S. Sommariva T. Maffei G. Migliavacca T. Faravelli E. Ranzi. A predictive multi-step kinetic model of coal devolatilization.

[26] M.L. Hobbs P.T. Radulovic and L.D. Smoot. Modeling fixed bed coal gasifiers. *AIChE Journal*, 38(5):681–702, 1992.

[27] D. Merrick. Mathematical model of thermal decomposition of coal. *Fuel*, 62(4):534–546, 1983.

[28] E. Giacomazzi. Modellistica e simulazione della combustione turbolenta. Tesi di dottorato di ricerca in meccanica teorica e applicata, UniversitÃ "La Sapienza", Dipartimento di Meccanica ed Aeronautica, Roma, 1999.

[29] E. Giacomazzi, C. Bruno, and B. Favini. Fractal modeling of turbulent mixing. *Combustion Theory and Modeling*, 3:637–655, 1999.

[30] E. Giacomazzi, C. Bruno, and B. Favini. Fractal modeling of turbulent combustion. *Combustion Theory and Modeling*, 4:391–412, 2000.

[31] E. Giacomazzi, V. Battaglia, and C. Bruno. The coupling of turbulence and chemistry in a premixed bluff-body flame as studied by LES. *Combustion and Flame*, 138:320–335, 2004.

[32] K.R. Sreenivasan. Fractals and multifractals in fluid turbulence. *Annu.Rev. Fluid Mech.*, 23:539–600, 1991.

[33] U. Frish. *Turbulence, the Legacy of A N Kolmogorov*. Cambridge University Press, Cambridge, 1995.

[34] F.C. Gouldin. An application of fractals to modeling premixed turbulent flames. *Combust. Flame*, 68:249–266, 1987.

[35] M. Murayama and T. Takeno. Fractal-like character of flamelets in turbulent premixed combustion. *22nd Int. Symp. on Combustion*, pages 551–559, 1988.

[36] N. Chakraborty and M. Klein. A priori direct numerical simulation assessment of algebraic flame surface density models for turbulent premixed flames in the context of large eddy simulation. *Physics of fluids*, 20(085108):1–14, 2008.

[37] B.F. Magnussen and B.H. Hjertager. *Proc. Combust. Inst.*, 16, 1976.

[38] B.F. Magnussen. Report n-7034, Division of Thermodynamics, Trondheim, Norwegian Institute of Technology, 1989.

[39] M. Sommerfeld and H.H. Qiu. Detailed measurements in a swirling particulate twophase flow by a phase-doppler anemometer. *Int Journal Heat and Fluid Flow*, 12:20–28, 1991.

[40] M. Germano, U. Piomelli, P. Moin, and W. H. Cabot. A dynamic subgrid-scale eddy viscosity model. *Phys. Fluids A*, 3:1760–1765, 1991.

[41] L. Cervone. Modelli di simulazione di flussi bifase per motori a propellente solido. Master's thesis, La Sapienza University, Rome, 2001-2002. *In italian*.

[42] C. Shu and S. Osher. Efficient implementation of eno shock-capturing schemes. *J. Comp. Phys.*, 77:439–471, 1988.

[43] S. Nagarajan, S.K. Lele, and J.H. Ferziger. A robust high-order compact method for large eddy simulation. *J. Comp. Phys.*, 191:392–419, 2003.

[44] H.D. Thompson, B.W. Webb, and J.D. Hoffman. The cell reynolds number myth. *Int. J. Num. Meth. Fluids*, 5(4):305–310, 2005.

[45] M. Sommerfeld and H.H. Qiu. Characterization of particle-laden, confined swirling flows by phase-doppler anemometry and numerical calculation. *Int. J. Multiphase Flow*, 19(6):1093–1127, 1993.

[46] M. Klein, A. Sadiki, and J. Janicka. A digital filter based generation of inflow data for spatially developing direct numerical simulation or large eddy simulation. *J. Comp. Phys.*, 186:652–665, 2003.

[47] T.J. Poinsot and S.K. Lele. Boundary conditions for direct simulations of compressible viscous flows. *J. Comp. Phys.*, 101:104–129, 1992.

[48] J.C. Sutherland and C.A. Kennedy. Improved boundary conditions for viscous reacting compressible flows. *J. Comp. Phys.*, 101:502–524, 2003.

[49] M. Boileau, S. Pascaud, E. Riber, B. Cuenot, L.Y.M. Gicquel, and T. Poinsot. Investigation of two-fluid methods for Large Eddy Simulation of spray combustion in gas turbines. Technical report, 2007.

[50] S. de Chaisemartin, F. Laurent, M. Massot, and J. Reveillon. Evaluation of eulerian multi-fluid versus lagrangian methods for ejection of polydispersed evaporating sprays by vortices. *Preprint to be submitted to J. of Comp. Phys.*, 2007.

[51] M. Boileau, G. Staffelbach, B. Cuenot, T. Poinsot, and C. Bérat. LES of an ignition sequence in a gas turbine engine. *Combustion and Flame*, 154(1-2):2–22, 2008.